

# Robust Nucleus/Cell Detection and Segmentation in Digital Pathology and Microscopy Images: A Comprehensive Review

Fuyong Xing, *Student Member, IEEE*, and Lin Yang, *Member, IEEE*

(*Clinical Application Review*)

**Abstract**—Digital pathology and microscopy image analysis is widely used for comprehensive studies of cell morphology or tissue structure. Manual assessment is labor intensive and prone to interobserver variations. Computer-aided methods, which can significantly improve the objectivity and reproducibility, have attracted a great deal of interest in recent literature. Among the pipeline of building a computer-aided diagnosis system, nucleus or cell detection and segmentation play a very important role to describe the molecular morphological information. In the past few decades, many efforts have been devoted to automated nucleus/cell detection and segmentation. In this review, we provide a comprehensive summary of the recent state-of-the-art nucleus/cell segmentation approaches on different types of microscopy images including bright-field, phase-contrast, differential interference contrast, fluorescence, and electron microscopies. In addition, we discuss the challenges for the current methods and the potential future work of nucleus/cell detection and segmentation.

**Index Terms**—Cell, detection, digital pathology, histopathology, microscopy images, nucleus, segmentation.

## I. INTRODUCTION

DIGITAL pathology and microscopy images play a significant role in decision making for disease diagnosis, since they can provide extensive information for CAD, which enables quantitative analysis of digital images with a high throughput processing rate. Nowadays, automatic digital pathology including image analysis, which can greatly benefit pathologists and patients, has attracted much attention in both research and clinical practice [1], [2]. In comparison with manual assessment that is labor intensive and time consuming, computerized approaches [3]–[6] provide faster and reproducible image analysis such that the basic science researchers and clinician scientists can be released from boring and repeated routine efforts. More importantly, the complex nature of pathology and microscopy

images presents significant challenges for manual image analysis, which might lead to large interobserver variations [7]; on the other hand, the CAD can greatly reduce the bias and provide accurate characterization of diseases [8]. In addition, it allows personalized treatments that can significantly benefit the patients. In order to handle large-scale image datasets, grid computing [9]–[11] and computationally scalable algorithms [12]–[14] are reported for high-throughput pathology image analysis. Another advantage of automated methods is that they can easily provide reproducible and rigorous measurements of important image features, which will be used with clinical followup, and thus, allows comparative study and potential prognosis and personalized medicine.

A critical prerequisite in CAD is nucleus/cell detection and segmentation, which is usually considered as the basis of automated image analysis. It provides supports for various quantitative analyses including calculating cellular morphology, such as size, shape, texture, and other imagenomics. However, it is difficult to achieve robust and accurate nucleus/cell segmentation. First, pathology, especially histopathology, and microscopy images often exhibit background clutter with many noises, artifacts (e.g., blurred regions) introduced during image acquisition, and potential poor contrast between the foreground and the background. Second, there exist significant variations on nucleus/cell size, shape, and intracellular intensity heterogeneity. Finally, nuclei/cells are often clustered into clumps so that they might partially overlap with one another. Many efforts have been made to achieve automated nucleus/cell detection and segmentation, aiming to tackle some or all of these challenges.

Currently, there are several reviews on automated pathology image analysis. The review in [15] summarizes the CAD system technologies for histopathology image analysis, which covers preprocessing (color and illumination normalization), nucleus and gland segmentation, feature extraction, and classification. Some other CAD systems on histopathological images can be found in [16] and [17]. A specific review on breast cancer histopathology image analysis is presented in [18], which additionally covers mitosis detection and proliferation assessment. Fuchs and Buhmann [19] have provided a broader overview of a workflow in computational pathology, which consists of three components: image data acquisition and ground-truth generation; image analysis including object detection, segmentation, and recognition; and medical statistics in terms of survival analysis. Kothari *et al.* [20] have presented a review on

Manuscript received August 13, 2015; revised November 21, 2015; accepted December 7, 2015. Date of publication January 6, 2016; date of current version September 16, 2016. This work was supported in part by NIH 1R01AR06547901A1 and in part by the startup grant from The University of Florida.

The authors are with the Department of Electrical and Computer Engineering and the J. Crayton Pruitt Family Department of Biomedical Engineering, University of Florida, Gainesville, FL 32611 USA (e-mail: f.xing@ufl.edu; lin.yang@bme.ufl.edu).

Digital Object Identifier 10.1109/RBME.2016.2515127

TABLE I  
NOMENCLATURE (ABBR. = ABBREVIATION)

Abbr.	Description	Abbr.	Description	Abbr.	Description
CAD	Computer-aided diagnosis	SIFT	Scale-invariant feature transform	MAP	Maximum a posteriori
WSI	Whole-slide imaging	DIC	Differential interference contrast	BRF	Balanced random forest
H&E	Hematoxylin and eosin	LoG	Laplacian of Gaussian	GMM	Gaussian mixture model
IHC	Immunohistochemistry	MESR	Maximally stable extremal region	SVM	Support vector machine
DT	Distance transform	HT	Hough transform	NET	Neuroendocrine tumor
EDT	Euclidean DT	PCA	Principle component analysis	TMA	Tissue microscopy array
MO	Morphology operation	ILP	Integer linear programming	FNA	Fine needle aspirates
UE	Ultimate erosion	FRST	Fast radial symmetry transform	GVF	Gradient vector flow
HIT	H-minima transform	OWT	Oriented watershed transform	FCM	Fuzzy c-means
HAT	H-maxima transform	RBSM	Repulsive balloon snake model	EM	Expectation-maximization
LDA	Linear discriminant analysis	CNN	Convolutional neural network	GBM	glioblastoma multiform
CRF	Conditional random field	FISH	Fluorescence <i>in situ</i> hybridization	MDC	Most discriminant color
LFT	Local Fourier transform	PSD	Percentage of symmetry difference	ADT	Alternating decision tree
DET	Detection	SEG	Segmentation	RNAi	RNA interference
UDR	Underdetection rate	ODR	Overdetection rate	CDR	Correct detection rate
USR	Undersegmentation rate	OSR	Oversegmentation rate	CSR	Correct segmentation rate
$A_{sg}$	Area of segmented objects	$A_{gt}$	Area of ground-truth objects	ONL	Outer nuclear layer
INL	Inner nuclear layer	NSD	Normalized sum of distance	SNR	Signal-to-noise ratio
HD	Hausdorff distance	MAD	Mean absolute distance	PPV	Positive predictive value
TPR	True positive rate	FPR	False positive rate	FNR	False negative rate

histopathological WSI informatics methods, which includes image quality control, feature extraction, predictive modeling, and visualization. All of these publications are not specifically summarized for nucleus/cell detection and segmentation, and thus, many recent state-of-the-art detection and segmentation algorithms are not discussed. Recently, Irshad *et al.* [21] have reported a survey on the methods for nucleus detection, segmentation, feature extraction, and classification on H&E and IHC-stained histopathology images, but many recent nucleus/cell detection segmentation algorithms on other types of staining images are still missed.

In this review, we extensively and specifically look at the recent state of the arts on automated nucleus/cell detection and segmentation approaches on digital pathology and microscopy (bright-field, phase-contrast, DIC, fluorescence, and electron microscopies) images. We will introduce the major categories of detection and segmentation approaches and explain the mathematical models for basic methods, with discussing their advantages and limitations. The preprocessing techniques including color normalization and image denoising, which are presented in [15], [21], and [22], and extraction of regions of interest, which are introduced in [23]–[25], prior to the detection or segmentation will not be reviewed in this paper. Meanwhile, although immunohistochemical staining is also used to facilitate manual assessment of image analysis [26], [27], it is beyond the scope of this review. We mainly highlight the work after 2000 but some basic methods before that will also be introduced. In addition, we will discuss the problems that many current cell detection and segmentation algorithms might not completely resolve, and provide the future potentials as well. For notation convenience, the nomenclature used in this review is listed in Table I.

## II. NUCLEUS AND CELL DETECTION METHODS

In this review, nucleus/cell detection is viewed as obtaining the object location without accurately delineating the

boundaries, and it is usually referred to as marker or seed seeking near the object centroids, one per nucleus/cell. The marker can be a single point or a small region inside the object. Clearly, marker detection can provide support for nucleus/cell counting, tracking, and segmentation. Although different types of microscopy images or staining images exhibit significant variations on image characteristics such that each might require a specific algorithm for nucleus/cell detection, the major methods presented in recent literature can be broadly classified into several groups based on their underlying algorithms: DT, morphology operation, HIT/HAT, LoG filtering, MSER detection, HT, radial symmetry-based voting, and supervised learning. For each group, we will first introduce the underlying algorithms, and then, the variants and applications on specific types of images. Note that the whole procedure of a marker detection method might combine several basic algorithms as well as other methods for specific object detection. For better comparison and illustration, we summarize those journal publications containing nucleus/cell detection in Tables II–IV. In the columns of *DET results* and *SEG results* of these tables, we report the detection and segmentation accuracy, respectively, if there exist specific quantification reported in the publications; otherwise we provide only the metrics. Note that the goals of many works are to segment or classify nuclei/cells based on the detection results so that they might not provide specific quantitative analysis of the detection but only quantify the segmentation or the classification.

### A. DT

A simple approach to detect markers is DT, which assigns each pixel/voxel with the distance to the nearest feature point [49]. In nucleus/cell detection, the feature points are usually selected as the edge pixels/voxels in a binary image and Euclidean distance is chosen as the metric. Therefore, ideally the local maxima in the generated distance map correspond to the centroids of nuclei or cells. EDT is often paired with watershed segmentation, since the inverse distance map eliminates

TABLE II  
SUMMARY OF JOURNAL PUBLICATIONS BASED ON THE UNDERLYING ALGORITHMS OF DETECTION AND SEGMENTATION METHODS

	Data	DET	DET Results	SEG	SEG Results
[28]	100 breast cancer nuclei	EDT	-	region growing	PSD: $\leq 7\%$
[29]	20 sets of Drosophila RNAi fluorescence cell images	EDT	-	level set	$F_1: > 84\%$
[30]	100 nucleus images, over 100 macrophases (cells)	EDT	CDR: $> 98\%$ (nucleus)	region growing	PSD: 85% (cell)
[31]	240 HeLa H2B-GFP cell images	EDT	-	watershed	CSR/USR/OSR: 99%/0.82%/0.19%
[32]	2 HeLa H2B-GFP cell sequences	EDT	-	watershed	CSR/USR/OSR: 99.5%/0.3%/0.2%
[33]	5 image stacks of rat brain tissues	EDT	-	watershed	CSR: 97%
[34]	12 electron micrograph images	MO	-	EM	direct count
[35]	5 HeLa cell fluorescence images	MO	-	watershed	CSR/USR/OSR: 98.8%/0.7%/0.5%
[36]	PC12 and NRK cell images	MO	-	watershed, level set	similarity measure†
[37]	38 Pap smear images	MO	CDR: 99.25%	FCM, SVM	sensitivity/specificity: 90.57%/75.28% (FCM), 69.86%/92.02% (SVM)
[38]	35 breast cancer mitotic cell images	MO, SVM	sensitivity/precision/ F-measure: 81.5%/33.9%/47.9%	thresholding	sensitivity/precision/ MAD: 89.3%/87.5%/1.74
[39]	50 blood smear images	MO, fuzzy cellular neural network	CDR: 98%	-	-
[40]	152 Pap smear images	HIT	-	active physical model	HD: $19.91 \pm 8.38$ , Euclidean distance: $8.71 \pm 3.45$ $\frac{A_{sg} \cap A_{gt}}{A_{sg} \cup A_{gt}}$
[41]	1439 nuclei in breast tissue FISH images	HAT	-	watershed	-
[42]	3 MadinDarby canine kidney (MDCK) epithelial cell and 4 human umbilical vein endothelial cell (HUVEC) image sequences	HAT	accuracy: 90.12%	-	-
[43]	6 2-D prostate carcinoma (P) and 1 3-D cervical carcinoma (C) images	HAT	-	watershed	CSR: 91% (P), 91% (C)
[44]	53 mouse neuronal and 4 Drosophila Kc167 cell images	HAT	-	watershed	CSR/USR/OSR: 97.39%/0.78%/1.83% (mouse) 96.30%/0.46%/3.24% (Drosophila)
[45]	5762 nuclei of cervical cells and mammary invasive ductal carcinomas	HIT	-	watershed	CSR/USR/OSR: 96.74%/0.65%/2.61%
[46]	20 endometrial images	HAT	precision/recall/ $F_1$ : 86%/83%/84% (stromal), 89%/91%/90% (uNK)	-	-
[47]	700 frames from 3 murine embryonic cell and 1 HeLa cell sequences	HAT	precision/recall: 94.37%/96.75%	-	-
[48]	3 mouse embryonic cell and 1 HeLa cell sequences	HAT	precision/recall/ $F_1$ : 94.8%/92.4%/93.6%	watershed, Adaboost	area overlap accuracy, Kappa Index

†See Table III in [36].

many unnecessary local minima that will lead to serious over-segmentation, and the remaining minima serve as the seeds for watershed transform flooding.

Adiga *et al.* [28] have exploited a DT to detect nucleus centers in breast cancer histopathological images, Yan *et al.* [29] have used EDT to locate nucleus centers as seeds for subsequent watershed segmentation in RNAi fluorescence images, and some other similar EDT-based nucleus centroid detection methods for fluorescence microscopy images are reported in [30] and [50]. However, EDT is only effective on regular shapes in a binary image, and small variations on the edge pixels will result in false local maxima. Therefore, it might fail to detect overlapping

nuclei or cells. In [31] and [32], the original intensity is first added to the distance map, then a Gaussian filter is applied to the combined image for noise suppression, and finally, the local maxima are detected by tracing simulated particles in the GVF of the combined image. Since nonlocal maxima have very few accumulated pixels, a simple threshold is applied to the number of accumulated pixels to detect local maxima, which correspond to the centers of HeLa cell nuclei in fluorescence images. In [33], Lin *et al.* have proposed a gradient weighted-DT method to locate nucleus centroids in 3-D fluorescence images, which applies a multiplication to the distance map and the normalized gradient magnitude image. Although image intensity or gradient

TABLE III  
SUMMARY OF JOURNAL PUBLICATIONS BASED ON THE UNDERLYING ALGORITHMS OF DETECTION AND SEGMENTATION METHODS

	Data	DET	DET Results	SEG	SEG Results
[67]	41 retinal images	LoG	counting error: 3.67% in ONL, 8.55% in INL	-	-
[68]	15 K1735 tumor cell and 10 breast histopathology images	LoG	-	graph cut	CSR: 86.3%
[69]	20 GBM images	LoG	-	graph cut	precision/recall/F <sub>1</sub> : 75%/85%/79.7%
[70]	15 pathology and 7 fluorescent images	generalized LoG	detection rate, FPR	-	-
[71]	15 pathological images (P) and 200 fluorescent images (F)	Hessian-based LoG	precision/recall/F <sub>1</sub> : 92.4%/92.5%/92.4% (P)	-	-
[72]	600 human forearm skin images	Hessian analysis	-	convergence index filter	nuclear-to-cytoplasmic ratio: 0.328 ± 0.023
[73]	16 images <i>Drosophila melanogaster</i> Kc167 images	sliding band filter	precision/recall/F <sub>1</sub> : 95%/69%/80%(nuclei), 82%/90%/89%(cytop.)	-	-
[74]	16 cervical extended depth of field (EDF) images	MSER	precision: 73%, recall: 85%	level set	precision/recall/Dice: 96%/90%/92%
[75]	198 molecular (M), 22 HeLa cell (H), 22 blastocyst (B), 20 Lymphocyte (L), and 20 fluorescent nuclei (F) images	MSER, structured SVM	F <sub>1</sub> -score: 77.43%±1.98%(M), 97.1%±0.27%(H), 85.9%±0.94%(B), 87.4%±1.66%(L), 89.05%±0.29%(F)	-	-
[76]	20 zebrafish (Z), 20 bovine aortic endothelial (B), and 20 human central nervous system stem (H) cell images	Thresholding, SVM	F <sub>1</sub> -score: 95.4%(Z), 92%(B), 90.5%(H)	-	-
[77]	207 cervical images	HT	PPV/TPR/F-measure: 96.69%/95.63%/96.15%	level set	mean difference: 0.205
[78]	737 breast cancer images	HT, SVM	effectiveness: 98.51%	-	-
[79]	100 follicular lymphoma images	FRST, EM	accuracy: 80.7%	-	-
[80]	234 breast TMA images	single-pass voting	pixel-wise error: 6.63	level set	precision: 90%, recall: 78%
[81]	10 lung cancer images	single-pass voting	precision/recall/F <sub>1</sub> : 99.7%/84%/90%	snake	precision/recall: 87%/95%
[82]	129 NET images	single-pass voting	precision/recall/F <sub>1</sub> : 89%/91%/90%	-	-
[83]	114 cutaneous histopathological images [skin epidermis (E) and dermis (D)]	single-pass voting	precision/sensitivity: 85.99%/94.4%(E), 92.2%/93.7%(D)	watershed	CSR/USR/OSR: 92.18%/5.39%/2.43% (E), 93.15%/6.06%/0.79% (D)

TABLE IV  
SUMMARY OF JOURNAL PUBLICATIONS BASED ON THE UNDERLYING ALGORITHMS OF DETECTION AND SEGMENTATION METHODS

	Data	DET	DET Results	SEG	SEG Results
[122]	over 500 multifocus z-stack muscle images	SVM, mean shift	precision/recall/F <sub>1</sub> : 93%/96% /94%	-	-
[123]	10 bladder inverted papilloma images	SVM	USR: 0.2%, OSR: 0.4%	watershed	MAD: 0.85
[124]	6 CHO, 5 L929, and 5 Sf21 cell line images	random forest, hierarchical clustering	precision: 77.7%±8%(CHO), 82.8%±4.4% (L929), 97.3%±0.9% (Sf21), recall: 92.9%±3%(CHO), 92.6%±2.9% (L929), 96.4%±3.2% (Sf21)	-	-
[125]	30 brain tumor (BT), 51 pancreatic neuroendocrine tumor (NET), and 35 breast cancer (BC) images	CNN	precision/recall/F <sub>1</sub> : 72%±20%/88%±15%/77%±16% (BT), 84%±8%/93%±5%/88%±4% (NET), 71%±14%/88%±9%/78%±8% (BC)	active contour	Dice/HD/MAD: 85%±11%/5.06±5.26/3.26±2.89 (BT), 92%±9%/2.41±2.99/1.58±1.75 (NET), 80%±15%/8.6±6.77/6.24±4.90 (BC)
[126]	21 cervical images	multiscale CNN, graph cut	-	watershed	Dice: 95%±18% (cytoplasm), F <sub>1</sub> : 99%±1% (nuclei)
[127]	48 U2OS and 49 NIH3T3 cell images	PCA, template matching	-	nonrigid registration	Rand index: 95% (U2OS), 91% (NIH3T3), Jaccard index: 2.5 (U2OS), 2.72 (NIH3T3)
[128]	30 rolling leukocyte images	Bayesian classifier	detection rate/ false alarm rate: 78.6%/13.1%	-	-
[129]	50 breast histology images	sparse representation classification	precision/recall/F <sub>1</sub> : 84.98%/87.18%/86.07%	-	-



information is used to improve the distance maps, it is often not sufficient to handle appearance variations of the complex histopathological images so that it might lead to over-detection.

### B. Morphology Operation

Based on the mathematical morphology theory, binary morphological filtering is a technique processing the images with a certain structure element, such as circular disk, square, cross, etc. [51]. It performs image filtering by examining the geometrical and topological structures of objects with a predefined shape. There exist four basic shift-invariant operators: erosion, dilation, opening, and closing, which can be used to generate other basic morphological operations such as boundary extraction, hole filling, skeletonizing, etc. The binary mathematical morphology can be extended to gray-scale morphology and directly applied to gray-scale images [52], [53]. Some widely used operators, such as top-hat and bottom-hat transforms, are derived from those basic gray-level operators and can be used for image enhancement, which facilitates further image analysis such as extracting small objects.

UE is a popular mathematical morphology operation for marker detection. It repeatedly applies a series of erosion operator to each connected component until one more erosion will completely remove the component [54]. In this way, touching or overlapping objects can be separated. However, UE might produce more than one marker per object in noisy images. In order to address this issue, Park *et al.* [34] have proposed an improved UE operation that exploits a noise-robust measurement of convexity as the stopping criterion for erosion. Specifically, starting with a binary image, for each non-convex connected component it iteratively performs an erosion with a one-pixel-radius disk structure element until the component is convex. The convexity (or concavity) is measured based on the sensitivity to the coarseness of digital grids [55]. This method is validated for nucleus-like nanoparticle detection in electron microscopy images, and generally can provide an earlier stopping for erosion than the traditional UE. Nevertheless, it is designed for binary images, and perfect binarization is not easy on H&E-stained histopathology images.

Instead of relying on UE, Yang *et al.* [35] have presented a conditional erosion method to detect nucleus markers in fluorescence microscopy images. Considering the elliptical shapes of nuclei, it defines four  $7 \times 7$  mask structures for coarse erosion and two  $3 \times 3$  mask structures for fine erosion. The former can preserve object shapes, and the latter is used to avoid undersegmentation. Given two threshold  $T_1$  and  $T_2$ , it applies a coarse-to-fine strategy to marker detection with three steps: 1) erode iteratively with coarse structures until the component size is smaller than  $T_1$ , 2) repeat the erosion with fine structures until the component size is smaller than  $T_2$ , and 3) collect the components from previous two steps as markers. Similar to UE, this conditional erosion is defined on binary images, and meanwhile it requires two extra predefined thresholds for termination, which need to be carefully selected for different pathology and microscopy images. Hodneland *et al.* [36] have proposed a morphology operation-based cell detection approach on 3-D fluorescence images. It first applies adaptive threshold [56] to ridge

extraction, and then, performs iterative close operation with an increasing-radius circular structure element to link the gaps in the binary edges. The holes in the closed objects are detected as candidate markers, which are further refined by removing

---

#### Algorithm 1: Gray-scale morphological reconstruction-based nucleus detection in [37]

---

1. Obtain initial candidate nucleus centroids based on gray-scale morphological reconstruction [58]
  2. Refine the nucleus centroids by searching nucleus boundaries from the centroids in the morphological gradient image
  3. Remove redundant centroids based on a distance-dependent rule
  4. Recognize true nucleus centroids from others using FCM [59] or SVM [60]
- 

those area smaller than a userdefined threshold. This method is suitable for those images in which nucleus/cell boundaries are easy to extract.

Without converting into binary images, gray-scale morphology operation has also been applied to nucleus/cell detection. Plissiti *et al.* [37] have presented a gray-scale morphological reconstruction-based nucleus detection on Pap smear images, which can be summarized as the four steps in Algorithm 1. Another similar strategy [38] in the manner of “first candidate generation, and then, classification” is reported for mitotic cell detection on H&E-stained multispectral microscopy images. It first creates candidate regions based on opening-by-reconstruction and closing-by-reconstruction, then segments out the intact regions with local thresholding, and finally, applies an SVM to mitotic cell classification. Gray-scale morphology-based marker detection can also be found in [57], which identifies nuclei in RNAi fluorescence images. In [39], a white blood cell detection algorithm applies morphological gray reconstruction based on a fuzzy cellular neural network to complete contour extraction of white blood cells.

### C. HIT/HAT

HIT is based on the morphology operation, and it is widely used in local minima detection. Given an initial image  $A$  (e.g., an inverse distance map) and a depth value  $h$ , HIT [51] is represented by

$$H(A, h) = R^{\varepsilon}(A + h) \quad (1)$$

where  $R^{\varepsilon}$  denotes the operator of morphological reconstruction by erosion. In the resulting image, all the regional minima whose depth is not larger than  $h$  are suppressed and the initially connected components can be split in terms of the detected minima. The parameter  $h$  plays a significant role in the marker extraction: a larger value might lead to undersegmentation and conversely a smaller value can result in oversegmentation. Compared with DT using all minima as markers, HIT can remove spurious local minima caused by uneven object shapes or noises and generates correct markers. On the contrary, HAT suppresses the regional maxima whose height is not larger than  $h$ . In order to improve

the robustness, it is often necessary to perform image enhancement before HIT/HAT. Like DT in pathology and microscopy image analysis, HIT/HAT is usually used to generate markers for watershed transform-based nucleus or cell segmentation.

---

**Algorithm 2:** HAT-based nucleus detection in [41]
 

---

1. Normalize intensity by its maximum value in the blue channel
  2. Perform top-hat filtering to reduce the effects of color diffusion
  3. Segment out the foreground by Otsu's method [63]
  4. Identify and fill the holes in a single nucleus
  5. Apply HAT to marker detection
- 

HIT/HAT is very popular in locating nuclei/cells in biomedical images. Plissiti and Nikou [40] have applied HIT to overlapping nuclei detection in Pap smear images, which are smoothed in advance by a Gaussian filter, and then, enhanced by histogram equalization. Raimondo *et al.* [41] have proposed an HAT-based nucleus detection approach on FISH images, and the details are listed in Algorithm 2. Similar procedures for nucleus detection are applied to IHC-stained breast cancer images [61] and phase contrast microscopy images [42]. In [43] and [62], HAT is applied to nucleus marker detection in original intensity images, which will guide the subsequent watershed segmentation in fluorescence microscopy images. These methods require a properly predefined  $h$  value, which is not easy to achieve in real applications.

An adaptive HIT algorithm is presented in [44], which iteratively increases the  $h$  value until a region merging occurs. In this scenario, it can select an optimal  $h$  value such that resulting markers preserve the shapes of nuclei. However, it ignores the nucleus size such that the number of the nuclei might not be adaptively determined [45]. In [46], an adaptive HAT method is applied to automatic detection of uterine natural killer (uNK) cell nuclei in endometrial histopathology images. Specifically, it clusters the image intensity histograms into multiple ranges with K-means, and then, selects the  $h$  value based on the upper bound of the range corresponding to the uNK nuclei. In addition, it detects the stromal cell nuclei using a local isotropic phase symmetry measure and a boundary searching strategy for redundant detection elimination. Jung and Kim [45] have proposed an HIT-based nucleus marker extraction method on cervical and breast cell images. Starting from the (initial) number  $m$  of regional minima, it iteratively decreases  $m$  by increasing the depth until  $m$  reaches zero. Within each iteration, it performs marker-controlled watershed segmentation and evaluates the segmentation distortion  $S(w_h)$ , which is defined using an ellipse fitting model [64]

$$S(w_h) = \frac{1}{m} \sum_{i=1}^m \text{AFR}(w_{h,i}) \quad (2)$$

$$\text{AFR}(w_{h,i}) = \frac{1}{n_{h,i}} \sum_{j=1}^{n_{h,i}} r(\mathbf{b}_{h,i,j}, F_{h,i}) \quad (3)$$

where  $w_h$  and  $w_{h,i}$  represent the segmentation result using  $h$  value and the  $i$ th nucleus of  $w_h$ , respectively.  $\text{AFR}(\cdot)$  denotes the average of the fitting residuals.  $n_{h,i}$  and  $\mathbf{b}_{h,i,j}$  are the number of boundary points and the  $j$ th boundary point on  $w_{h,i}$ , respectively, and  $r(\mathbf{b}_{h,i,j}, F_{h,i})$  is the distance from  $\mathbf{b}_{h,i,j}$  to the closet point on  $F_{h,i}$ , which is a fitting contour. Finally, the optimal  $h$  value is determined by minimizing the segmentation distortion. A similar algorithm with weighted average fitting residuals is reported in [65] to locate nuclei in fluorescence microscopy images. Another HIT algorithm with automatic selection of the  $h$  value for cell detection is presented in [66], which exploits the variance in the cell areas to evaluate the segmentation quality and the optimal  $h$  corresponds to the case with a minimum area variance. The  $h$  value in HAT can also be determined in terms of the intensity contrast between the nuclei and the background in phase contrast microscopy images [47], [48].

### D. LoG Filtering

In medical image analysis, the LoG filter is one of most popular methods to identify small blob objects, which usually correspond to the central regions of nuclei or cells in microscopy images. Given an image  $I(x, y)$ , the convolution of  $I(x, y)$  with the LoG filter is represented as [84]

$$\nabla^2 L(x, y; \sigma) = I(x, y) * \nabla^2 G(x, y; \sigma) \quad (4)$$

where  $\nabla^2$  and  $G(x, y; \sigma)$  represent the Laplacian operator and the Gaussian kernel with scale parameter  $\sigma$ , respectively. In order to handle object scale variations, Lindeberg [85] has presented a multiscale LoG blob detector by introducing a normalizing factor  $\gamma$  into (4)

$$\nabla^2 L(x, y; \sigma) = I(x, y) * \sigma^\gamma \nabla^2 G(x, y; \sigma). \quad (5)$$

By using the  $\gamma$ , this normalized LoG filter can obtain scale invariance such that the object size can be determined at the scale corresponding to the maximal LoG response.

Byun *et al.* [67] have successfully applied an LoG filter with a specified scale to nucleus locating on retinal images, but this method assumes that the object size is known *a priori*. Later, the scale-normalized LoG filter [85] is used to detect cells on phase-contrast microscopy images [86], [87]; nevertheless, it might fail in touching or overlapping objects which exhibit weak boundaries. To tackle this issue, Al-Kofahi *et al.* [68] have introduced a multiscale LoG filter constrained by a Euclidean distance map to detect nuclei in histopathology images. It is mainly composed of four steps: 1) calculate the filter response using (5) with  $\gamma = 2$  and a set of  $\sigma \in [\sigma_{\min}, \sigma_{\max}]$ ; 2) exploit the distance map to constrain the maximal scale and obtain  $R(x, y) = \arg \max_{\sigma \in [\sigma_{\min}, \sigma_{\max}]} \nabla^2 L(x, y; \sigma)$ , where  $\sigma_{\max} = \max\{\sigma_{\min}, \min\{\sigma_{\max}, 2 \times D(x, y)\}\}$  and  $D(x, y)$  represents the distance map; 3) seek local maxima of  $R(x, y)$  as seeds; and 4) use a local-maximum clustering algorithm [88] to remove false seeds caused by minor peaks in the distance map. Instead of using local-maxima clustering, Chang *et al.* [69] have exploited the response strength and the blue ratio intensity to constrain the LoG-based nucleus marker selection on H&E-stained histopathology images.

In order to detect rotationally asymmetric blobs, Kong *et al.* [70] have proposed a generalized LoG filter to identify elliptical blob structures and successfully applied it to nucleus detection in digitized pathological specimens and cell counting in fluorescence microscopy images. Different from the conventional LoG detector, it defines the Gaussian kernel as

$$G(x, y) = Z \cdot e^{-(ax^2 + 2bxy + cy^2)} \quad (6)$$

where  $Z$  is a normalization constant. The parameters  $a$ ,  $b$ , and  $c$  control the shape and the orientation of  $G(x, y)$ .

Another improvement of the LoG filter is presented in [71], which applies Hessian analysis to the LoG-based detection. Specifically, it first smooths the input image with a multiscale LoG filter, then segments the candidate blobs by identifying the optimal scale based on Hessian analysis, and finally, refines the blobs using an unsupervised GMM. This detector is computationally efficient and has been applied to nucleus detection in both pathology images and fluorescence microscopy images. Similarly, Lee *et al.* [72] have used the determinant of the Hessian matrix to detect nucleus markers in third-harmonic-generation microscopy images. Blob detection using other filters can be found in [73] and [89]. Due to the approximately convex shapes of *Drosophila* Kc167 nuclei in fluorescence microscopy images, a sliding band filter [73] is applied to nucleus detection, which is robust to image noise. In [89], a bilateral filter is applied to the intensity images and the local maxima are detected based on a  $3 \times 3$  window, and thereafter pairwise grouping is used to detect final cell markers.

### E. MSER Detection

The MSER detector [90] is also used to locate blob objects. Similar to the procedure that applying an increasing intensity threshold to a gray-level image, it generates a set of nested extremal regions based on the level sets in the intensity landscape and considers one region to be stable using a local intensity minimum-based criterion. In microscopy image analysis, the MSER-based blob object detection algorithm usually consists of two major steps: 1) generate a sufficient number of extremal regions, and 2) recognize those regions corresponding to real nuclei or cells.

Lu *et al.* [91] have applied this strategy to nucleus detection in Pap smear microscopy images, and simply used the eccentricity to evaluate the MSER detected blobs and filter out those least circular ones that do not correspond to real nuclei. The same algorithm is also presented in [74], which combines the blob appearance information and the shape properties as the criteria to filter out the undesired extremal regions. However, these criteria require empirical selection of the parameter values, which might limit the algorithm's applications. On the other hand, Arteta *et al.* [92] have formulated the region selection an optimization problem and proposed a more general framework for nucleus/cell detection on multiple microscopy modalities including bright field, fluorescence, and phase contrast. Specifically, it first generates a set of candidate cell-like regions using the MSER detector, then assigns a score to each candidate region using a statistical model with cell appearance, and finally, selects a set of nonoverlapping regions matching the model

using dynamic programming by maximizing the total scores. This framework is extended to handle tightly overlapping cells in [75], which can identify the blobs corresponding to multiple overlapping objects, and this method have also been applied to cell detection in time-lapse microscopy image sequences [93]. Similarly, Bise and Sato [76] have used this "generate, scoring, and select" strategy to detect cells in DIC microscopy images and 3-D image data. The main differences are that it uses multilevel thresholding to create candidate regions and binary linear programming to maximize the scores for region selection.

### F. HT

Since nuclei usually exhibit circular or elliptical shapes in pathological images, HT [94], [95] based nucleus detection has attracted many research interests. In the 2-D  $xy$ -plane (it can be easily extended to 3-D representation), a circle with center at  $(a, b) = (a_0, b_0)$  and radius equal to  $r = r_0$  is presented by

$$(x - a_0)^2 + (y - b_0)^2 = r_0^2. \quad (7)$$

For each point on the circle, the loci for the parameters  $(a, b, r)$  form a cone in the parameter space, and the cones corresponding to all the circle points pass through a common point  $(a_0, b_0, r_0)$ , which represents the location and the size of the circle in the  $xy$ -plane. For a specific radius  $r_0$ , this discrete voting strategy actually produces a vote distribution in the Hough-transformed image, and the point at pixel  $(a_0, b_0)$  collects the most votes and exhibits the highest value. In [96], the HT has been generalized to deal with arbitrary shapes. Therefore, based on the nucleus/cell edges, HT can locate the targets by seeking peaks in the transformed parameter space. The search space can be narrowed down by introducing the gradient direction into the voting procedure [96].

Ramesh *et al.* [97] have first thresholded the haematopoietic cell regions in bone marrow images, and then, applied the circular HT to haematopoietic cell detection. Zanella *et al.* [98] have first applied the Canny edge detector [99] to confocal images of zebrafish embryogenesis, and thereafter, used the 3-D HT with a range of predefined radius values and a variation of the gradient direction to identify the nucleus centroids, which are recognized by detecting the local maxima in the Hough space. Bergmeir *et al.* [77] have applied a randomized HT to Canny detector-generated edge maps for nucleus detection, which serves as contour initialization for subsequent level-set-based nuclei segmentation in cervical images. In order to enhance the robustness, it performs mean-shift filtering for noise elimination before edge detection. Some other similar methods directly using the HT-generated local maxima as the nucleus locations can be found in [100] and [101].

However, the HT might generate false peaks due to image noise, incorrect edge extraction, or touching objects. Therefore, it is necessary to perform further analysis to remove the false detection. Ortiz De Solorzano *et al.* [102] have proposed a nucleus detection algorithm based on the 3-D generalized HT, which consists of the following major steps: 1) calculate the magnitude and the direction of the image gradient with a  $3 \times 3$  Sobel filter, 2) use the HT to generate the transformed image that records the votes, 3) exploit a Gaussian filter to remove



**Algorithm 3: HT-based cell detection in [103]**

1. Detect good cell edges with the pixel-wise classifier (Ilastik) [104]
2. Use the generalized HT to generate the transformed image
3. Employ a Gaussian filter to smooth the transform image and obtain continuous votes
4. Extract local maxima regions with HAT
5. Identify those maxima regions centered at real cells with ILP

noises in the transformed image, and 4) extract the peaks in the image to be the nucleus locations by using morphological reconstruction [58]. Instead of relying on Gaussian smoothing and morphology operation, Filipczuk *et al.* [78] have evaluated the HT-generated candidate circles using an SVM classifier with three features: 1) the average intensity inside the circle, 2) the long run high gray-level emphasis texture, and 3) the percentage of nuclei pixels according to the nuclei mask. This algorithm has been validated using breast cancer cytological images and produced encouraging performance. For yeast cell detection in bright-field microscopy images [103], ILP is used to refine the detection produced by the HT, and the details of this approach are listed in Algorithm 3. In particular, the optimization problem is solved by minimizing the shortest Euclidean distance between the edge elements and the cell center candidates.

**G. Radial-Symmetry-Based Voting**

Radial symmetry transform [105], [106], which is designed to detect points of interest, can be used to locate the centroids of nuclei or cells. Nevertheless, the high computational complexity limits its practical applications. Fortunately, Loy and Zelinsky [107] have proposed a FRST to significantly decrease the time cost such that it is well suitable for real-time vision applications. It maps an input image into a transformed image in which the points with high radial symmetry is highlighted. In other words, these points collect higher responses than the others. Specifically, for each radius  $r \in R = \{r_1, \dots, r_N\}$ , FRST votes along the direction of image gradient at each point  $\mathbf{p}$  to determine the positively affected pixel  $\mathbf{p}_{+ve}(\mathbf{p})$  and negatively affected pixel  $\mathbf{p}_{-ve}(\mathbf{p})$

$$\mathbf{p}_{+ve}(\mathbf{p}) = \mathbf{p} + \text{round} \left( \frac{\mathbf{g}(\mathbf{p})}{\|\mathbf{g}(\mathbf{p})\|_2} r \right) \quad (8)$$

$$\mathbf{p}_{-ve}(\mathbf{p}) = \mathbf{p} - \text{round} \left( \frac{\mathbf{g}(\mathbf{p})}{\|\mathbf{g}(\mathbf{p})\|_2} r \right) \quad (9)$$

where  $\mathbf{g}(\mathbf{p})$  represents the gradient at  $\mathbf{p}$  and the *round* operator rounds each vector element to its nearest integer. Based on these pixels, an orientation projection image  $O_r$  and a magnitude projection image  $M_r$  are generated as follows: for each positively (or negatively)-affected pixel, the corresponding point  $\mathbf{p}_{+ve}$  (or  $\mathbf{p}_{-ve}$ ) in  $O_r$  and  $M_r$  is increased (or decreased) by 1 and  $\|\mathbf{g}(\mathbf{p})\|_2$ , respectively. Thereafter, the radial symmetry

transform is defined as

$$S = \frac{1}{N} \sum_{r \in R} S_r = \frac{1}{N} \sum_{r \in R} F_r * A_r \quad (10)$$

$$F_r(\mathbf{p}) = \frac{M_r(\mathbf{p})}{k_r} \left( \frac{|\hat{O}_r(\mathbf{p})|}{k_r} \right)^\alpha \quad (11)$$

where  $A_r$  is a 2-D Gaussian kernel, and  $\hat{O}_r(\mathbf{p}) = O_r(\mathbf{p})$  if  $O_r(\mathbf{p}) < k_r$ , otherwise  $k_r$ .  $\alpha$  controls the radial strictness, and  $k_r$  is a scaling factor.

Veta *et al.* [108] have applied the FRST to nucleus detection in H&E-stained breast cancer images. However, the FRST might produce false peaks in the transformed image due to clustered nuclei, and the radius range needs careful selection to handle nucleus scale variations. In addition, many nuclei or cells exhibit elliptical but not circular shapes, thereby presenting significant challenges for the FRST. In [109], a distance-based non-maximum suppression method is used to refine the FRST-generated candidate nucleus centroids in FISH images. For centroblast detection in follicular lymphoma images [79], it first uses the FRST to generate a set of candidate cell regions (combined with the foreground segmentation), then calculates the size, eccentricity, and Gaussian distribution of the gray-level run length matrix features, and finally, picks the true centroblasts by applying thresholding values to these measurements for refinement. On the other hand, Ni *et al.* [110] have generalized the FRST to directly handle elliptical objects by introducing an affine transform into (8) and (9)

$$\mathbf{p}_{+ve}(\mathbf{p}) = \mathbf{p} + \text{round} \left( \frac{\hat{V}_{q(\phi)}}{\|\hat{V}_{q(\phi)}\|_2} r \right) \quad (12)$$

$$\mathbf{p}_{-ve}(\mathbf{p}) = \mathbf{p} - \text{round} \left( \frac{\hat{V}_{q(\phi)}}{\|\hat{V}_{q(\phi)}\|_2} r \right) \quad (13)$$

$$\hat{V}_{q(\phi)} = G \cdot M \cdot G^{-1} \cdot M^{-1} \cdot \mathbf{g}(\mathbf{p}) \quad (14)$$

where  $G$  represents the affine transform matrix, and  $M = [0 \ 1; -1 \ 0]$ . The generalized FRST can effectively detect elliptical nuclei in H&E histopathological images. However, it introduces new parameters for the affine transform.

Instead of using the interest-point operators, Parvin *et al.* [111], [112] have proposed an iterative voting approach, which is adaptive to geometric perturbation and can handle elliptical objects. It defines a set of cone-shaped kernels that vote iteratively for the likelihood of the object centers. These kernels are initially aligned along the gradient direction, and within each iteration, their orientations are aligned along the maximum responses of the voting space and their shapes are updated by reducing the size. In this scenario, the object center is iteratively refined until it converges to a single response. Formally, let  $I(x, y)$  denote the original image, and  $\nabla I(x, y)$  be the gradient, for each pixel  $(x, y)$ , the algorithm defines its voting area  $A$  with vertex at  $(x, y)$ , radial range  $[r_{\min}, r_{\max}]$  and angular range  $\Delta$ , the gradient magnitude-based iterative voting updates



---

**Algorithm 4:** Radial-symmetry-based iterative voting in [111]

---

1. Initialize  $r_{\min}, r_{\max}, \{\Delta_N, \dots, \Delta_0\}$  ( $\Delta_i > \Delta_{i-1}$ , and  $\Delta_0 = 0$ ), gradient threshold  $\Gamma_g$ , vote threshold  $\Gamma_v$  and variance parameter  $\sigma$ . Set  $\Delta_n = \Delta_N$  and  $\alpha(x, y) = -\frac{\nabla I(x, y)}{\|\nabla I(x, y)\|}$
  2. **Repeat**
  3. Set  $V(x, y; r_{\min}, r_{\max}, \Delta_n) = 0$ , and for each pixel  $(x, y) \in \{(x, y) | \|\nabla I(x, y)\| > \Gamma_g\}$ , update  $V(x, y; r_{\min}, r_{\max}, \Delta_n)$  using (15)
  4. Update the voting direction  $\alpha(x, y) = \frac{(u^* - x, v^* - y)}{\sqrt{(u^* - x)^2 + (v^* - y)^2}}$ , where  $(u^*, v^*) = \arg \max_{(u, v) \in A} V(x, y; r_{\min}, r_{\max}, \Delta)$
  5.  $n = n - 1$
  6. **Until**  $n = 0$
  7. Calculate the centers of the objects as  $C = \{(x, y) | V(x, y; r_{\min}, r_{\max}, \Delta) > \Gamma_v\}$
- 

the vote image  $V(x, y; r_{\min}, r_{\max}, \Delta)$  as

$$V(x, y; r_{\min}, r_{\max}, \Delta) = V(x, y; r_{\min}, r_{\max}, \Delta) + \sum_{(u, v) \in A} \|\nabla I(x + u, y + v)\| K(u, v; \sigma, \alpha, A) \quad (15)$$

$$A := \{(x \pm r \cos \psi, y \pm r \sin \psi) | r_{\min} \leq r \leq r_{\max}, \theta(x, y) - \Delta \leq \psi \leq \theta(x, y) + \Delta\} \quad (16)$$

where  $K(u, v; \sigma, \alpha, A)$  is a 2-D Gaussian kernel with variance  $\sigma^2$ , masked by  $A$  and oriented in the voting direction  $\alpha(x, y) := (\cos(\theta(x, y)), \sin(\theta(x, y)))$ . The detailed steps of the approach are listed in Algorithm 4.

This iterative voting technique has been used to detect the centers of yeast cells in DIC microscopy images [113] and red blood cells in bright-field microscopy images [114]. A similar approach applicable to gray level images is reported in [115] to decompose cell clusters in histopathological images, which updates the vote image with a weighted combination of the gradient magnitude and the gray value image. In addition, a median filter is used to smooth the final vote landscape for facilitating local maxima seeking. Another iterative method, namely regularized centroid transform [116], has been reported to locate clustered nuclei in fluorescence microscopy images. It moves the boundary points to the local object center along a minimum energy path, which is regularized with a smoothness constraint. Instead of conducting iterative voting, Qi *et al.* [80] have proposed a single-pass voting to detect the nucleus on breast cancer TMA and blood smear images, which performs only one round of voting and computes the nucleus centers by applying the mean shift clustering [117] to the vote image. The marker detection results using this method on several sample images are shown in Fig. 1. Considering the nucleus scale variations, a single-pass voting with multiple scales is presented for nucleus locating in H&E-stained lung cancer images [81], [118]–[120] and IHC-stained pancreatic NET images [82], [121]. In [83], a similar

single-pass voting is applied to only touching or overlapping nuclei that are discriminated from those isolated nuclei by using ellipse descriptor analysis, and thus, reduces the number of voting points. All of these radial-symmetry-based voting methods require a careful choice of the parameters defining the voting areas.

## H. Supervised Learning

To deal with complex nature of pathology (especially histopathology) images, nowadays supervised learning-based methods have attracted much attention. Supervised learning is a machine learning technique aiming to infer a mapping function or model from training data [130]. The nucleus/cell detection is usually formulated as a pixel/voxel-wise or superpixel/supervoxel-wise classification problem, and a specific model is learned to map new data examples into discrete labels. Many classifiers with various feature representations are presented in the literature, and here, we mainly focus on SVM, random forests, and deep neural networks, which are nowadays very popular in nucleus or cell detection.

**1) SVM:** Traditionally, an SVM is a nonprobabilistic binary classifier, aiming to find a hyperplane with a maximal margin to separate high-dimensional data points [131]. Given a set of training data  $\{(\mathbf{x}_i, y_i)\}_{i=1}^N$ , where  $\mathbf{x}_i \in R^p$  and  $y_i \in \{1, -1\}$ , an SVM solves the following problem:

$$\min_{\mathbf{w}, b, \xi} \frac{1}{2} \mathbf{w}^T \mathbf{w} + C \sum_{i=1}^N \xi_i,$$

$$s.t. y_i (\mathbf{w}^T \phi(\mathbf{x}_i) + b) \geq 1 - \xi_i, \xi_i \geq 0 \forall i \quad (17)$$

where the  $\phi(\mathbf{x})$  maps the data points into a high-dimensional space.  $C > 0$  is a penalty parameter to control the violation, which is represented by the slack variables  $\xi$ .

Su *et al.* [122], [132] have applied a binary SVM classifier to automatic myonuclear detection in isolated single muscle fiber fluorescence images. It consists of four major steps: 1) extract foreground edges by applying Otsu's method [63] to the fused z-stack image, 2) fit a sufficient number of ellipse hypotheses using heteroscedastic Errors-in-variable regression [133], 3) use an SVM with a set of specifically designed ellipse features to select the good candidate fittings, and 4) apply inner geodesic distance-based clustering to ellipse refinement, which determines the locations of myonuclear centers. In [134], a linear SVM classifier with RGB-value feature representation is exploited to detect nuclei in H&E-stained prostate images, along with a nonmax suppression heuristic. Mao *et al.* [123] have proposed a supervised learning approach for nucleus detection and segmentation in bladder cancer images. First, it trains a linear SVM classifier to convert color images into gray-level images, and then, uses Otsu's method [63] to segment out the nucleus regions. Second, it extracts the intensity values along the valley lines between minima from both gray-level and complemented distance images, and learns another SVM classifier (with selected features by an orthogonal sequential forward search method), which is used to merge falsely detected minima. Another two-step supervised learning method [135] is reported

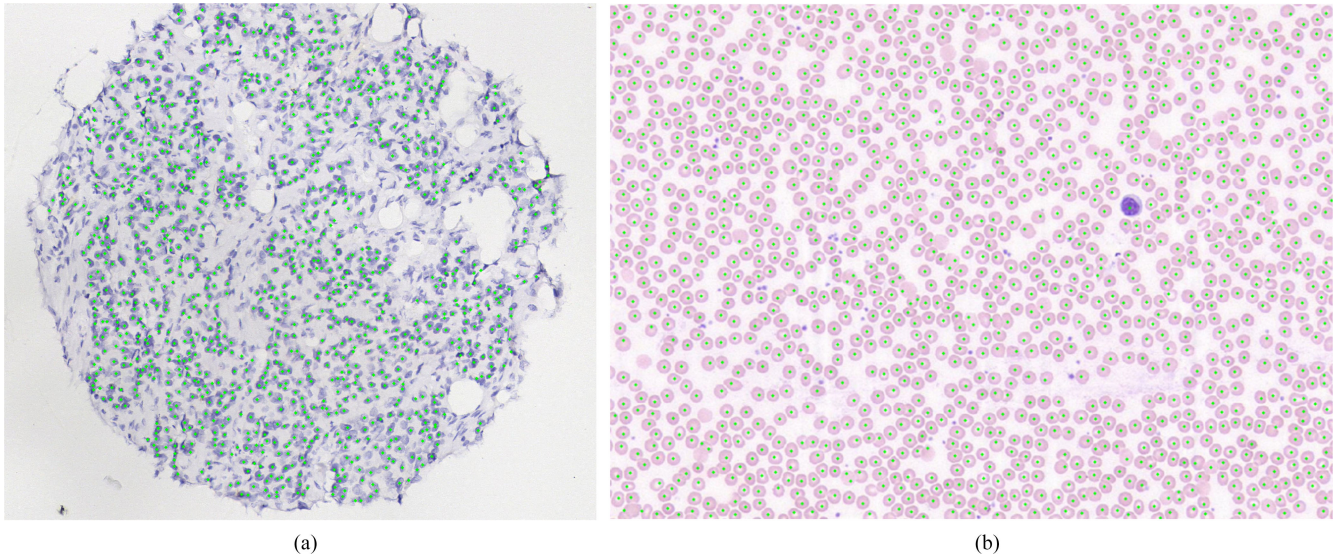


Fig. 1. Marker detection results using [80] on two sample images from breast cancer and blood smear datasets. The green dots represent the detected seeds. The breast cancer image is acquired at  $10\times$  objective magnification. Note that seed detection is performed only on the segmented epithelial regions [80]. The blood smear image is acquired at  $40\times$  objective magnification. (a) Breast cancer. (b) Blood smear.

for mitotic cell detection in H&E-stained breast cancer images. In the first stage, a random forest classifier [104] with local intensity and gradient information is learned to obtain a number of candidates, and then, adopts local adaptive thresholding to segment out these candidates. In the second stage, a Gaussian kernel-based SVM model with global cell features [136] is used for final prediction. Khan *et al.* [137] have presented a learning approach for mitotic cell detection in breast cancer histopathology images, which models image intensities with a Gamma-GMM and performs pixel-wise classification in testing images, then generates a set of candidate regions, and finally, distinguishes mitotic from nonmitotic cells using an SVM classifier with a set of texture features.

**2) Random Forests:** Random forests [138] are popular due to fast training and testing, and fair error tolerance in training data. A decision forest  $\mathcal{F} = \{T_t\}$  is an ensemble of decision trees  $T_t$ , which are trained independently on randomly selected samples  $S = \{s_i = (\mathbf{x}_i \in \mathcal{X}, y_i \in \mathcal{Y})\}$ , where  $\mathcal{X}$  and  $\mathcal{Y}$  denote the spaces of input features and output labels, respectively. For each node  $n$  in a decision tree, a split function  $h(\mathbf{x}, \theta^n)$  is chosen to split the samples  $S^n$  into left  $S_L^n$  or right  $S_R^n$ , and it is optimized by maximizing the information gain

$$S^n = H(S^n) - \left( \frac{|S_L^n|}{|S^n|} H(S_L^n) + \frac{|S_R^n|}{|S^n|} H(S_R^n) \right) \quad (18)$$

where  $H(\cdot)$  is the class entropy function. The split function  $h(\mathbf{x}, \theta^n)$  is often chosen as a stump function for efficiency [139]. The training procedure persistently splits the samples until either a maximal depth is reached, or too few samples are left, or information gain falls below a certain threshold. In runtime testing, a decision tree  $T_t(\mathbf{x})$  produces the predictions by recursively branching a feature sample  $\mathbf{x} \in \mathcal{X}$  left or right down the tree until a leaf node is reached, and a majority voting or an

average is applied to the predictions of all the decision trees for classification or regression.

Mualla *et al.* [124], [140] have applied a random forest to cell detection in microscopy images. It is composed of five major stages: 1) extract keypoints using SIFT [141], 2) discriminate cell keypoints with a BRF [142] that uses bootstrap sampling to handle imbalanced training data, 3) classify the cell keypoints into two categories corresponding to inner profiles and cross profiles using a BRF to measure the similarity between keypoints, 4) apply agglomerative hierarchical clustering to the keypoints based on the similarity, and 5) calculate the weighted mean of keypoints as the final location of cell center for each cluster. The difference is that the keypoint features and the profile features in [140] are calculated from the transport of intensity equation solution or the low-pass monogenic local phase images, while defocused images are used in [124].

Gall *et al.* [143], [144] have introduced a general object detection algorithm, namely Hough forests, which constructs discriminative class-specific part appearance codebooks based on random forests that are able to cast probabilistic votes within the HT framework. In [145], Hough forests are incrementally trained to detect mitotic cells in DIC microscopy images. For random forests training, a set of small patches  $S = \{s_i\}$  are randomly sampled from bounding-box annotated image data. Each patch  $s_i$  is associated with a class label  $c_i$  and an offset vector  $\mathbf{d}_i$  of the patch center to the bounding-box center. A node  $n$  is randomly assigned as a classification or regression node, whose objective function (19) or (20) is

$$H(S^n) = - \sum_{c \in \{\text{pos}, \text{neg}\}} p(c|S^n) \log(p(c|S^n)) \quad (19)$$

$$H(S^n) = \frac{1}{|\{\mathbf{d}_i : c_i = \text{pos}\}|} \sum_{\mathbf{d}_i : c_i = \text{pos}} \|\mathbf{d}_i - \bar{\mathbf{d}}\|_2^2 \quad (20)$$



where  $p(c|S^n)$  is the percentage of samples with label  $c$  in  $S^n$ , and  $\bar{d}$  is the mean of offsets  $d_i$  of the positive samples in  $S^n$ . After the tree is built with (18), a split function is stored at each node, and the patches arriving at the leaf nodes have low variations in both class labels and offsets. Therefore, the leaves, which store the positive offsets, can cast probabilistic votes with low uncertainty about the existence of object centroids near the patch [144]. In order to handle an interactive annotation task, the Hough forest is trained in an incremental way similar to the online learning of Hough forests [146], with the exception that the leaves additionally store the patches [145].

**3) Deep Neural Networks:** Deep learning-based models, especially CNN, have attracted particular attention recently [147]–[149]. Different from SVM and random forests that rely on hand-crafted features for object classification, CNN can automatically learn multilevel hierarchies of features that are invariant to irrelevant variations of samples while preserving relevant information [150], [151], and has achieved great success on image classification and scene labeling [152], [153]. A CNN usually consists of successive pairs of convolutional and pooling layers, followed by several fully connected layers. A convolutional layer learns a set of convolutional filters, which will be used to calculate output feature maps, with each convolutional filter corresponding to one output feature map. The pooling (often chosen as max-pooling) layer summarizes the activities and picks the max values over a neighborhood region in each feature map. The fully connected layer learns more higher level feature representation and the last is often a softmax layer (fully connected), which outputs the probability that the input patch belongs to a certain category [154].

Ciregan *et al.* [155] have applied a deep CNN to automatic mitotic cell detection in breast cancer histology images. With raw intensities of the testing image, the CNN provides a probability map, in which each pixel value is the probability of the centroid of a mitotic cell. Next, the probability map is smoothed with a disk kernel and final centroid detection is obtained with nonmaxima suppression. Similarly, a nine-layer CNN [156] followed by nonmaxima suppression is applied to cell detection in wide-field microscopy zebrafish images, which are converted into the YUV color space, and a seven-layer CNN [157] is used to locate circular tumor cells in both fluorescence and phase-contrast microscopy images. In [125], Xing *et al.* have learned three different CNN models corresponding to brain tumor, pancreatic NET, and breast cancer pathology images, respectively, which are applied to automated nucleus detection. Instead of using a simple nonmaxima suppression for detection refinement, Liu and Yang [158] have formulated pancreatic neuroendocrine and lung cancer nucleus detection into an optimization problem. Specifically, it consists of the following three steps: 1) generate a set of nucleus candidates using different methods including LoG [67], MSER detection-based structure learning [92], and iterative voting [111], 2) score each candidate using a seven layer CNN, and 3) select a best subset of candidates using maximum-weight independent set. Considering scale variations in nuclei, Song *et al.* [126] have proposed a multiscale CNN framework-based nucleus detection in H&E-stained cervical images, which is composed of 1) extracting

feature representation with a three-scale CNN and applying it to a two-layer neural network for pixel-wise coarse segmentation, 2) building an undirected graph based on the coarse segmentation and superpixels generated from the simple linear iterative clustering (SLIC) [159] and partitioning the graph with a fast min-cut/max-flow algorithm [160], and 3) finally, calculating nucleus markers based on the marker seeking strategy in [161].

If CNN models are applied to testing images in a sliding-window manner for pixel-wise classification, it will be computationally expensive for large-scale images. In [162], a fast scanning strategy [163] is introduced to a deep CNN, which is learned to detect pancreatic nuclei in bright-field microscopy images. Inspired by [143] and [144], the CNN model in [162] learns an implicit Hough-voting codebook, which consists of a set of pairs of offset vectors and confidence. For a testing image, fast scanning is used to perform the convolutional operations on the entire image so that the computational complexity can be significantly improved. Each testing patch votes toward several directions with specific voting confidences, and all the votes from the image are collected in an additive way and finally a Patch-window is used to estimate the voting densities as final nucleus locations. Furthermore, Xie *et al.* [164] have extended the conventional CNN-based classification to structure regression for nucleus and cell detection, which generates proximity patches with the fast scanning technique [163]. Let  $\mathcal{X}$  denote the patch space, which consists of a set of  $d \times d \times c$  local image patches extracted from  $c$ -channel images  $I$ . An image patch  $\mathbf{x} \in \mathcal{X}$  centered at  $(u, v)$  is represented by a quintuple  $\{u, v, d, c, I\}$ . It defines  $\mathcal{M}$  as the proximity mask corresponding to image  $I$ , and computes the  $ij$ th entry in  $\mathcal{M}$  as

$$\mathcal{M}_{ij} = \begin{cases} \frac{1}{1 + \alpha D(i, j)}, & \text{if } D(i, j) \leq r \\ 0, & \text{otherwise} \end{cases} \quad (21)$$

where  $D(i, j)$  represents the Euclidean distance from pixel  $(i, j)$  to manually annotated nucleus or cell center,  $r$  is a distance threshold (selected as 5 pixels), and  $\alpha$  is the decay ratio (set as 0.8). Given training data  $\{(\mathbf{x}^i, \mathbf{y}^i) \in (\mathcal{X}, \mathcal{Y})\}_{i=1}^N$ , where  $\mathcal{Y} \subset \mathcal{V}^{p \times 1}$  represents the output space of the structured regression model ( $p = d' \times d'$  is the number of units in the last layer), and denoting  $\{\theta_l\}_{l=1}^L$  the parameters corresponding to each of the  $L$  layers, the training process of the structured regression model can be formulated as learning a mapping function  $F$  represented by  $\{\theta_l\}_{l=1}^L$ , which maps the image space  $\mathcal{X}$  to the output space  $\mathcal{Y}$ . Therefore, the optimization problem can be formulated as

$$\arg \min_{\theta_1, \dots, \theta_L} \frac{1}{N} \sum_{i=1}^N \mathcal{L}(\psi(\mathbf{x}^i; \theta_1, \dots, \theta_L), \mathbf{y}^i) \quad (22)$$

where  $\mathcal{L}$  is a user-defined loss function [164]. Back propagation [150] is used to learn the model parameters. To generate the proximity map, the learned CNN structure model is applied to a testing image with fast scanning. Each image pixel receives  $d' \times d'$  predictions from its neighboring pixels, and the average is used as its final proximity value. Finally, nucleus or cell centers are obtained by seeking local maxima in the average

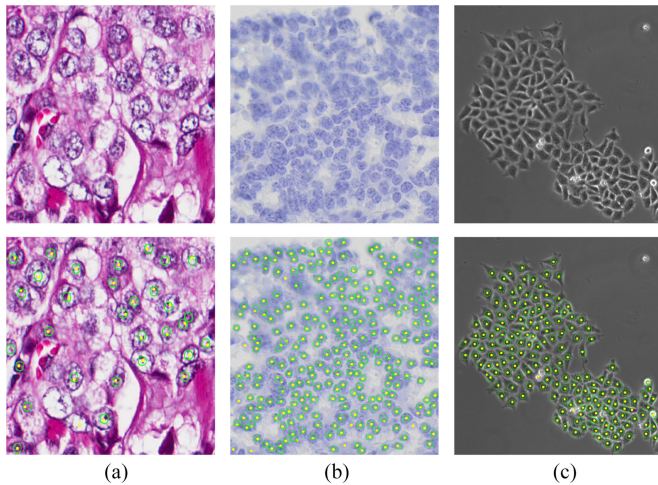


Fig. 2. Marker detection results using [164] on three sample images from breast cancer, pancreatic NET, and HeLa cell datasets, respectively. Original images are shown in the top row, and their corresponding detections are represented as yellow dots in the bottom row. The breast cancer and NET images are captured at 40 $\times$  and 20 $\times$  objective magnification, respectively. The HeLa cell line image is obtained from [92]. (a) Breast cancer. (b) NET. (c) HeLa.

proximity map. This approach has been successfully applied to cell detection in breast cancer, pancreatic NET, and HeLa cell images, and the detection results on several sample images are shown in Fig. 2.

**4) Others:** A supervised learning-based template matching technique is applied to nucleus seed detection on fluorescence and bright-field microscopy images [127], [165]. In the training stage, it learns a statistical model for nucleus texture and shapes with PCA. In the testing stage, it applies this model to the image for detection map generation, and then, locates the nucleus Centroids with distance-based nonmaximum suppression. In [166], sparse reconstruction-based template matching is used to locate nuclei in H&E-stained lung cancer and brain tumor images. It exploits K-selection [167] to learn a nucleus patch dictionary, which is used to perform sparse reconstruction with trivial templates for testing images and generate corresponding probability maps. The mean-shift clustering [117] with weighted data is applied to final nucleus center detection. Both of these approaches can produce encouraging performance, but they locate nuclei with a sliding window technique, which might be computationally expensive on large-size images.

Dong *et al.* [128] have proposed a Bayesian-classification-based leukocyte detection algorithm on intravital microscopy images, which is composed of three steps: 1) conduct ellipse matching to produce maximal gradient inverse coefficient of variation (GICOV), 2) refine cell contours using B-spline snake with the GICOV constraint, and 3) retain the optimal contours based on a learned Bayesian classifier. A mitotic cell detection method presented in [129] learns a discriminative dictionary with sparse representation and conducts mitosis classification based on the sparse reconstruction errors [168]. In [169], a graphics-processing-unit-based two-layer artificial neural network is used to efficiently identify cells in 3-D bright-field microscopy images. Raw voxel intensities are extracted and the dimensionality is reduced by the PCA. It performs voxel-wise

classification on a parallel computing platform so that it can produce high-throughput cell detection.

### III. NUCLEUS AND CELL SEGMENTATION METHODS

Nucleus/cell segmentation aims to separate individual nuclei/cells with delineating their boundaries. This is very important for extracting cellular morphology features or texture, which could be potentially used to identify and grade diseases. Broadly, there exist three popular strategies for nucleus/cell segmentation [18]: 1) *separate* the foreground from the background, and then, *split* the object clumps, if present, into individual nuclei or cells, 2) *identify* markers of nuclei or cells, and then, *expand* the markers to the object boundaries, and 3) *generate* a sufficient number of region candidates, and then, *select* the best ones as final segmentation. Although some other procedures might have been also proposed, the major current nucleus/cell segmentation methods are covered by these three strategies. On the other hand, the vast majority of methods are based on a few underlying algorithms: intensity thresholding, morphology operation, watershed transform, deformable models, clustering, graph-based methods, and supervised classification. We summarize the recent state of the arts based on these categories as follows. Similar to the marker detection methods, in real applications, a segmentation approach may combine some of these algorithms as well as other methods to produce satisfactory performance. Note that in Tables II–VI, we list only the segmentation metrics if no specific quantification for segmentation performance exists in the publications.

#### A. Intensity Thresholding

Intensity thresholding might be the first and simplest method for nucleus/cell segmentation. Based on the assumption that the intensity distributions of nuclei/cells and the background are sufficiently and consistently distinct [53], the image can be converted into a binary image using a global threshold or locally adaptive thresholds. It is usually empirical to select the threshold level, which highly depends on the specific images. Alternatively, Otsu's method [63] performs statistical discriminant analysis of the image intensity histograms, and chooses an optimal threshold value by maximizing the interclass variance. In order to deal with noise or nonuniform illumination, local thresholding has been introduced for segmentation. One strategy for local thresholding is to divide the image into multiple subimages, and then, binarize each subimage with a threshold value; alternatively, one can also compute a threshold at each point in its neighboring region [53], [170]. However, compared with global thresholding, local thresholding requires an additional parameter to define the local region size.

In microscopy imaging (e.g., fluorescence), nuclei are sometimes brightly stained in a relatively uniform dark background such that a single global threshold can be used as the first step of nuclei segmentation [171]–[173], and further analysis is conducted to separate touching or overlapping nuclei. Callau *et al.* [174] have first empirically converted the RGB color images into grayscale images and then employed a threshold to segment the epithelial cell areas for cytokeratin-19 evaluation in breast cancer TMA images. In order to obtain individual cells, it



TABLE V  
SUMMARY OF JOURNAL PUBLICATIONS BASED ON THE UNDERLYING ALGORITHMS OF SEGMENTATION METHODS

	Data	SEG	SEG Results
[177]	20 HeLa cell line images	adaptive thresholding, watershed	CSR/USR/OSR: 98.43%/0.43%/1.14%
[178]	images of <i>C. elegans</i> (C), human skin (H), benign human breast tissue (B), breast cancer cell line (L), and invasive human breast carcinoma (I)	local adaptive thresholding, watershed	CSR: 98.9% (C), 94.7% (H), 93.7% (B), 88.7% (L), 65.8% (I)
[180]	10 zebrafish predomitic mesoderm (Zeb), 5 H4 neuroglioma (H4), and 9 HeLa cell nuclei images	gradient flow tracking, local adaptive thresholding	USR/OSR: 1.17%/1.9% (Zeb), 0.88%/1.22% (H4), 1.26%/1.44% (HeLa)
[182]	7931 cells of breast cancer, bone marrow, liver, kidney, and intestinal mucosa	contour tracing, color deconvolution, thresholding	precision/recall/conglomerate score: 90.8%/85.9%/95.3%
[184]	5 time-lapse image datasets	wavelet-based watershed	precision: 99.98%, recall: 99.97%
[185]	10 rat brain cell nuclei images	watershed	CSR: 96.3%
[186]	17 rat brain nuclei image stacks	watershed	CSR: 93.7% $\pm$ 3.3%
[187]	55 image stacks of <i>C. elegans</i> cells	watershed	accuracy: 89%
[188]	5 2-D time-lapse series of rat adipose-derived mesenchymal stem cell (2-D) and 7 3-D series of human lung squamous cell carcinoma (3-D) images	level set (LS), graph cut (GC)	Jaccard coefficient: 95.55% (2D-LS), 86.28% (3-D-LS), 96.36% (2-D-GC), 86.89% (3-D-GC)
[189]	3 HeLa and 1 CHO cell image sequences	level set	precision/recall/F <sub>1</sub> -score
[190]	6 <i>Drosophila</i> cell images	level set	relative region coincidence: > 92%
[191]	more than 1000 HeLa cells	level set	HD: 1.9 $\pm$ 1.1, MAD: 0.57 $\pm$ 0.22
[192]	48 U2OS, 49 NIH3T3, 7 N1E115, and 16 <i>Drosophila</i> (DRO) cell images	level set	Dice/NSD/HD: 94%/5%/12.8 (U2OS), 85%/12%/14.2 (NIH3T3), 90%/10%/6.7 (N1E115), 82%/19%/4.0 (DRO)
[193]	100 lymphocytes in breast histopathology	level set	HD/MAD: 2.1/0.9
[194]	440 GBM tumor images	level set	precision/recall/F-measure: 71%/79%/74.8%
[195]	800 breast cancer lymphocytes	level set	HD/MAD: 2.1/1.1
[196]	536 benign white blood cell (benign), 397 B-cell chronic lymphocytic leukemia (CLL), 543 mantle cell lymphoma (MCL), and 315 follicle-center cell lymphoma (FCC) images	color GVF	accuracy rate: 97.10% (nuclei-benign), 92.94% (cytoplasm-benign), 93.56% (nuclei-CLL), 91.83% (cytoplasm-CLL), 90.09% (nuclei-MCL), 87.92% (cytoplasm-MCL), 91.2% (nuclei-FCC), 89.57% (cytoplasm-FCC)

TABLE VI  
SUMMARY OF JOURNAL PUBLICATIONS BASED ON THE UNDERLYING ALGORITHMS OF SEGMENTATION METHODS

	Data	SEG	SEG Results
[266]	4635 nuclei of cervical cells and mammary invasive ductal carcinomas	EM	CSR/USR/OSR: 97.52%/0.26%/2.22%
[267]	20 breast cancer histopathological images	normalized cut	Euclidean distance error: 1.12 $\pm$ 0.71, absolute difference error: 16.75 $\pm$ 7.47 (tolerance radius is 2)
[268]	12 fetal and maternal red blood cell images	normalized cut	undercounted: < 1.7%, over-counted: < 0.9%
[269]	3 sets of cytological smear images (each with 64 images)	CRF	Dice: 90%
[270]	16 Huh7 and 21 HepG2 cell line human hepatocellular carcinoma images	attributed relational graph	precision/recall/F <sub>1</sub> -score: 88.14%/88.44%/88.29% (nucleus-based-Huh7), 78.28%/85.51%/81.74% (pixel-based-Huh7), 81.41%/79.19%/80.28% (nucleus-based-HepG2), 65.75%/75.37%/70.24% (pixel-based-HepG2)
[271]	21 follicular lymphoma images	KNN classifier, concave point-based clump split	$\frac{A_{sg} \cap A_{gt}}{A_{sg} \cup A_{gt}} = 76.9\%$
[272]	111 skeletal muscle images	multiclass SVM, concave point-based clump split	precision/recall/F <sub>1</sub> -score: 60%/66%/62%

needs further processing to split the cell areas. In [175], a global threshold is used to segment isolated nuclei in cervical images and then incremental thresholding is applied to clustered nucleus separation with a range of threshold levels. For each level, it selects those segmented regions as nuclei based on a set of predefined criteria. In order to enhance the bimodal intensity distribution for the Otsu's-method-based image segmentation, a multiscale filter is used to improve intensity contrast [176] and a supervised SVM classifier is learned to convert color images to gray-level images [123]. Zhou *et al.* [177] have adopted an adaptive thresholding based on a local window to binarize HeLa cell line images, Ortiz De Soloranzo *et al.* [178] have used a locally adaptive thresholding method to segment nuclear

regions in 3-D confocal microscopy images, and another adaptive thresholding-based method [179] is evaluated on whole-slide lung cytology images. Li *et al.* [180] have applied Otsu's method [63] to local small regions, which are segmented in advance by using an elastic deformable model [181] in the diffused GVF. In [182], Otsu's method [63] is applied to color deconvolution segmented images for cell segmentation across different types of tissues. The whole procedure consists of six steps: 1) detect all possible closed contours with a contour tracing algorithm, 2) score each contour based on mean gradient magnitude and gradient fit, 3) generate a set of nonoverlapping regions by picking the locally prominent contours based on scores, 4) select the compact regions based on DT, 5) separate touching

nuclei using convex hull-based concave point detection, and 6) discriminate those regions corresponding to real nuclei from the others with color deconvolution [183] followed by Otsu's thresholding [63]. To achieve satisfactory segmentation performance, intensity thresholding usually needs to cooperate with other image analysis techniques, especially for touching or overlapping object cases.

### B. Morphology Operation

A mathematical morphology operation-based multiscale decomposition method is presented in [197] for cell segmentation in bright-field microscopy images. It consists of two steps: top-down erosion and bottom-up dilation. Specifically, starting from a thresholding-binarized image, it iteratively applies enhanced erosion operators with increasing scales to the image until obtaining the markers, and thereafter grows the markers with iterative dilation to reconstruct the original cell shapes, with preventing the markers from merging. However, this approach might fail in dense cell clumps and produce undersegmentation results. Wang *et al.* [198] have presented another iterative masked erosion and dilation approach to segment bacterial, yeast, and mammalian cells, but it enhances the procedure by modeling the object shapes, and then, selecting only those undecided regions for further proceeding within next iteration.

Mathematical morphology operation, especially gray-scale morphology, is used more often in image preprocessing to facilitate subsequent segmentation. In [199], a self-dual multiscale morphological toggle operator is derived from scale-space gray-scale morphology [200], and it is adopted to improve gradient images with edge enhancing, thereby yielding better cell segmentation accuracy in white blood cell images. The top-hat transform used to reduce the effects of color diffusion for cell segmentation is reported in [41] and gray-scale reconstruction is applied to cell clump splitting in [58].

### C. Watershed Transform

Watershed transform is the most popular region accumulation method, which starts from certain seed points and iteratively adds connected pixels to create labeled regions [201]. Viewing the image as a landscape with the intensity representing the elevation, watershed transform floods the landscape with water from regional minima, which correspond to areas of low elevation, and builds dams to prevent water merging when water in distinct catchment basins is going to meet. The flooding procedure continues until the water reaches the highest point in the landscape. The boundaries of the dams are called watershed lines, which split the landscape into regions [202]. Watershed transform is typically applied to gradient magnitude images, but it can also be used on gray intensity images, DT maps, and other gray-scale images. Nowadays, it attracts relatively more attentions than another region accumulation method called ordinary region growing [203].

Flooding from all the regional minima in gradient magnitude images, watershed transform might be prone to oversegmentation because of intensity variations in the foreground and the background. To tackle this problem, a practical approach,

marker-controlled watershed, is widely used for nucleus or cell segmentation. A (internal) marker is a connected component in the image, which corresponds to one object of interest [53]. With the constraint that the markers will be the only allowed regional minima, marker-controlled watershed can significantly alleviate the oversegmentation. Although manual marker labeling can be applied to watershed segmentation [204], it is inefficient for large-scale images. Therefore, the automated nucleus/cell detection methods discussed in Section II can be used to locate markers for watershed segmentation. For example, based on DT-generated markers, watershed is applied to distance maps [28]–[30], [50], intensity-fused distance maps [31], [32], and gradient-weighted distance maps [33] for nucleus segmentation in microscopy images. Another large set of nucleus segmentation methods using watershed in distance maps are reported in [41], [44], [48], and [61], which use HIT/HAT for marker detection. Other marker-controlled watershed segmentation methods use markers detected by morphology operation [35], [57], HT [103], radial-symmetry-based voting [83]. Besides DT maps, gradient information is also used in marker-controlled watershed transform, such as nuclei segmentation in H&E-stained histopathology images [108], H&E-stained cytology images [126], and fluorescence microscopy images [205]. Yang *et al.* [206] have applied marker-controlled watershed to gradient magnitude images for cell-like particle segmentation in low-SNR fluorescence images, in which markers can be easily detected on the noise-reduced gray-scale images with feature-preserving nonlocal means filtering. With supervised learning-based markers detection in [123], watershed transform is applied to overlapping nuclei separation in histology images; in [36], marker-controlled watershed transform is applied to ridge-enhanced intensity images for cell segmentation in 3-D fluorescence microscopy images. Recently, watershed transform is applied to cell segmentation in a wavelet coefficient space of fluorescence microscopy images, in which noise has been significantly reduced [184].

Another approach to deal with watershed's oversegmentation is to merge falsely segmented regions into components corresponding to real nuclei or cells based on certain predefined criteria. Although gradient-weighted DT is used for watershed segmentation in [33], oversegmentation is still inevitable in challenging images. Therefore, a statistical object model is introduced in [33] to merge undesired regions. First, it models the nucleus distribution with a multivariate Gaussian function in the feature space, which is spanned by cellular morphology and texture of nuclei; next, for each initial segment, it calculates a merging decision criterion by combining a confidence score from the Gaussian model and the average intensity gradient value; finally, it merges those regions with a threshold-based decision if the resulting segment can provides higher measurement score than single region before merging. In order to address the oversegmentation caused by watershed, Lin *et al.* [185] have represented the initial partition using a hierarchical merge tree and recursively searched for the candidates with maximum measurement scores, which correspond to real nuclei. Furthermore, multiple object models [186] are introduced to the framework [185] to handle various types of cell nuclei such as neuronal

and glial nuclei. For nucleus segmentation in 2-D prostate carcinoma images [43], [62], the mean intensity along the border is used to measure the strength and merge those weak-border regions, which are generated by applying marker-controlled watershed to gradient magnitude images. To eliminate false merging, it further applies watershed transform to the inverse DT maps, which are calculated from the previous segmentation. This approach is also adopted to segment nuclei in 3-D cervical fluorescence microscopy images [43]. Long *et al.* [187] have presented an automated segmentation method to assist annotation of 3-D *Caenorhabditis elegans* nuclei, and then, build a 3-D digital nuclear atlas, which can be used to automatically identify cells in new image stacks [207]. It merges watershed-based oversegmented regions and splits undersegmented regions using both a rule-based method with statistical information of the regions and an SVM-based classification with region geometry information.

Building a hierarchical merge tree from watershed oversegmentation and searching for the best candidate is actually an optimization problem of region selection. In [209], dynamic programming is used to segment muscle cells by selecting the optimal regions. The method consists of four major steps: 1) create an edge map using a gPb detector [210], 2) generate a sufficient number of segments using OWT and construct hierarchical segmentation by applying different threshold values to the OWT-based ultrametric contour map [210], 3) assign a score to each region based on edge strength and sparse shape representation [211], and 4) select the best candidate regions via ILP. Denote a set of candidate regions by  $s = [s_1, \dots, s_N]^T$  and their scores by  $w = [w_1, \dots, w_N]^T$ . Define  $c_{ij}$  as  $c_{ij} = 1$  if  $s_i \cap s_j \neq \emptyset$ , otherwise  $c_{ij} = 0$ . Let  $z = [z_1, \dots, z_N]^T$  be an indicator variable corresponding to the regions:  $z_i = 1$  means  $s_i$  is selected, otherwise not. The ILP aims to select a set of nonoverlapping regions with maximizing the total score

$$F_{\text{ILP}} = \max_z w^T z, \text{ s. t. } z_i + z_j \leq 1, \text{ if } c_{ij} = 1 \quad (23)$$

where  $z_i \in \{0, 1\}$ . The candidate regions are a set of nested segments, and the constraint in (23) guarantees at most one region will be selected for two overlapping regions. Therefore, the final segmentation will be the best nonoverlapping regions with the highest overall score. For computational efficiency, dynamic programming with a special tree structure is applied to solving (23) [209]. A similar region selection method for muscle cell segmentation is presented in [208], except that the edge map is created using a random-forest-based structure edge detection in the first step. The segmentation results using this approach are shown in Fig. 3. Another watershed-transform-based region selection via dynamic programming is also reported in [212] for cell segmentation in immunohistopathology images, which measures each region with unsupervised shape similarity and object scale information. For joint segmentation of nuclei and cytoplasm in Pap smear images [213], a set of nested partitions are generated by applying watershed to the  $h$ -minima transform of gradient magnitude images with increasing  $h$  values, and then, a two-pass search algorithm [214] is used to select the best

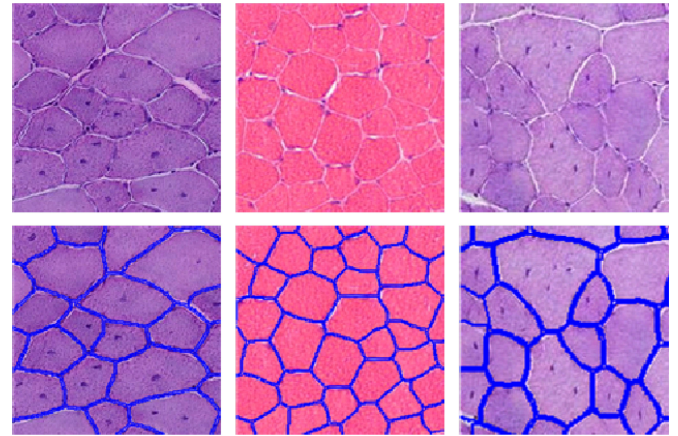


Fig. 3. Segmentation results using [208] on three sample skeletal muscle images. Original images are shown in the top row, and their corresponding segmentations are represented as blue contours in the bottom row. The images are captured at 10 $\times$  objective magnification.

candidate regions. The classification of nuclei and cytoplasm is achieved via an SVM classifier.

#### D. Deformable Models

Deformable models (or active contour/surface models) are one of the most popular nucleus or cell segmentation algorithms, since they exhibit a great tradeoff between efficiency and flexibility [215]. Starting from a certain initial position, which is manually specified by a user or automatically detected by another algorithm (see Section II), an active contour evolves toward the object boundary by minimizing an energy functional, and the model achieves segmentation when the evolving contour matches the object boundary. Originally, the energy of the active contour model (called snake) is formulated as a linear combination of three terms [216].

$$EG(v) = E_{\text{int}}(v) + E_{\text{image}}(v) + E_{\text{con}}(v) \quad (24)$$

where  $v$  is the representation of a snake.  $E_{\text{int}}$ ,  $E_{\text{image}}$ , and  $E_{\text{con}}$  correspond to the internal energy constraining the snake to be smooth, the image energy encouraging the snake to move toward features of interest, and the constraint energy allowing interaction between the user and the snake, respectively. Although graph cut-based active contour models [188], [217] are presented, the two major implementations of deformable models for nucleus or cell segmentation are geodesic and parametric snakes, which are with implicit and explicit contour representations, respectively. The choice of the representation and the energy terms usually depend on the practical applications [215].

**1) Geodesic Models:** In a geodesic model (or level set model), a contour is implicitly represented as the zero level set of a high-dimensional manifold [215], [218]. The edge-based level set models usually rely on the image gradient to terminate contour evolution [219]–[222], and thus, they might be effective on only objects with boundaries defined by gradients. On the other hand, recently the region-based energies [223], [224], which are based on the Mumford–Shah functional [225],



can detect nongradient defined contours. Compared with edge-based models, region-based models are more robust to noise and weak edges. A well-known Chan–Vese level set model used for nucleus or cell segmentation is formulated as follows [223]:

$$\begin{aligned}
 EG(c_0, c_b, \phi) = & \lambda_0 \int_{\Omega} |I(x, y) - c_0|^2 H(\phi(x, y)) dx dy \\
 & + \lambda_b \int_{\Omega} |I(x, y) - c_b|^2 (1 - H(\phi(x, y))) dx dy \\
 & + \mu \int_{\Omega} \delta(\phi(x, y)) |\nabla \phi(x, y)| dx dy \\
 & + \nu \int_{\Omega} H(\phi(x, y)) dx dy
 \end{aligned} \quad (25)$$

where  $I(x, y)$  represents a 2-D image.  $c_0$  and  $c_b$  are the average intensities of  $I(x, y)$  inside and outside the curve  $\phi(x, y)$ , respectively.  $H(\cdot)$  and  $\delta(\cdot)$  denote the Heaviside function and the Dirac function, respectively. All the parameters  $\lambda_0, \lambda_b, \nu$ , and  $\mu$  are constants, controlling the corresponding terms in the energy functional. The associated Euler–Lagrange equation can be derived from (25) and solved with the gradient descent method.

In order to simultaneously segment hundreds or even thousands of nuclei or cells in microscopy images, usually multiple level set energy functions are initialized, one per nucleus or cell. However, nuclei or cells often touch with each other, and thus, evolving each contour independently will lead to undesired segmentation results: adjacent evolving contours will cross each other, and finally, merge into a single one. Therefore, a repulsive term is introduced into the Chan–Vese formula to model the interaction among contours for *Drosophila* cell segmentation in RNAi fluorescent cellular images [29] and breast cancer nuclei segmentation in hematoxylin-stained TMA images [80].

$$\begin{aligned}
 EG = & \lambda_0 \sum_{i=1}^N \int_{\Omega} |I(x, y) - c_i|^2 H(\phi_i(x, y)) dx dy \\
 & + \lambda_b \int_{\Omega} |I(x, y) - c_b|^2 \prod_{i=1}^N (1 - H(\phi_i(x, y))) dx dy \\
 & + \omega \sum_{i=1}^N \sum_{j=1, j \neq i}^N \int_{\Omega} H(\phi_i(x, y)) H(\phi_j(x, y)) dx dy \\
 & + \mu \int_{\Omega} g(I) \delta(\phi_i(x, y)) |\nabla \phi_i(x, y)| dx dy
 \end{aligned} \quad (26)$$

where contour  $\phi_i(x, y)$  corresponds to the  $i$ th object, and  $g(\cdot)$  is a sigmoid function. The third term in (26) represents the repulsion to prevent adjacent contours from merging so that touching nuclei or cells can be correctly segmented. The last term can additionally help separate cells from the background.

There exist many other geodesic deformable models for nucleus or cell segmentation. Dufour *et al.* [226] have extended the active contour [223] to 3-D active surface models, which have been applied to fluorescent cell segmentation, and later improved the framework by using 3-D active meshes to reformulate the problem in the discrete domain such that the computational complexity can be significantly reduced [227]. In

addition, Dzyubachyk *et al.* [189] have presented an advanced level set-based cell segmentation and tracking framework by introducing a number of improvements on the coupled-active-surfaces framework [226] including an efficient stopping criterion, energy minimization without partial differential equations, and weighted DT for active surface reinitialization. Li *et al.* [228] have combined a region energy [229] and an edge energy [222] into a level set model to segment and track cells in phase-contrast microscopy images. Based on the Chan–Vese model [223], Zhang *et al.* [230] have proposed a coupled geodesic active contour model for cell segmentation and tracking in fluorescence microscopy images, which minimizes the overlaps between contours (corresponding to touching or overlapping cells) to prevent them from merging. This model is also applied to red blood cell segmentation in [114], where graph coloring is introduced to improve computational efficiency.

In order to improve the robustness of weak edge tolerance, Padfield *et al.* [231] have added a size constraint to the geodesic model [222] to extract G2 phase nuclei of 3-D eukaryotic cells in confocal microscopy images, and Xiong *et al.* [190] have introduced a new force from coarse segmentation, which is generated by FCM clustering [232], into the geodesic model [222] for *Drosophila* RNAi fluorescent cell segmentation. For freezing cell segmentation, Wu *et al.* [191] have presented a local level set model with a competitive constraint to handle touching HeLa cells, which can tackle the heterogeneous intensity. Nath *et al.* [233] have proposed a fast coupled level set method based on the four color theorem to segment cells in phase-contrast microscopy images, and another efficient level set method is reported in [192] for fluorescent cell segmentation, which formulates the energy functionals into a convex problem such that a global solution can be achieved. In order to reduce the sensitivity to initialization of the level set model [234], EM is used to automatically segment the regions of interest in breast cancer histopathology images [193]. Furthermore, an edge-path algorithm is exploited to split overlapping cells. Similarly, Chang *et al.* [194] have first adopted a level set model with color and scale information constraints to segment the foreground, and then, applied Delaunay triangulation and geometric reasoning to nuclei clump splitting.

Level set models with shape priors have been widely used to handle object partial occlusion [235], [236]. In [195], a statistical shape model is incorporated into the level set framework [236] to segment overlapping nuclei and lymphocytes in prostate and breast cancer histopathological images; in [74], the shape prior constraint [235] is integrated in the distance regularized level set model [237], and thus, the method can efficiently handle severely overlapping cervical cells. Some other level set methods with object shape constraints have also reported for nucleus segmentation in FNA prepared smear images [238], joint segmentation of nuclei and membranes in fluorescent cell images [239], mitotic nucleus segmentation in *Drosophila* embryos fluorescence images [240], and cell segmentation in 3-D zebrafish spinal cell images [241]. However, these shape models might introduce extra parameters for optimization. In addition, supervised shape prior modeling usually needs a sufficient number of training data, which might require labor-intensive annotation.



**2) Parametric Models:** In a parametric active contour model, a contour is explicitly represented with a continuous parameter:  $v(s) = (x(s), y(s))$ ,  $s \in [0, 1]$ . By searching for a balance between the internal and external force, the traditional snake model [216] moves contours toward desired image edges while keeping them smooth. In order to increase the capture range of the external force, Cohen has introduced a pressure force to form a balloon snake [242]. On the other hand, Xu and Prince [243] have replaced the traditional external force with a GVF to handle the problems of sensitive initialization and poor convergence to boundary concavities. Let  $M(x, y)$  be the edge map, the GVF field  $f(x, y) = [o(x, y), q(x, y)]$  is defined by minimizing the energy functional

$$EG = \int \int \mu(o_x^2 + o_y^2 + q_x^2 + q_y^2) + |\nabla M|^2 |f - \nabla M|^2 dx dy. \quad (27)$$

Compared with geodesic models, the corresponding parametric models usually have relatively lower computational cost and can be solved faster [244]. In addition, it is more suitable to resort to parametric models when the object topology is known. This occurs frequently in cell segmentation in fluorescence microscopy images, in which nuclei are first detected, and then, used as initialization of cell segmentation. Although topology preserving level set model [245] is proposed, generally it might be more efficient to use parametric models for this case.

Based on the GVF snake [243], Zimmer *et al.* [246] have introduced a new edge map, which is calculated for each snake, to handle weak object boundaries, and successfully applied it to cell segmentation and tracking in phase-contrast microscopy images. Meanwhile, the introduced repulsive mechanism, which can prevent adjacent contours from merging into each other, does not suffer from the increased complexity of multiple objects. Later, Zimmer and Olivo-Marin [244] have proposed a region-based parametric active contour model with a repulsion constraint for cell segmentation and tracking in fluorescence microscopy images. Compared with the traditional snake [216] or GVF snake [243], it is more robust to image noise, and able to handle touching cells as well. Given an image  $I$  with  $N$  cells, let  $c_i$  and  $c_b$  represent the average intensity inside contour  $v_i$  and outside all the contours, respectively, the coupled parametric active contour is formulated as

$$\begin{aligned} EG = & \frac{1}{2} \sum_{i=1}^N \int_0^1 \left[ \alpha \left( \frac{\partial v_i}{\partial s} \right) + \beta \left( \frac{\partial^2 v_i}{\partial s^2} \right) \right] ds \\ & + \lambda_0 \sum_{i=1}^N \int_{\text{inside}(v_i)} (I - c_i)^2 d\sigma \\ & + \lambda_b \int_{\text{outside}(v_1 \cup \dots \cup v_N)} (I - c_b)^2 d\sigma \\ & + \omega \sum_{i=1}^N \sum_{j=1, j \neq i}^N \int_{\text{inside}(v_i) \cap \text{inside}(v_j)} 1 d\sigma \end{aligned} \quad (28)$$

where  $s$  denotes the parameter for explicit contour representation and  $d\sigma$  is the elementary surface. Similar models have

been applied to cell segmentation in phase-contrast microscopy images [247] and pancreatic NET nuclei segmentation in bright-field microscopy images [248], [249].

The traditional GVF snake [243] is applied to schizosaccharomyces pombe cell segmentation in bright-field microscopy images [173], where focus gradient correction and image enhancement are performed in advance to generate better edge maps. In [196], [250], and [251], the GVF snake is applied to the LUV color space for simultaneous segmentation of nuclei and cytoplasm in blood smear images; in [252], a repulsive force is incorporated to the GVF snake to separate adjacent neuronal axons, which is achieved by reversing the gradient direction of neighboring objects. Recently, Xing *et al.* [82], [121] have introduced a contour-based repulsive term into the balloon snake model [242] for nucleus segmentation in pancreatic NET images. The internal  $F_{\text{int}}$  and external  $F_{\text{ext}}$  forces of the repulsive balloon snake model are represented as

$$F_{\text{int}}(v_i) = \alpha v_i''(s) - \beta v_i'''(s) \quad (29)$$

$$\begin{aligned} F_{\text{ext}}(v_i) = & \gamma n_i(s) - \lambda \frac{\nabla E_{\text{ext}}(v_i(s))}{\|E_{\text{ext}}(v_i(s))\|} \\ & + \omega \sum_{j=1, j \neq i}^N \int_0^1 d_{ij}^{-2}(s, t) n_i(t) dt \end{aligned} \quad (30)$$

where the two terms in (29) are the second and fourth derivative of  $v_i(s)$  with corresponding weights  $\alpha$  and  $\beta$ , respectively. The  $n_i(s)$  together with weight  $\gamma$  in (30) represents the pressure force, and  $\nabla E_{\text{ext}}(v_i(s))$  denotes the image force where  $E_{\text{ext}}(v_i(s)) = -\|\nabla I(x(s), y(s))\|^2$ . The last term in (30) represents the repulsive force, where  $N$  is the number of cells,  $d_{ij}(s, t) = \|v_i(s) - v_j(t)\|_2$  denotes the Euclidean distance between contour  $v_i(s)$  and  $v_j(t)$ . The parameter  $\omega$  controls the weight for the repulsive force. The last term can prevent evolving contours from crossing and merging with one another such that touching nuclei can be correctly separated if given proper initialization.

Parametric deformable models combined with shape priors are also presented in recent literature. Cai *et al.* [253] have introduced a single shape prior into the GVF model for better neuron boundary delineation in 3-D microscopy images. In [254], Xing and Yang have presented a sparsity-based shape dictionary to constrain an RBSM in lung cancer nuclei segmentation. Specifically, starting from initial contours, it alternately performs shape deformation with the RBSM and shape inference with the shape dictionary. It can segment touching nuclei with preserving smooth contours. Similarly, sparse shape prior modeling is also combined with a deformable model introduced in [125] for nucleus segmentation in multiple pathology image datasets, and the segmentation result for one sample image is shown in Fig. 4. Another learning-based method with shape prior modeling is presented in [40] for Pap smear nuclei segmentation, which combines the physical deformable model [255] and the active shape model (ASM) [256]. This approach can effectively segment partially occluded nuclei in pair, and produce better segmentation accuracy than the standard ASM model.

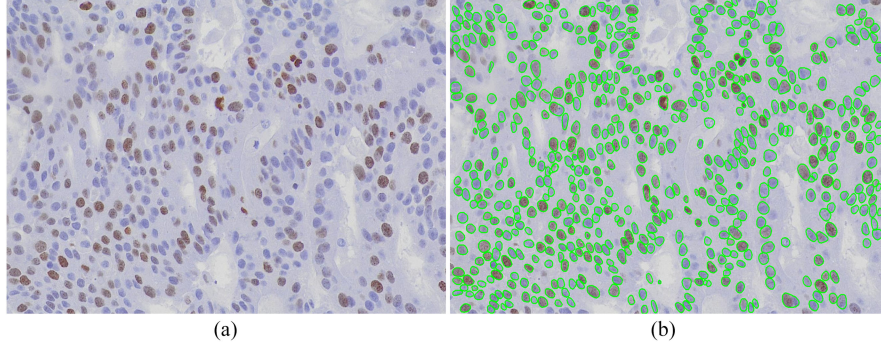


Fig. 4. Segmentation results using [125] on one sample pancreatic NET image. Green contours represent results of boundary segmentation. (a) Original image. (b) Segmentation results.

### E. Clustering

Clustering is to group a collection of objects into subsets or clusters, such that those within each cluster are closely related to one another than objects assigned to different clusters [257]. One fundamental and important aspect of cluster analysis is the selection of similarity or dissimilarity among objects, which can be measured with various metrics, such as Euclidean distance, correlation, 0-1 error, etc. For image segmentation, clustering usually realizes each object as one pixel and partitions all pixels into multiple disjoint regions. In nucleus or cell segmentation, cluster analysis might not output the final segmentation, but provide supports for subsequent object boundary extraction. In this subsection, we discuss those nucleus or cell segmentation approaches based on three popular clustering algorithms: K-means, FCM, and EM. Although clustering models are mainly used for object segmentation in pathology or microscopy image analysis, the cluster centers can be used to locate the nuclei or cells [80], [122], [258].

**1) K-means:** K-means clustering [130], [259] is an iterative descent clustering algorithm, which aims to partition the dataset  $\{\mathbf{x}_i\}_{i=1}^N$  into  $K$  groups. By introducing a set of prototypes  $\{\boldsymbol{\mu}_k\}_{k=1}^K$ , which are actually cluster centers, associated with  $K$  clusters, it tends to assign each data point to the nearest prototype. Formally, the K-means clustering algorithm is formulated as minimizing the distortion measure

$$\arg \min_{r_{ik}, \boldsymbol{\mu}_k} \sum_{i=1}^N \sum_{k=1}^K r_{ik} \|\mathbf{x}_i - \boldsymbol{\mu}_k\|^2 \quad (31)$$

where  $r_{ik} \in \{0, 1\}$  is a binary indicator variables:  $r_{ik} = 1$  if  $\mathbf{x}_i$  is assigned to cluster  $k$ , otherwise 0. The model (31) can be solved by alternately calculating the means based on the current assignment and determining the assignment by associating data points to their nearest means. K-means is sensitive to initialization, and one straightforward strategy for tackling this problem is to run the algorithm multiple times and select the one with the smallest distortion.

Kothari *et al.* [260] have applied K-means clustering to coarse segmentation, and then, conducted refinement for nucleus segmentation in H&E- and IHC-stained pathology images. Specifically, it mainly contains three steps: 1) separate nucleus regions

from the background using K-means clustering followed by morphological reconstruction [51] and simple edge detection, 2) split touching nuclei based on concave point detection [261], and 3) extract nucleus boundaries using direct least-square-based ellipse fitting [64]. In order to deal with different stained pathology images, it allows user interaction to select initial points for K-means clustering. An alternative and automated method to handle stain variations is to perform stain normalization [183], [262] before image analysis. Arif and Rajpoot [263] have formulated nuclei segmentation as manifold learning-based shape classification on prostate histology images, which consists of three major steps: 1) segment nuclei or nucleus clumps with K-means clustering, 2) extract the candidate boundaries with Fourier transform representation, and 3) apply out-of-sample extension to a learned shape manifold embedding for nucleus classification.

**2) FCM:** Unlike hard clustering that assigns each object to exactly one cluster, soft clustering allows one object to associate with more than one cluster and uses membership degree to measure the strength of the association [264]. In this scenario, it can produce better data representation for the objects that cannot be fully assigned to one cluster. One of the most popular soft clustering algorithm is FCM [232]. FCM aims to partition the dataset into  $C$  fuzzy clusters, and its objective function is very similar to (31), but replaces the indicator variable with a continuous variable  $w_{ik}^m$ , which represents the membership degree, and calculates the cluster centers as a weighted average as follows:

$$J_m = \sum_{i=1}^N \sum_{c=1}^C w_{ic}^m \|\mathbf{x}_i - \boldsymbol{\mu}_c\|^2 \quad (32)$$

$$w_{ic}^m = \frac{1}{\sum_{j=1}^C \left( \frac{\|\mathbf{x}_i - \boldsymbol{\mu}_c\|}{\|\mathbf{x}_i - \boldsymbol{\mu}_j\|} \right)^{\frac{2}{m-1}}}, \quad \boldsymbol{\mu}_c = \frac{\sum_{i=1}^N w_{ic}^m \mathbf{x}_i}{\sum_{i=1}^N w_{ic}^m} \quad (33)$$

where  $m \in [1, +\infty)$  is a real value controlling the fuzzy level. Similar to the K-means optimization, minimizing (32) is to alternately compute the membership degree and the weighted cluster means using (33).

Zhou *et al.* [57] have proposed an FCM-based cell segmentation in RNAi images. Since nuclei are brighter than image background in the DNA channel, it is easy to first segment nuclei, and then, use the segmented nuclei to guide subsequent cell segmentation. Specifically, the approach consists of four key steps: 1) segment nucleus regions based on top-hat and bottom-hat transforms and split touching nuclei with Hue transform, 2) estimate a rough cell boundary with a polygon for each cell with a nonoverlapping region constraint, 3) binarize each cell region with a two-stage FCM clustering, and 4) separate touching cells using marker-controlled watershed with DT. In the two-stage FCM clustering, it first uses an FCM to partition image pixels into three clusters, and then, exploits a second FCM clustering to sharpen the regions of interest to obtain the cytoplasm regions, which automatically select a membership degree threshold for binarization. In [265], a parallel FCM-based nucleus segmentation approach is introduced to adapt to large-scale histological images. It uses message passing interface to build the parallel programming platform, which is applicable to high resolution image analysis of WSI.

**3) EM:** EM algorithm [273], which is originally designed for maximum likelihood estimation, can be used to conduct cluster analysis with soft assignment. Based on a probabilistic modeling, it provides not only the cluster means but also the covariance. EM for Gaussian mixtures is one of the most widely used method for image segmentation. Suppose a  $D$ -dimensional dataset  $\mathbf{X} = [\mathbf{x}_1 \mathbf{x}_2 \dots \mathbf{x}_N]^T \in \mathbb{R}^{N \times D}$  is modeled with a mixture of Gaussians:  $\mathcal{N}(\mathbf{x}_i | \boldsymbol{\mu}_k, \boldsymbol{\Sigma}_k)$ , where  $i = 1, \dots, N$  and  $k = 1, \dots, K$ , and the corresponding latent variables are represented by  $\mathbf{Z} = [\mathbf{z}_1 \mathbf{z}_2 \dots \mathbf{z}_N]^T \in \mathbb{R}^{N \times K}$ , which indicate the component from which the data are generated, then the log of the likelihood function is given as

$$\ln p(\mathbf{X} | \boldsymbol{\pi}, \boldsymbol{\mu}, \boldsymbol{\Sigma}) = \sum_{i=1}^N \ln \left\{ \sum_{k=1}^K \pi_k \mathcal{N}(\mathbf{x}_i | \boldsymbol{\mu}_k, \boldsymbol{\Sigma}_k) \right\} \quad (34)$$

where  $\{\pi_k\}_{k=1}^K$  denote the mixing coefficients with the constraint  $\sum_{k=1}^K \pi_k = 1$ . Given initial  $\{\pi_k, \boldsymbol{\mu}_k, \boldsymbol{\Sigma}_k\}_{k=1}^K$ , the EM algorithm maximizes the log-likelihood (34) by iteratively alternating computing the responsibilities  $\gamma(z_{ik})$  in (35) (E-step) and estimating the parameters in (36) and (37) (M-step) until convergence as follows [130]:

$$\gamma(z_{ik}) = \frac{\pi_k \mathcal{N}(\mathbf{x}_i | \boldsymbol{\mu}_k, \boldsymbol{\Sigma}_k)}{\sum_{j=1}^K \pi_k \mathcal{N}(\mathbf{x}_i | \boldsymbol{\mu}_j, \boldsymbol{\Sigma}_j)} \quad (35)$$

$$\pi_k = \frac{N_k}{N}, \quad \boldsymbol{\mu}_k = \frac{1}{N_k} \sum_{i=1}^N \gamma(z_{ik}) \mathbf{x}_i \quad (36)$$

$$\boldsymbol{\Sigma}_k = \frac{1}{N_k} \sum_{i=1}^N \gamma(z_{ik}) (\mathbf{x}_i - \boldsymbol{\mu}_k)(\mathbf{x}_i - \boldsymbol{\mu}_k)^T \quad (37)$$

where  $N_k = \sum_{i=1}^N \gamma(z_{ik})$  represents the effective number of data points assigned to cluster  $k$ . Due to slow convergence, usually the EM algorithm is initialized with K-means clustering. After convergence, each image pixel is assigned  $K$  (posterior)

probability values of associating with the  $K$  clusters. In addition, it provides both the means and covariances of the clusters, while K-means estimates only the cluster means.

Jung *et al.* [266] have presented an EM-based automated nucleus segmentation approach in mammary invasive ductal carcinomas and cervical images. It uses a mixture of Gaussians to model the topographic surfaces in the DT maps, and each Gaussian component corresponds to one nucleus. It incorporates the EM algorithm into a cluster validation framework based on the separation and the compactness of nuclei [274], which can automatically select the optimal number of nuclei. In order to maximize the separability of overlapping nuclei, the data points are projected onto the direction estimated by using LDA, and their memberships are determined based on the Bayesian rule. After nuclei splitting, it further applies the direct least-square ellipse-fitting method [64] to the contours for recovering occluded nuclei. However, it exhibits high computational complexity due to the parametric EM-based cluster analysis.

Another EM-based nucleus segmentation method is reported in [193], which focuses on lymphocyte nuclei in breast cancer histopathological images. It uses the RGB values to create a GMM, and partitions the image into four types of regions corresponding to the structures of breast cancer nuclei, lymphocyte nuclei, stroma, and background, respectively. The final membership of each pixel is determined as the one corresponding to the maximum posterior probability. The whole procedure of lymphocyte nucleus segmentation can be summarized as: 1) segment the image into the four categories of regions using the EM algorithm, 2) extract component boundaries using the magnetostatic active contour model [234] with EM-generated segmentation as initialization, 3) split touching nuclei with a concave point detection-based shortest path searching algorithm, and 4) discriminate lymphocytes from the others by using K-means clustering with the first-order statistical texture features calculated from the segmented nuclei. Due to lack of nucleus shape prior modeling, this approach would not guarantee accurate boundary delineation.

## F. Graph-Based Methods

Graph-based image segmentation approaches [275], [276] model one image as a weighted graph, in which each node associates a pixel or superpixel in the image and each edge weight between two nodes corresponds to the similarity between neighboring pixels or superpixels. According to a certain criterion, the graph is partitioned into multiple sets, each representing an object segment in the image.

**1) Max-Flow/Min-Cut:** Max-flow/min-cut algorithms [160],

[277] have been widely applied to image segmentation in computer visions and medical image analysis. Typically, A graph-cut algorithm is used to minimize an energy function, which aims to solve a pixel-labeling problem. The energy can be generally formulated as

$$EG(L) = \sum_{v \in \mathcal{V}} D_v(L_v) + \sum_{(v,u) \in \mathcal{N}} S_{v,u}(L_v, L_u) \quad (38)$$



where  $L = \{L_v \in \mathcal{L} | v \in \mathcal{V}\}$  is a labeling of image  $\mathcal{V}$ ,  $D_v(\cdot)$  represents the penalty function that measures the cost of label  $L_v$  assigned to pixel  $v$ ,  $S_{v,u}(\cdot)$  denotes an interaction potential that controls the spatial smoothness, and  $\mathcal{N} \subset \mathcal{V} \times \mathcal{V}$  is the set of all pairs of neighboring pixels. The goal is to search for a mapping from  $\mathcal{V}$  to  $\mathcal{L}$ . The definition for the data term  $D_v(\cdot)$  and the smoothness term  $S_{v,u}(\cdot)$  depends on specific applications.

Al-Kofahi *et al.* [68] have presented a two-stage graph cut-based method to segment nuclei in histopathology images. First, a fast max-flow/min-cut algorithm [160] is applied to foreground (nucleus regions) segmentation, which chooses the data and smoothness terms as follows:

$$D_v(L_v) = -\ln p(V_v | z = \{0, 1\}) \quad (39)$$

$$S_{v,u}(L_v, L_u) = \eta(L_v, L_u) \times e^{-\frac{|V_v - V_u|}{2\sigma^2}} \quad (40)$$

where  $p(v|z)$ ,  $z = 0, 1$  are Poisson distributions.  $\eta(L_v, L_u) = 1$  if  $L_v \neq L_u$ , otherwise 0.  $\sigma$  is a fixed parameter. After foreground segmentation, nuclei are initially segmented with LoG detection followed by size-constrained clustering [88]. Finally, graph cut with  $\alpha$ -expansion [277] and graph coloring [233] are used to refine the initial segmented contours. The cost for assigning pixel  $v$  to color  $j$  is calculated as

$$D_v(L_v = j) = -\ln \max\{G(v; \mu_i, \Sigma_i) | C_i = j\} \quad (41)$$

$$S_{v,u}(L_v, L_u) = \eta(L_v, L_u) \times e^{-|V_v - V_u|} \quad (42)$$

where  $G(v; \mu_i, \Sigma_i)$  is a Gaussian function representing the likelihood assigning pixel  $v$  to nucleus  $i$ , and  $C_i$  is the label of nucleus  $i$ .  $\eta(L_v, L_u) = c$  ( $c$  is a constant) if  $L_v \neq L_u$ , otherwise 0. This algorithm is also applied to cell segmentation in colon fluorescence images [278], where it further eliminates small candidates or merges adjacent regions to constrain subsequent cell phenotype analysis on only distinguishable nuclei.

Lou *et al.* [279] have incorporated a blob-like shape prior into the graph cut framework [277], where the weights in the energy function are optimized via structured learning, for dense nucleus segmentation in fluorescence microscopy images. Denote  $G = (V, E)$  the graph associated with an MRF, the segmentation is formulated as a labeling problem that minimizing the following energy function:

$$\begin{aligned} EG(\mathbf{x}, \mathbf{l}; \mathbf{w}) = & w_d \sum_{v \in V} E_d(l_v) + w_s \sum_{\langle v, u \rangle \in E} E_s(l_v, l_u) \\ & + w_f \sum_{v \in V} E_f(l_v) + w_p \sum_{\langle v, u \rangle \in E} E_p(l_v, l_u) \end{aligned} \quad (43)$$

where  $\mathbf{l} \in \{0, 1\}^{|V|}$  is the labeling for the image  $\mathbf{x}$ .  $E_d(\cdot)$  and  $E_s(\cdot)$  correspond to local appearance and smoothness constraint, respectively.  $E_f(\cdot)$  counteracts the shrinking bias [280], and  $E_p(\cdot)$  encodes the shape prior. These four energy terms are weighted by their corresponding parameters  $\mathbf{w} = \{w_d, w_s, w_f, w_p\}$ . This problem is solved by the max-flow/min-cut algorithm [160]. With the shape prior, this approach is able to well handle regularly shaped nuclei. In addition, it can be scaled up using dual decomposition and parallelization techniques.

Chang *et al.* [69] have exploited the max-flow/min-cut algorithm [160] to separate GBM nuclei regions from the H&E-stained histopathological image background, and then, split touching or overlapping nuclei using Delaunay triangulation and geometric reasoning. Different from [68], the data term in [69] is a combination of the intrinsic local probability map and the learned global property map, and the smoothness term is represented by  $n$ -links [281], which encourages continuous local geometric or minimal surface. In order to reduce the computational cost and memory requirement, the graph is constructed based on superpixels instead of pixels to simultaneously segment out nuclei, cytoplasm, and background regions in cervical cancer images [126]. However, similar to [69], it requires further processing to split the nuclei clumps.

**2) Normalized Cut:** An early attempt to use minimum cut in image segmentation is presented in [275]. With a globally minimum cut criterion, it recursively seeks the minimum cut that partitions the graph into two disjoint segments. However, this minimum cut criterion favors partitioning out small sets of nodes, which are undesired segments in real applications. In [282], a new cut cost named normalized cut is presented to avoid the unnatural bias. Let  $G = (V, E)$  denote the graph with  $V$  and  $E$  representing the sets of nodes and edges, respectively, and  $A, B$  be two disjoint sets of  $V$ , the normalized cut is defined as

$$\text{Ncut}(A, B) = \frac{\sum_{u \in A, v \in B} w(u, v)}{\sum_{u \in A, t \in V} w(u, t)} + \frac{\sum_{u \in A, v \in B} w(u, v)}{\sum_{v \in B, t \in V} w(v, t)} \quad (44)$$

where  $w(u, v)$  is the edge weight between nodes  $u$  and  $v$ . With this cut cost, partitioning out small isolated sets will exhibit large high cut values, which are penalized in the optimization, such that the bias will be eliminated. The normalized cut problem can be approximately solved using generalized eigenvalue system techniques.

Bernardis and Yu [267], [283] have applied a generalized normalized cut criterion [284] to cell segmentation in bright-field and fluorescence microscopy images. It formulates image segmentation as a constrained graph partitioning problem over a set of overlapping image patches, which are represented by weighted graphs, one per patch. By introducing grouping cues of attraction, which measures feature similarity, and repulsion, which encodes feature dissimilarity, it obtains cell segmentation via a two-way node partitioning. One potential limitation of this approach is that it requires multiple neighboring size selection for image feature extraction. Another spectral graph theory-based segmentation method is reported in [268] for separating overlapping red blood cells, which uses both spatial and color information to generate feature vectors for graph partitioning.

**3) CRF:** CRF [285] is a variant of MRF, which is a set of random variables represented by a graph. CRF is a discriminative graphical model, which usually formulates image segmentation as a labeling or classification problem, and infers the membership of each image pixel (or superpixel) based on the observations. Denote  $X$  and  $Y$  random variables corresponding to the pixels (observations) and the labels, respectively. Let  $G = (V, E)$  be a graph with nodes  $V$  and edges



$E$ , and  $V$  indexes  $Y$ . Then,  $(X, Y)$  is a CRF when conditioned on  $X$ , the variables  $Y$  obeys the Markov property [285]. The CRF globally conditioned on  $X$  can be represented as [286]

$$p(y|\mathbf{x}) \propto \exp \left( \sum_{v \in V} E_v(y_v, X) + \sum_{e_{ij} \in E} E_{ij}(y_i, y_j, X) \right) \quad (45)$$

where  $-E_v(\cdot)$  and  $-E_{ij}(\cdot)$  represent the unary and pair-wise potentials, respectively, and their selection depends on specific applications (associated with parameters needed to be estimated). With parameter estimation in the potentials, the final label  $y$  of an unseen observation  $\mathbf{x}$  is determined by computing the MAP.

Wu *et al.* [269] have adopted a CRF model to segment nuclei in multispectral cytology images. Considering the label state in neighboring spectra, it incorporates the energy function with an additional spectral constraint. To split clustered nuclei, watershed transform is applied to the DT images, which are generated from previous foreground segmentation. In [287], a heterogeneous CRF model is presented to jointly detect and segment C2C12 muscle cells and bovine aortic endothelial cells in phase-contrast microscopy images. Different from the traditional CRF, it constrains each node to be associated with a specifically defined state set to design a graphical model with sufficient expressive power and avoid unidentifiability and excessive complexity. Uzunbas *et al.* [288] have presented a superpixel-based CRF model for neuron segmentation in electron microscopy images, which could be extended to cell segmentation applications. To improve the accuracy, it also provides a flexible interactive segmentation framework.

**4) Random Walk:** Random walk is a graph-based  $K$ -way image segmentation approach given a small number of user-defined labels [289], in which one graph edge weight represents the likelihood that a random walker will cross that edge. Specifically, the algorithm can be summarized in four steps: 1) construct the graph and calculate the edge weight with an intensity similarity-based weighting function, 2) obtain seeded nodes with  $K$  labels, 3) compute the probability of each label in every node by solving a combinatorial Dirichlet problem, and 4) assign each node the label associated with the largest probability to obtain image segmentation. The random walk algorithm is applied to joint segmentation of nuclei and cytoplasm of Pap smear cells in [290], which consists of three major stages: 1) extract object edges with Sobel operator, 2) enhance the edges with a maximum gray-level gradient difference method, and 3) refine edges with random walk, which can separate overlapping objects. A fast random walker algorithm is presented in [291] for interactive blood smear cell segmentation, which improves the running time using offline precomputing. However, these random walk algorithms rely on interactive seeding for good segmentation. An automatically seed generation method for random walker is presented in [292], which could be extended to nucleus or cell segmentation in digital pathology or microscopy images.

**5) Others:** Yang *et al.* [293] have formulated touching blood cell segmentation as optimal path searching in a convex

vertex graph. For an image, the segmentation procedure begins with extracting cell boundaries using color GVF snake [196], then constructing a graph with nodes and edges corresponding to concave points and inner edges inside cells, respectively, and finally recursively searching for optimal shortest paths in the graph to separate touching cells. Wu *et al.* [294] have segmented interacting fibroblast cells in phase-contrast microscopy images by seeking the shortest path in a graph. With two endpoints of a gap, the graph is constructed by using the pixels between these two endpoints as nodes and the image gradient as the edge weight. It searches for the shortest path using dynamic programming. Another shortest path searching-based cell segmentation is presented in [295] and [296]. Given an image  $I$ , it defines a Riemannian metric as

$$\mathbf{G} = \frac{\nabla g(I) \nabla g^T(I) + \lambda \mathbf{I}_2}{1 + \lambda} \quad (46)$$

where  $g(\cdot)$  is a blurring filter,  $\mathbf{I}_2$  represents the  $2 \times 2$  identity matrix, and  $\lambda$  is a regularization parameter. Given manually located seeds (nuclei) in *Drosophila* cell fluorescence images, the cell cytoplasmic regions are segmented by using the Dijkstra's algorithm [297] to assign each pixel to its nearest seed within the manifold defined by (46) [295]. This algorithm is also applied to cell segmentation in a cell tracking framework [298], which uses the nuclei as seeds for pixel membership assignment.

Zhang *et al.* [299] have used correlation clustering [300] to achieve joint detection and segmentation of yeast cells in bright-field microscopy images and cervical cancer cells in phase-contrast microscopy images. Given a testing image, it first uses a random forest [104] to generate a cell boundary probability map, to which watershed transform is applied for superpixel computation. Next, it builds a weighted superpixel adjacency graph, in which each edge  $e$  is assigned a real-valued potential  $\theta_e$ . Positive potentials favor merging superpixels, while negative ones force them to be separated. Finally, the graph partition is achieved by solving

$$\min_{X_e \in C} \theta_e X_e \quad (47)$$

$$\theta_e = \log \left( \frac{1 - F(p_e + t)}{F(p_e + t)} \right) \quad (48)$$

where  $X_e$  is a binary indicator for edge  $e$ :  $X_e = 1$  if edge  $e$  is to be cut, otherwise  $X_e = 0$ .  $\theta_e$  represents  $e$ 's potential,  $p_e$  is the edge probability from the random forest, and  $F(x) = \max(\min(x, 0.9999), 0.0001)$ .

Arsalan *et al.* [270] have presented an attributed relational graph-based algorithm for nucleus segmentation in fluorescence microscopy images. It mainly consists of four steps: 1) calculate the nucleus boundary primitives, which correspond to different orientations, from the gradient magnitude image, 2) build an attributed relational graph based on the primitives to represent their spatial relations, 3) identify nuclei by searching for predefined structural patterns in the graph, and 4) grow the regions from the centroids of nucleus primitives to obtain nucleus boundaries. This method needs careful selection of several significant parameters, such as the primitive length threshold, percentage threshold, and standard deviation threshold from the nuclei identification. In addition, it relies on good edge

extraction, which might be challenging in complex histopathology images.

### G. Supervised Classification

Supervised classification techniques have also been used for nucleus or cell segmentation nowadays. In pixel-wise classification, the membership of each pixel in the image is determined by a learned model with a certain criterion. Usually it is unable to handle touching objects. Therefore, it requires additional efforts to achieve final segmentation. On the other hand, superpixel-wise classification first partitions the image into a set of candidate regions, and then, discriminates those regions corresponding to real nuclei or cells from the others. Compared with the pixel-wise approach, superpixel-based classification might significantly reduce the time cost. However, the performance of this approach highly depends on the generated superpixels, which might not well adhere the object boundaries.

**1) Pixel-Wise Classification:** Kong *et al.* [271] have exploited supervised learning techniques to segment nuclei in follicular lymphoma pathological images. It learns a mapping from the traditional RGB space to the MDC, in which the extracted LFT features [301] exhibit strong discriminative powers for classification, based on the Fisher-Rao discrimination criterion [302]

$$\arg \max_{\mathbf{A}, \mathbf{P}} \frac{\det(\mathbf{P}^T \hat{\mathbf{S}}_b \mathbf{P})}{\det(\mathbf{P}^T \hat{\mathbf{S}}_w \mathbf{P})} \quad (49)$$

where  $\mathbf{A}$  is a coefficient matrix for constructing MDC from the RGB space, and  $\mathbf{P}$  is the matrix to project features for more compact representation in the MDC space.  $\hat{\mathbf{S}}_b$  and  $\hat{\mathbf{S}}_w$  are feature covariance matrices of the interclass (between nuclei and extracellular regions) and intraclass (within nuclei or extracellular regions), respectively, which are dependent on  $\mathbf{A}$ . Given a testing image, it first converts the image into the MDC space, then extracts LFT features, and finally, performs pixel-wise classification with a K-NN classifier. However, the classification only separates the nucleus regions from the background such that the touching-nuclei clump does not be split. To address this problem, it iteratively separates individual nuclei from each other in the clumps based on concave point detection and radial-symmetry-based voting [107].

Another pixel-wise classification method is presented in [303] for cell segmentation on phase-contrast and DIC microscopy images, which learns a set of Bayesian classifiers from clustered local image appearance histograms and uses this mixture of classifiers to determine final pixel membership. In [304], a set of convolutional filters and a sparse linear regressor are jointly learned from GBM images, and the nucleus segmentation is achieved by performing pixel-wise binary classification, which is conducted by applying a threshold to the prediction from the regressor. However, similar to [271], these methods might need further processing to split touching cells or nuclei. Ciregan *et al.* [305] have applied a deep CNN-based method to neuronal membrane segmentation in electron microscopy images. It trains multiple networks and calculates the average of their outputs as final prediction, which is better than a single network. However,

it conducts the segmentation in a sliding window manner, which might have high time cost on large-size images.

**2) Superpixel-Wise Classification:** Janssens *et al.* [272] have applied a multiclass SVM classifier to cell segmentation on H&E-stained skeletal muscle images. It consists of three steps: 1) generate initial segments by thresholding the saturation and the brightness of the image; 2) classify these segments into three categories with a set of features consisting of geometry, texture, bottle measurement, and luminosity: individual cells, cell clumps, and remnant connective tissues; 3) split the cell clumps based on concave point detection [306]. The last two steps are recursively conducted until no cell clumps exist. In [307], nucleus segmentation is achieved by using an ADT [308] to select the best superpixels, which are generated using a set of intensity thresholds. However, these methods might not generate accurate object boundary delineation. For serous image segmentation, Cheng *et al.* [309] have used a structured SVM classifier to pick the optimal superpixels, which are created by Turbopixels [310]. Specifically, it is composed of four steps: 1) calculate a set of pixel-based features in a local region including appearance, shape, and context, 2) pool these features to form one single vector for a superpixel, 3) apply structure SVM to region selection, and 4) separate touching objects with DT and generalized Voronoi diagram [311].

## IV. DISCUSSION AND FUTURE WORK

During the last few decades, many state-of-the-art methods have been proposed for nucleus/cell detection and segmentation in digital pathology and microscopy images, but not all of them are applied to the same dataset. Instead, many of them are evaluated on their own datasets, and thus, it is difficult to determine whether one approach is better than another. In addition, since different detection and segmentation measurements are used in the literature, it is not straightforward to quantitatively compare the current methods. Therefore, common benchmarks of image data are required for comparative evaluation of various detection and segmentation approaches. Currently, there exists several public benchmarks for nucleus/cell detection and segmentation approaches: ICPR 2012 mitotic cell detection contest [312], [313]; AMIDAI13 dataset [314], [315]; UCSB Bio-Segmentation benchmark [316]; hand-segmented U2OS/3T3 cell image dataset [317]; and ISBI 2013 cell tracking challenge [318].

The mitotic cell dataset at ICPR 2012 contest [312] contains H&E-stained breast cancer histology images acquired with Aperio ScanScope XT slide scanner, Hamamatsu NanoZoomer 2.0-HT slide scanner, and ten bands multispectral microscopy. It consists of 50 high-power fields images with 326 mitotic cells from the two scanners and 322 from the multispectral microscopy. All the mitotic cells are manually annotated by one pathologist. Another mitotic cell dataset AMIDAI13 [314], [315] consists of 23 H&E-stained breast cancer histological images (12 for training and 11 for testing) from the Aperio ScanScope XT slide scanner. The ground truth of cells are annotated by multiple pathologists. These two datasets provide the locations of mitotic cells, and thus, they are suitable for cell

detection. In these contests, the precision, recall, and  $F_1$  score are suggested for algorithm evaluation.

The UCSB Bio-Segmentation benchmark [316] is composed of different types of images and associated ground truth. Four types of cellular level images are collected for cell detection and segmentation: 10 cat retinal photoreceptor images; 10 stacks of arabidopsis and cat retinal 3-D cells; 190 COSI kidney cell images; and 58 breast cancer cell images. The first three are obtained through confocal microscopy imaging, and the last one is H&E-stained histopathological images. The ground truth consists of manually annotated nuclei centroids for the first two, which can be used for evaluation of detection algorithms, and binary masks for the last two, which are created to validate segmentation methods.

The hand-segmented U2OS/3T3 cell image dataset [317] contains a set of 97 2-D fluorescence microscopy images: 48 images with U2OS cells and 49 with NIH3T3 cells. The nucleus boundaries used for comparison are manually annotated. It also suggests several segmentation metrics including Rand and Jaccard indexes, counting errors (split, merged, added, and missing), NSD, and HD. The ISBI cell tracking challenge [318] benchmark contains 48 time-lapse sequences (half for training and the other for testing), which can be used to evaluate cell segmentation or tracking algorithms. The training/testing has 12 real fluorescence microscopy videos and 12 computer-simulated videos, 6 2-D and 6 3-D, with different levels of cell densities and image noise. The ground truth for cell segmentation are manually generated by several experts.

There exist a set of public and free biomedical imaging software tools, which can be used to detect and segment nuclei or cells across different microscopy image modalities. ImageJ [319], [320] is a widely used Java-based image analysis program, which is inspired at the National Institutes of Health. It is available for multiple operating systems including Windows, Mac OS, and Linux. It provides many algorithm implementations for medical image processing including nucleus/cell detection and segmentation. CellProfiler [321] is a very popular software tool for identifying and quantifying cell phenotypes, and it has well served the community for years [322], [323]. It implements several existing algorithms for nucleus and cell segmentation as well as quantitative analysis. More information about popular biomedical imaging software tools can be found in [324]–[326].

One of major challenges for automated nucleus/cell detection and segmentation is to accurately separate touching or overlapping nuclei/cells. Due to the significant variations in image appearance of different microscopy images including bright field, phase contrast, DIC, fluorescence, and electron, many approaches have achieved great successes on some specific image modalities, but they might produce poor performance on other datasets. Nucleus/cell segmentation with shape preserving is very important for cellular morphology computation, which can be used to determine the categories of cells or biospecimens. Therefore, detection and segmentation of touching and overlapping nuclei/cells might continuously attracts research attention.

Many current algorithms are not well scalable to a large number of nuclei or cells. In digital pathology, it is usually necessary

to achieve efficient and effective cell segmentation on the whole slice images, each of which might contain millions of cells. For example, it will be more accurate to calculate the Ki-67 score based on all the cells in the whole slide image instead of several representative image patches cropped from the image. The intensity thresholding, morphological operation, and watershed can be easily implemented, but usually they are not able to effectively handle touching or overlapping cells. Although marker-controlled watershed transform is introduced to separate touching cells, sometimes it is not easy to obtain correct marker detection. Deformable models, clustering, and graph-based methods might have high computational costs when applying to whole slide images. The pixel-wise classification suffers from the limitations of the sliding window technique on large-size images, while the segmentation accuracy of superpixel-wise classifiers depends on the boundary adherence of generated superpixels. Therefore, designing a robust nuclei/cell detection and segmentation algorithm that can adapt to whole slide images (gigabytes with millions of cells) might remain to be an open challenge in digital pathology and microscopy image analysis. One potential solution might be using parallel or distributed computing techniques to improve the running time cost.

## REFERENCES

- [1] M. G. Rojo, V. Punys, J. Słodkowska, T. Schrader, C. Daniel, and B. Blobel, "Digital pathology in Europe: Coordinating patient care and research efforts," *Stud. Health Technol. Inform.*, vol. 150, pp. 997–1001, 2009.
- [2] M. G. Rojo, "State of the art and trends for digital pathology," *Stud. Health Technol. Inform.*, vol. 179, pp. 15–28, 2012.
- [3] M. May, "A better lens on disease: Computerized pathology slides may help doctors make faster and more accurate diagnoses," *Sci. Amer.*, vol. 302, pp. 74–77, 2010.
- [4] A. Katouzian, E. D. Angelini, S. G. Carlier, J. S. Suri, N. Navab, and A. F. Laine, "A state-of-the-art review on segmentation algorithms in intravascular ultrasound (IVUS) images," *IEEE Trans. Inf. Technol. Biomed.*, vol. 16, no. 5, pp. 823–834, Sep. 2012.
- [5] J. C. Principe and A. J. Brockmeier, "Representing and decomposing neural potential signals," *Current Opinion Neurobiol.*, vol. 31, pp. 13–17, Apr. 2015.
- [6] L. Yang, X. Qi, F. Xing, T. Kurc, J. Saltz, and D. J. Foran, "Parallel content-based sub-image retrieval using hierarchical searching," *Bioinformatics*, vol. 30, no. 7, pp. 996–1002, Apr. 2014.
- [7] C. López, M. Lejeune, R. Bosch, A. Korzynska, M. García-Rojo, M. T. Salvadó, T. Alvaro, C. Callau, A. Roso, and J. Jaén, "Digital image analysis in breast cancer: An example of an automated methodology and the effects of image compression," *Stud. Health Technol. Inform.*, vol. 179, pp. 155–171, 2012.
- [8] D. J. Foran, Y. L., C. W., *et al.*, "Imageminer: A software system for comparative analysis of tissue microarrays using content-based image retrieval, high-performance computing, and grid technology," *J. Amer. Med. Inform. Assoc.*, vol. 8, no. 4, pp. 403–415, 2011.
- [9] L. Yang, W. Chen, P. Meer, G. Salaru, L. A. Goodell, V. Berstis, and D. J. Foran, "Virtual microscopy and grid-enabled decision support for large-scale analysis of imaged pathology specimens," *IEEE Trans. Inf. Technol. Biomed.*, vol. 13, no. 4, pp. 636–644, Jul. 2009.
- [10] L. Yang, W. Chen, P. Meer, G. Salaru, M. D. Feldman, and D. J. Foran, "High throughput analysis of breast cancer specimens on the grid," in *Proc. Int. Conf. Med. Image Comput. Comput.-Assisted Intervention*, 2007, vol. 4791, pp. 617–625.
- [11] G. Bueno, M. García-Rojo, O. Déniz, M. M. Fernández-Carrobles, N. Vázquez, J. Salido, and J. García-González, "Emerging trends: Grid technology in pathology," *Stud. Health Technol. Inform.*, vol. 179, pp. 218–229, 2012.
- [12] X. Zhang, L. Yang, W. Liu, H. Su, and S. Zhang, "Mining histopathological images via composite hashing and online learning," in *Proc.*



- Int. Conf. Med. Image Comput. Comput.-Assisted Intervention*, 2014, vol. 8674, pp. 479–486.
- [13] X. Zhang, H. Dou, T. Ju, and S. Zhang, “Fusing heterogeneous features for the image-guided diagnosis of intraductal breast lesions,” in *Proc. IEEE Int. Symp. Biomed. Imag.*, Apr. 2015, pp. 1288–1291.
  - [14] X. Zhang, W. Liu, M. Dundar, S. Badve, and S. Zhang, “Towards large-scale histopathological image analysis: Hashing-based image retrieval,” *IEEE Trans. Med. Imag.*, vol. 34, no. 2, pp. 496–506, Feb. 2015.
  - [15] M. N. Gurcan, L. E. Boucheron, A. Can, A. Madabushi, N. M. Rajpoot, and B. Yener, “Histopathological image analysis: A review,” *IEEE Rev. Biomed. Eng.*, vol. 2, pp. 147–171, 2009.
  - [16] C. Demir and B. Yener, “Automated cancer diagnosis based on histopathological images: A systematic survey,” Rensselaer Polytechnic Institute, Computer Science Department, Troy, NY, USA, Tech. Rep. TR0509, 2005.
  - [17] L. He, R. Long, S. Antani, and G. Thoma, “Computer assisted diagnosis in histopathology,” in *Sequence and Genome Analysis: Methods and Applications*, Z. Zhao, Ed., Hong Kong, China: iConcept Press, 2011, pp. 271–287.
  - [18] M. Veta, J. Pluim, P. van Diest, and M. Viergever, “Breast cancer histopathology image analysis: A review,” *IEEE Trans. Biomed. Eng.*, vol. 61, no. 5, pp. 1400–1411, May 2014.
  - [19] T. J. Fuchs and J. M. Buhmann, “Computational pathology: Challenges and promises for tissue analysis,” *Comput. Med. Imag. Graph.*, vol. 35, no. 7–8, pp. 515–530, 2011.
  - [20] S. Kothari, J. H. Phan, T. H. Stokes, and M. D. Wang, “Pathology imaging informatics for quantitative analysis of whole-slide images,” *J. Amer. Med. Inform. Assoc.*, vol. 20, no. 6, pp. 1099–1108, 2013.
  - [21] H. Irshad, A. Veillard, L. Roux, and D. Racoceanu, “Methods for nuclei detection, segmentation, and classification in digital histopathology: A review—Current status and future potential,” *IEEE Rev. Biomed. Eng.*, vol. 7, pp. 97–114, Apr. 2014.
  - [22] A. M. Khan, N. Rajpoot, D. Treanor, and D. Magee, “A nonlinear mapping approach to stain normalization in digital histopathology images using image-specific color deconvolution,” *IEEE Trans. Biomed. Eng.*, vol. 61, no. 6, pp. 1729–1738, Jun. 2014.
  - [23] M. T. McCann, J. A. Ozolek, C. A. Castro, B. Parvin, and J. Kovacevic, “Automated histology analysis: Opportunities for signal processing,” *IEEE Signal Process. Mag.*, vol. 32, no. 1, pp. 78–87, Jan. 2015.
  - [24] G. Bueno, M. M. Fernández-Carrobles, O. Déniz, J. Salido, N. Vázquez, and M. García-Rojo, “An entropy-based automated approach to prostate biopsy ROI segmentation,” *Diagnostic Pathol.*, vol. 8, no. 1, pp. 1–5, 2013.
  - [25] M. M. Fernández-Carrobles, I. Tadeo, R. Noguera, M. García-Rojo, O. Déniz, J. Salido, and G. Bueno, “A morphometric tool applied to angiogenesis research based on vessel segmentation,” *Diagnostic Pathol.*, vol. 8, no. 1, pp. 1–5, 2013.
  - [26] M. Wolk, J. E. Martin, and R. Constantin, “Blood cells with fetal haemoglobin (F-cells) detected by immunohistochemistry as indicators of solid tumours,” *J. Clin. Pathol.*, vol. 57, no. 7, pp. 740–745, Jul. 2004.
  - [27] M. Wolk, J. E. Martin, and C. Reinus, “Development of fetal haemoglobin-blood cells (F cells) within colorectal tumour tissues,” *J. Clin. Pathol.*, vol. 59, no. 6, pp. 598–602, Jun. 2006.
  - [28] U. Adiga, R. Malladi, R. Fernandez-Gonzalez, and C. O. de Solorzano, “High-throughput analysis of multispectral images of breast cancer tissue,” *IEEE Trans. Image Process.*, vol. 15, no. 8, pp. 2259–2268, Aug. 2006.
  - [29] P. Yan, X. Zhou, M. Shah, and S. T. C. Wong, “Automatic segmentation of high-throughput RNAi fluorescent cellular images,” *IEEE Trans. Inf. Technol. Biomed.*, vol. 12, no. 1, pp. 109–117, Jan. 2008.
  - [30] U. Adiga, B. Bell, L. Ponomareva, D. Taylor, R. Saldanha, S. Nelson, and T. Lamkin, “Mapping infected cell phenotype,” *IEEE Trans. Biomed. Eng.*, vol. 59, no. 8, pp. 2362–2371, Aug. 2012.
  - [31] M. Wang, X. Zhou, F. Li, J. Huckins, R. W. King, and S. T. C. Wong, “Novel cell segmentation and online SVM for cell cycle phase identification in automated microscopy,” *Bioinformatics*, vol. 24, no. 1, pp. 94–101, 2008.
  - [32] F. Li, X. Zhou, J. Ma, and S. T. C. Wong, “Multiple nuclei tracking using integer programming for quantitative cancer cell cycle analysis,” *IEEE Trans. Med. Imag.*, vol. 29, no. 1, pp. 96–105, Jan. 2010.
  - [33] G. Lin, U. Adiga, K. Olson, J. F. Guzowski, C. A. Barnes, and B. Roysam, “A hybrid 3D watershed algorithm incorporating gradient cues and object models for automatic segmentation of nuclei in confocal image stacks,” *Cytometry A*, vol. 56A, no. 1, pp. 23–36, Nov. 2003.
  - [34] C. Park, J. Z. Huang, J. X. Ji, and Y. Ding, “Segmentation, inference and classification of partially overlapping nanoparticles,” *IEEE Trans. Pattern Anal. Mach. Intell.*, vol. 35, no. 3, pp. 669–681, Mar. 2013.
  - [35] X. Yang, H. Li, and X. Zhou, “Nuclei segmentation using marker-controlled watershed, tracking using mean-shift, and Kalman filter in time-lapse microscopy,” *IEEE Trans. Circuits Syst.*, vol. 53, no. 11, pp. 2405–2414, Nov. 2006.
  - [36] E. Hodneland, N. Bukoreshtliev, T. Eichler, X.-C. Tai, S. Gurke, A. Lundervold, and H.-H. Gerdes, “A unified framework for automated 3-D segmentation of surface-stained living cells and a comprehensive segmentation evaluation,” *IEEE Trans. Med. Imag.*, vol. 28, no. 5, pp. 720–738, May 2009.
  - [37] M. E. Plissiti, C. Nikou, and A. Charchanti, “Automated detection of cell nuclei in pap smear images using morphological reconstruction and clustering,” *IEEE Trans. Inf. Technol. Biomed.*, vol. 15, no. 2, pp. 233–241, Mar. 2011.
  - [38] C. Lu and M. Mandal, “Toward automatic mitotic cell detection and segmentation in multispectral histopathological images,” *IEEE J. Biomed. Health Inform.*, vol. 18, no. 2, pp. 594–605, Mar. 2014.
  - [39] W. Shitong and W. Min, “A new detection algorithm (NDA) based on fuzzy cellular neural networks for white blood cell detection,” *IEEE Trans. Inf. Technol. Biomed.*, vol. 10, no. 1, pp. 5–10, Jan. 2006.
  - [40] M. Plissiti and C. Nikou, “Overlapping cell nuclei segmentation using a spatially adaptive active physical model,” *IEEE Trans. Image Process.*, vol. 21, no. 11, pp. 4568–4580, Nov. 2012.
  - [41] F. Raimondo, M. A. Gavrielides, G. Karayannopoulou, K. Lyroutia, I. Pitas, and I. Kostopoulos, “Automated evaluation of her-2/neu status in breast tissue from fluorescent in situ hybridization images,” *IEEE Trans. Image Process.*, vol. 14, no. 9, pp. 1288–1299, Sep. 2005.
  - [42] K. Thirusittampalam, M. Hossain, O. Ghita, and P. Whelan, “A novel framework for cellular tracking and mitosis detection in dense phase contrast microscopy images,” *IEEE J. Biomed. Health Inform.*, vol. 17, no. 3, pp. 642–653, May 2013.
  - [43] C. Wahlby, I. M. Sintorn, F. Erlandsson, G. Borgefors, and E. Bengtsson, “Combining intensity, edge and shape information for 2D and 3D segmentation of cell nuclei in tissue sections,” *J. Microsc.*, vol. 215, no. 1, pp. 67–76, Jul. 2004.
  - [44] J. Cheng and J. C. Rajapakse, “Segmentation of clustered nuclei with shape markers and marking function,” *IEEE Trans. Biomed. Eng.*, vol. 56, no. 3, pp. 741–748, Mar. 2009.
  - [45] C. Jung and C. Kim, “Segmenting clustered nuclei using H-minima transform-based marker extraction and contour parameterization,” *IEEE Trans. Biomed. Eng.*, vol. 57, no. 10, pp. 2600–2604, Oct. 2010.
  - [46] G. Li, V. Sanchez, G. Patel, S. Quenby, and N. Rajpoot, “Localisation of luminal epithelium edge in digital histopathology images of IHC stained slides of endometrial biopsies,” *Comput. Med. Imag. Graph.*, vol. 42, pp. 56–64, Jun. 2015.
  - [47] M. A. A. Dewan, M. O. Ahmad, and M. N. S. Swamy, “Tracking biological cells in time-lapse microscopy: An adaptive technique combining motion and topological features,” *IEEE Trans. Biomed. Eng.*, vol. 58, no. 6, pp. 1637–1647, Jun. 2011.
  - [48] M. Dewan, M. Ahmad, and M. Swamy, “A method for automatic segmentation of nuclei in phase-contrast images based on intensity, convexity and texture,” *IEEE Trans. Biomed. Circuits Syst.*, vol. 8, no. 5, pp. 716–728, Oct. 2014.
  - [49] C. R. J. Maurer, R. Qi, and V. Raghavan, “A linear time algorithm for computing exact Euclidean distance transforms of binary images in arbitrary dimensions,” *IEEE Trans. Pattern Anal. Mach. Intell.*, vol. 25, no. 2, pp. 265–270, Feb. 2003.
  - [50] N. Harder, M. Bodnar, R. Eils, D. Spector, and K. Rohr, “3D segmentation and quantification of mouse embryonic stem cells in fluorescence microscopy images,” in *Proc. IEEE Int. Symp. Biomed. Imag.*, Mar. 2011, pp. 216–219.
  - [51] P. Soille, *Morphological Image Analysis: Principles and Applications*. Berlin, Germany: Springer-Verlag, 1999.
  - [52] Q. Wu, F. A. Merchant, and K. R. Castleman, *Microscope Image Processing*. Burlington, MA, USA: Academic, 2008.
  - [53] R. C. Gonzalez and R. E. Woods, *Digital Image Processing*. Upper Saddle River, NJ, USA: Pearson, 2008.
  - [54] E. Dougherty, *Digital Image Processing Methods*. Boca Raton, FL, USA: CRC Press, 1994.
  - [55] A. Rosenfeld, “Measuring the sizes of concavities,” *Pattern Recogn. Lett.*, vol. 3, no. 1, pp. 71–75, Jan. 1985.
  - [56] S. G. Chang, B. Yu, and M. Vetterli, “Spatially adaptive wavelet thresholding with context modeling for image denoising,” *IEEE Trans. Image Process.*, vol. 9, no. 9, pp. 1522–1531, Sep. 2000.



- [57] X. Zhou, K.-Y. Liu, P. Bradley, N. Perrimon, and S. T. C. Wong, "Towards automated cellular image segmentation for RNAi genome-wide screening," in *Proc. Int. Conf. Med. Image Comput. Comput.-Assisted Intervention*, 2005, vol. 3749, pp. 885–892.
- [58] L. Vincent, "Morphological grayscale reconstruction in image analysis: Applications and efficient algorithms," *IEEE Trans. Image Process.*, vol. 2, no. 2, pp. 176–201, Apr. 1993.
- [59] J. C. Bezdek and S. K. Pal, *Fuzzy Models for Pattern Recognition*. New York, NY, USA: IEEE Press, 1992.
- [60] N. Christianini and J. S. Taylor, *Support Vector Machines and Other Kernel-Based Methods*. Cambridge, U.K.: Cambridge Univ. Press, 2000.
- [61] H. Masmoudi, S. M. Hewitt, N. Petrick, K. J. Myers, and M. A. Gavrielides, "Automated quantitative assessment of her-2/neu immunohistochemical expression in breast cancer," *IEEE Trans. Med. Imag.*, vol. 28, no. 6, pp. 916–925, Jun. 2009.
- [62] E. Bengtsson, C. Wahlby, and J. Lindblad, "Robust cell image segmentation methods," *Pattern Recog. Image Anal.*, vol. 14, no. 2, pp. 157–167, 2004.
- [63] N. Otsu, "A threshold selection method from gray-level histograms," *IEEE Trans. Syst., Man, Cybern.*, vol. 9, no. 1, pp. 62–66, Jan. 1979.
- [64] A. Fitzgibbon, M. Pilu, and R. Fisher, "Direct least square fitting of ellipses," *IEEE Trans. Pattern Anal. Mach. Intell.*, vol. 21, no. 5, pp. 476–480, May 1999.
- [65] W. Tarnawski, V. Kurtcuoglu, P. Lorek, M. Bodych, J. Rotter, M. Muszkieta, L. Piwowar, D. Poulikakos, M. Majkowski, and A. Ferrari, "A robust algorithm for segmenting and tracking clustered cells in time-lapse fluorescent microscopy," *IEEE J. Biomed. Health Inform.*, vol. 17, no. 4, pp. 862–869, Jul. 2013.
- [66] K. Mkrtchyan, D. Singh, M. Liu, V. Reddy, A. Roy-Chowdhury, and M. Gopi, "Efficient cell segmentation and tracking of developing plant meristem," in *Proc. IEEE Int. Conf. Image Process.*, Sep. 2011, pp. 2165–2168.
- [67] J. Byun, M. R. Verardo, B. Sumengen, G. Lewis, B. S. Manjunath, and S. K. Fisher, "Automated tool for the detection of cell nuclei in digital microscopic images: Application to retinal images," *Mol. Vis.*, vol. 12, pp. 949–960, Aug. 2006.
- [68] Y. Al-Kofahi, W. Lassoued, W. Lee, and B. Roysam, "Improved automatic detection and segmentation of cell nuclei in histopathology images," *IEEE Trans. Biomed. Eng.*, vol. 57, no. 4, pp. 841–852, Apr. 2010.
- [69] H. Chang, J. Han, A. Borowsky, L. Loss, J. Gray, P. Spellman, and B. Parvin, "Invariant delineation of nuclear architecture in glioblastoma multiforme for clinical and molecular association," *IEEE Trans. Med. Imag.*, vol. 32, no. 4, pp. 670–682, Apr. 2013.
- [70] H. Kong, H. C. Akakin, and S. E. Sarma, "A generalized Laplacian of Gaussian filter for blob detection and its applications," *IEEE Trans. Cybern.*, vol. 43, no. 6, pp. 1719–1733, Dec. 2013.
- [71] M. Zhang, T. Wu, and K. M. Bennett, "Small blob identification in medical images using regional features from optimum scale," *IEEE Trans. Biomed. Eng.*, vol. 62, no. 4, pp. 1051–1062, Apr. 2015.
- [72] G. G. Lee, H. Lin, M. Tsai, S. Chou, W. Lee, Y. Liao, C. Sun, and C. Chen, "Automatic cell segmentation and nuclear-to-cytoplasmic ratio analysis for third harmonic generated microscopy medical images," *IEEE Trans. Biomed. Circuits Syst.*, vol. 7, no. 2, pp. 158–168, Apr. 2013.
- [73] P. Quelhas, M. Marcuzzo, A. Mendonca, and A. Campilho, "Cell nuclei and cytoplasm joint segmentation using the sliding band filter," *IEEE Trans. Med. Imag.*, vol. 29, no. 8, pp. 1463–1473, Aug. 2010.
- [74] Z. Lu, G. Carneiro, and A. P. Bradley, "An improved joint optimization of multiple level set functions for the segmentation of overlapping cervical cells," *IEEE Trans. Image Process.*, vol. 24, no. 4, pp. 1261–1272, Apr. 2015.
- [75] C. Arteta, V. Lempitsky, J. A. Noble, and A. Zisserman, "Detecting overlapping instances in microscopy images using extremal region trees," *Med. Image Anal.*, vol. 27, pp. 3–16, Jan. 2016.
- [76] R. Bise and Y. Sato, "Cell detection from redundant candidate regions under nonoverlapping constraints," *IEEE Trans. Med. Imag.*, vol. 34, no. 7, pp. 1417–1427, Jul. 2015.
- [77] C. Bergmeir, M. G. Silvente, and J. M. Benítez, "Segmentation of cervical cell nuclei in high-resolution microscopic images: A new algorithm and a web-based software framework," *Comput. Methods Programs Biomed.*, vol. 107, no. 3, pp. 497–512, 2012.
- [78] P. Filipczuk, T. Fevens, A. Krzyzak, and R. Monczak, "Computer-aided breast cancer diagnosis based on the analysis of cytological images of fine needle biopsies," *IEEE Trans. Med. Imag.*, vol. 32, no. 12, pp. 2169–2178, Dec. 2013.
- [79] O. Sertel, G. Lozanski, A. Shana'ah, and M. N. Gurcan, "Computer-aided detection of centroblasts for follicular lymphoma grading using adaptive likelihood-based cell segmentation," *IEEE Trans. Biomed. Eng.*, vol. 57, no. 10, pp. 2613–2616, Oct. 2010.
- [80] X. Qi, F. Xing, D. J. Foran, and L. Yang, "Robust segmentation of overlapping cells in histopathology specimens using parallel seed detection and repulsive level set," *IEEE Trans. Biomed. Eng.*, vol. 59, no. 3, pp. 754–765, Mar. 2012.
- [81] X. Zhang, F. Xing, H. Su, L. Yang, and S. Zhang, "High-throughput histopathological image analysis via robust cell segmentation and hashing," *Med. Image Anal.*, vol. 26, no. 1, pp. 306–315, Dec. 2015.
- [82] F. Xing, H. Su, J. Neltner, and L. Yang, "Automatic Ki-67 counting using robust cell detection and online dictionary learning," *IEEE Trans. Biomed. Eng.*, vol. 61, no. 3, pp. 859–870, Mar. 2014.
- [83] H. Xu, C. Lu, and M. Mandal, "An efficient technique for nuclei segmentation based on ellipse descriptor analysis and improved seed detection algorithm," *IEEE J. Biomed. Health Inform.*, vol. 18, no. 5, pp. 1729–1741, Sep. 2014.
- [84] R. C. Gonzalez, R. E. Woods, and S. L. Eddins, *Digital Image Processing Using MATLAB*. Upper Saddle River, NJ, USA: Pearson, 2004.
- [85] T. Lindeberg, "Feature detection with automatic scale selection," *Int. J. Comput. Vis.*, vol. 30, no. 2, pp. 79–116, Nov. 1998.
- [86] H. Peng, X. Zhou, F. Li, X. Xia, and S. T. C. Wong, "Integrating multi-scale blob/curvilinear detector techniques and multi-level sets for automated segmentation of stem cell images," in *Proc. IEEE Int. Symp. Biomed. Imag.*, Jun. 2009, pp. 1362–1365.
- [87] F. Li, X. Zhou, H. Zhao, and S. T. C. Wong, "Cell segmentation using front vector flow guided active contours," in *Proc. Int. Conf. Med. Image Comput. Comput.-Assisted Intervention*, 2009, vol. 5762, pp. 609–616.
- [88] X. Wu, Y. Chen, B. R. Brooks, and Y. A. Su, "The local maximum clustering method and its application in microarray gene expression data analysis," *EURASIP J. Appl. Signal Process.*, vol. 2004, no. 1, pp. 53–63, Jan. 2004.
- [89] L. Rojas, G. Martinez, and T. Scheper, "Cell counting based on local intensity maxima grouping for in-situ microscopy," in *Proc. IEEE Int. Symp. Biomed. Imag.*, Apr. 2014, pp. 1344–1347.
- [90] J. Matas, O. Chum, M. Urban, and T. Pajdla, "Robust wide-baseline stereo from maximally stable extremal regions," *Image Vision Comput.*, vol. 22, no. 10, pp. 761–767, Feb. 2004.
- [91] Z. Lu, G. Carneiro, and A. P. Bradley, "Automated nucleus and cytoplasm segmentation of overlapping cervical cells," in *Proc. Int. Conf. Med. Image Comput. Comput.-Assisted Intervention*, 2013, vol. 8149, pp. 452–460.
- [92] C. Arteta, V. Lempitsky, J. A. Noble, and A. Zisserman, "Learning to detect cells using non-overlapping extremal regions," in *Proc. Int. Conf. Med. Image Comput. Comput.-Assisted Intervention*, 2012, vol. 7510, pp. 348–356.
- [93] P. D. Kostelec, L. M. Carliny, and B. Glocker, "Learning to detect and track cells for quantitative analysis of time-lapse microscopic image sequences," in *Proc. IEEE Int. Symp. Biomed. Imag.*, 2015, pp. 1544–1547.
- [94] P. V. C. Hough, "Methods and means for recognizing complex patterns," Patent US 3 069 654, Jun. 1962.
- [95] R. O. Duda and P. E. Hart, "Use of the Hough transformation to detect lines and curves in pictures," *Commun. ACM*, vol. 15, no. 1, pp. 11–15, Jan. 1972.
- [96] D. H. Ballard, "Generalizing the Hough transform to detect arbitrary shapes," *Pattern Recog.*, vol. 13, no. 2, pp. 111–122, 1981.
- [97] N. Ramesh, M. Salama, and T. Tasdizen, "Segmentation of haematopoietic cells in bone marrow using circle detection and splitting techniques," in *Proc. IEEE Int. Symp. Biomed. Imag.*, May 2012, pp. 206–209.
- [98] C. Zanella, M. Campana, B. Rizzi, C. Melani, G. Sanguinetti, P. Bourguine, K. Mikula, N. Peyrieras, and A. Sarti, "Cells segmentation from 3-D confocal images of early zebrafish embryogenesis," *IEEE Trans. Image Process.*, vol. 19, no. 3, pp. 770–781, Mar. 2010.
- [99] J. Canny, "A computational approach to edge detection," *IEEE Trans. Pattern Anal. Mach. Intell.*, vol. PAMI-8, no. 6, pp. 679–698, Nov. 1986.
- [100] K. Lee and W. N. Street, "An adaptive resource-allocating network for automated detection, segmentation, and classification of breast cancer nuclei topic area: Image processing and recognition," *IEEE Trans. Neural Netw.*, vol. 14, no. 3, pp. 680–687, May 2003.
- [101] E. Cosatto, M. Miller, H. P. Graf, and J. S. Meyer, "Grading nuclear pleomorphism on histological micrographs," in *Proc. IEEE Int. Conf. Pattern Recog.*, Dec. 2008, pp. 1–4.

- [102] C. Ortiz De Solorzano, R. Malladi, S. A. Lelievre, and S. J. Lockett, "Segmentation of nuclei and cells using membrane related protein markers," *J. Microsc.*, vol. 201, no. 3, pp. 404–415, Mar. 2001.
- [103] C. Zhang, F. Huber, M. Knop, and F. A. Hamprecht, "Yeast cell detection and segmentation in bright field microscopy," in *Proc. IEEE Int. Symp. Biomed. Imag.*, Apr. 2014, pp. 1267–1270.
- [104] C. Sommer, C. Straehle, U. Kothe, and F. A. Hamprecht, "Ilastik: Interactive learning and segmentation toolkit," in *Proc. IEEE Int. Symp. Biomed. Imag.*, Mar. 2011, pp. 230–233.
- [105] D. Reissfeld, H. Wolfson, and Y. Yeshurun, "Context-free attentional operators: The generalized symmetry transform," *Int. J. Comput. Vis.*, vol. 14, no. 2, pp. 119–130, Mar. 1995.
- [106] D. Reissfeld and Y. Yeshurun, "Preprocessing of face images: Detection of features and pose normalization," *Comput. Vis. Image Understanding*, vol. 71, no. 3, pp. 413–430, Sep. 1998.
- [107] G. Loy and A. Zelinsky, "Fast radial symmetry for detecting points of interest," *IEEE Trans. Pattern Anal. Mach. Intell.*, vol. 25, no. 8, pp. 959–973, Aug. 2003.
- [108] M. Veta, A. Huisman, M. Viergever, P. J. Van Diest, and J. P. W. Pluim, "Marker-controlled watershed segmentation of nuclei in stained breast cancer biopsy images," in *Proc. IEEE Int. Symp. Biomed. Imag.*, 2011, pp. 618–621.
- [109] S. Ram and J. Rodriguez, "Symmetry-based detection of nuclei in microscopy images," in *Proc. IEEE Int. Conf. Acoust., Speech, Signal Process.*, May 2013, pp. 1128–1132.
- [110] J. Ni, M. K. Singh, and C. Bahlmann, "Fast radial symmetry detection under affine transformations," in *Proc. IEEE Conf. Comput. Vis. Pattern Recog.*, Jun. 2012, pp. 932–939.
- [111] B. Parvin, Q. Yang, J. Han, H. Chang, B. Rydberg, and M. H. Barcellos-Hoff, "Iterative voting for inference of structural saliency and characterization of subcellular events," *IEEE Trans. Image Process.*, vol. 16, no. 3, pp. 615–623, Mar. 2007.
- [112] H. Chang, Q. Yang, and B. Parvin, "Segmentation of heterogeneous blob objects through voting and level set formulation," *Pattern Recogn. Lett.*, vol. 28, no. 13, pp. 1781–1787, Oct. 2007.
- [113] A. Kuijper and B. Heise, "An automatic cell segmentation method for differential interference contrast microscopy," in *Proc. IEEE Int. Conf. Pattern Recog.*, Dec. 2008, pp. 1–4.
- [114] I. Ersoy, F. Bunyak, J. Higgins, and K. Palaniappan, "Coupled edge profile active contours for red blood cell flow analysis," in *Proc. IEEE Int. Symp. Biomed. Imag.*, May 2012, pp. 748–751.
- [115] O. Schmitt and M. Hasse, "Radial symmetries based decomposition of cell clusters in binary and gray level images," *Pattern Recog.*, vol. 41, no. 6, pp. 1905–1923, Jun. 2008.
- [116] Q. Yang and B. Parvin, "Harmonic cut and regularized centroid transform for localization of subcellular structure," *IEEE Trans. Biomed. Eng.*, vol. 50, no. 4, pp. 469–475, Apr. 2003.
- [117] D. Comaniciu and P. Meer, "Mean shift: A robust approach toward feature space analysis," *IEEE Trans. Pattern Anal. Mach. Intell.*, vol. 24, no. 5, pp. 603–619, May 2002.
- [118] X. Zhang, H. Su, L. Yang, and S. Zhang, "Fine-grained histopathological image analysis via robust segmentation and large-scale retrieval," in *Proc. IEEE Conf. Comput. Vis. Pattern Recog.*, 2015, pp. 5361–5368.
- [119] F. Xing and L. Yang, "Robust cell segmentation for non-small cell lung cancer," in *Proc. IEEE Int. Symp. Biomed. Imag.*, Apr. 2013, pp. 386–389.
- [120] X. Zhang, H. Su, L. Yang, and S. Zhang, "Weighted hashing with multiple cues for cell-level analysis of histopathological images," in *Proc. Inf. Process. Med. Imag.*, 2015, vol. 9123, pp. 303–314.
- [121] F. Xing, H. Su, and L. Yang, "An integrated framework for automatic Ki-67 scoring in pancreatic neuroendocrine tumor," in *Proc. Int. Conf. Med. Image Comput. Comput.-Assisted Intervention*, 2013, vol. 8149, pp. 436–443.
- [122] H. Su, F. Xing, J. D. Lee, C. A. Peterson, and L. Yang, "Automatic myonuclear detection in isolated single muscle fibers using robust ellipse fitting and sparse representation," *IEEE Trans. Comput. Biol. Bioinfo.*, vol. 11, no. 4, pp. 714–726, Jul. 2014.
- [123] K. Z. Mao, P. Zhao, and P. H. Tan, "Supervised learning-based cell image segmentation for p53 immunohistochemistry," *IEEE Trans. Biomed. Eng.*, vol. 53, no. 6, pp. 1153–1163, Jun. 2006.
- [124] F. Mualla, S. Scholl, B. Sommerfeldt, A. Maier, and J. Hornegger, "Automatic cell detection in bright-field microscope images using SIFT, random forests, and hierarchical clustering," *IEEE Trans. Med. Imag.*, vol. 32, no. 12, pp. 2274–2286, Dec. 2013.
- [125] F. Xing, Y. Xie, and L. Yang, "An automatic learning-based framework for robust nucleus segmentation," *IEEE Trans. Med. Imag.*, vol. 35, no. 2, pp. 550–566, Feb. 2016.
- [126] Y. Song, L. Zhang, S. Chen, D. Ni, B. Lei, and T. Wang, "Accurate segmentation of cervical cytoplasm and nuclei based on multi-scale convolutional network and graph partitioning," *IEEE Trans. Biomed. Eng.*, vol. 62, no. 10, pp. 2421–2433, Oct. 2015.
- [127] C. Chen, W. Wang, J. A. Ozolek, and G. K. Rohde, "A flexible and robust approach for segmenting cell nuclei from 2D microscopy images using supervised learning and template matching," *Cytometry, A*, vol. 83A, no. 5, pp. 495–507, May 2013.
- [128] G. Dong, N. Ray, and S. T. Acton, "Intravital leukocyte detection using the gradient inverse coefficient of variation," *IEEE Trans. Med. Imag.*, vol. 24, no. 7, pp. 910–924, Jul. 2005.
- [129] K. Sirinukunwattana, A. M. Khan, and N. M. Rajpoot, "Cell words: Modelling the visual appearance of cells in histopathology images," *Comput. Med. Imag. Graph.*, vol. 42, pp. 16–24, 2015.
- [130] C. M. Bishop, *Pattern Recognition and Machine Learning*. New York, NY, USA: Springer Science+Business Media, LLC, 2006.
- [131] C. Cortes and V. Vapnik, "Support-vector networks," *Mach. Learn.*, vol. 20, no. 3, pp. 273–297, Sep. 1995.
- [132] H. Su, F. Xing, J. D. Lee, C. A. Peterson, and L. Yang, "Learning based automatic detection of myonuclei in isolated single skeletal muscle fibers using multi-focus image fusion," in *Proc. IEEE Int. Symp. Biomed. Imag.*, Apr. 2013, pp. 432–435.
- [133] B. Matei and P. Meer, "A general method for errors-in-variables problems in computer vision," in *Proc. IEEE Conf. Comput. Vis. Pattern Recog.*, 2000, vol. 2, pp. 18–25.
- [134] P. Khurd, L. Grady, A. Kamen, S. Gibbs-Strauss, E. M. Genega, and J. V. Frangioni, "Network cycle features: Application to computer-aided gleason grading of prostate cancer histopathological images," in *Proc. IEEE Int. Symp. Biomed. Imag.*, Mar. 2011, pp. 1632–1636.
- [135] C. Sommer, L. Fiaschi, F. A. Hamprecht, and D. W. Gerlich, "Learning-based mitotic cell detection in histopathological images," in *Proc. IEEE Int. Conf. Pattern Recog.*, Nov. 2012, pp. 2306–2309.
- [136] M. Held, M. H. A. Schmitz, B. Fischer, T. Walter, B. Neumann, M. H. Olma, M. Peter, J. Ellenberg, and D. W. Gerlich, "CellCognition: Time-resolved phenotype annotation in high-throughput live cell imaging," *Nature Methods*, vol. 7, no. 9, pp. 747–754, Sep. 2010.
- [137] A. M. Khan, H. El-Daly, and N. M. Rajpoot, "A gamma-Gaussian mixture model for detection of mitotic cells in breast cancer histopathology images," in *Proc. IEEE Int. Conf. Pattern Recog.*, Nov. 2012, pp. 149–152.
- [138] L. Breiman, "Random forests," *Mach. Learn.*, vol. 45, no. 1, pp. 5–32, Oct. 2001.
- [139] P. Dollar and C. L. Zitnick, "Fast edge detection using structured forests," arXiv: 1406.5549, 2014.
- [140] F. Mualla, S. Scholl, B. Sommerfeldt, S. Steidl, R. Buchholz, and J. Hornegger, "Improving joint learning of suspended and adherent cell detection using low-pass monogenic phase and transport of intensity equation," in *Proc. IEEE Int. Symp. Biomed. Imag.*, Apr. 2014, pp. 927–930.
- [141] D. G. Lowe, "Distinctive image features from scale-invariant keypoints," *Int. J. Comput. Vis.*, vol. 60, no. 2, pp. 91–110, Nov. 2004.
- [142] C. Chen, A. Liaw, and L. Breiman, "Using random forest to learn imbalanced data," University of California, Berkeley, CA, Tech. Rep. 666, 2004.
- [143] J. Gall, A. Yao, N. Razavi, L. Van Gool, and V. Lempitsky, "Hough forests for object detection, tracking, and action recognition," *IEEE Trans. Pattern Anal. Mach. Intell.*, vol. 33, no. 11, pp. 2188–2202, Nov. 2011.
- [144] J. Gall and V. Lempitsky, "Class-specific Hough forests for object detection," in *Proc. IEEE Conf. Comput. Vis. Pattern Recog.*, Jun. 2009, pp. 1022–1029.
- [145] A. Yao, J. Gall, C. Leistner, and L. Van Gool, "Interactive object detection," in *Proc. IEEE Conf. Comput. Vis. Pattern Recog.*, Jun. 2012, pp. 3242–3249.
- [146] S. Schuster, C. Leistner, P. M. Roth, L. van Gool, and H. Bischof, "Online Hough-forests," in *Proc. Brit. Mach. Vis. Conf.*, 2011, pp. 128–1–128–11.
- [147] L. Deng and D. Yu, "Deep learning: Methods and applications," *Found. Trends Signal Process.*, vol. 3, no. 3–4, pp. 197–387, 2013.
- [148] Y. LeCun, Y. Bengio, and G. Hinton, "Deep learning," *Nature*, vol. 521, no. 28, pp. 436–444, May 2015.
- [149] H. R. Roth, L. Lu, A. Seff, K. M. Cherry, J. Hoffman, S. Wang, J. Liu, E. Turkbey, and R. M. Summers, "A new 2.5D representation for lymph node detection using random sets of deep convolutional neural network observations," in *Proc. Int. Conf. Med. Image Comput. Comput.-Assisted Intervention*, 2014, vol. 8673, pp. 520–527.

- [150] Y. LeCun, L. Bottou, Y. Bengio, and P. Haffner, "Gradient-based learning applied to document recognition," *Proc. IEEE*, vol. 86, no. 11, pp. 2278–2324, Nov. 1998.
- [151] Y. LeCun, K. Kavukcuoglu, and C. Farabet, "Convolutional networks and applications in vision," in *Proc. IEEE Int. Symp. Circuits Syst.*, May 2010, pp. 253–256.
- [152] A. Krizhevsky, I. Sutskever, and G. E. Hinton, "Imagenet classification with deep convolutional neural networks," in *Proc. Adv. Neural Inf. Process. Syst.*, 2012, pp. 1097–1105.
- [153] C. Farabet, C. Couprie, L. Najman, and Y. LeCun, "Learning hierarchical features for scene labeling," *IEEE Trans. Pattern Anal. Mach. Intell.*, vol. 35, no. 8, pp. 1915–1929, Aug. 2013.
- [154] R. Collobert and J. Weston, "A unified architecture for natural language processing: Deep neural networks with multitask learning," in *Proc. Int. Conf. Mach. Learn.*, 2008, pp. 160–167.
- [155] D. C. Ciresan, A. Giusti, L. M. Gambardella, and J. Schmidhuber, "Mitosis detection in breast cancer histology images with deep neural networks," in *Proc. Int. Conf. Med. Image Comput. Comput.-Assisted Intervention*, 2013, vol. 8150, pp. 411–418.
- [156] B. Dong, L. Shao, M. D. Costa, O. Bandmann, and A. F. Frangi, "Deep learning for automatic cell detection in wide-field microscopy zebrafish images," in *Proc. IEEE Int. Symp. Biomed. Imag.*, Apr. 2015, pp. 772–776.
- [157] Y. Mao, Z. Yin, and J. M. Schober, "Iteratively training classifiers for circulating tumor cell detection," in *Proc. IEEE Int. Symp. Biomed. Imag.*, Apr. 2015, pp. 190–194.
- [158] F. Liu and L. Yang, "A novel cell detection method using deep convolutional neural network and maximum-weight independent set," in *Proc. Int. Conf. Med. Image Comput. Comput.-Assisted Intervention*, 2015, vol. 9351, pp. 349–357.
- [159] R. Achanta, A. Shaji, K. Smith, A. Lucchi, P. Fua, and S. Susstrunk, "SLIC superpixels compared to state-of-the-art superpixel methods," *IEEE Trans. Pattern Anal. Mach. Intell.*, vol. 34, no. 11, pp. 2274–2282, Nov. 2012.
- [160] Y. Boykov and V. Kolmogorov, "An experimental comparison of min-cut/max-flow algorithms for energy minimization in vision," *IEEE Trans. Pattern Anal. Mach. Intell.*, vol. 26, no. 9, pp. 1124–1137, Sep. 2004.
- [161] H. Yang and N. Ahuja, "Automatic segmentation of granular objects in images: Combining local density clustering and gradient-barrier watershed," *Pattern Recog.*, vol. 47, no. 6, pp. 2266–2279, Jun. 2014.
- [162] Y. Xie, X. Kong, F. Xing, F. Liu, H. Su, and L. Yang, "Deep voting: A robust approach toward nucleus localization in microscopy images," in *Proc. Int. Conf. Med. Image Comput. Comput.-Assisted Intervention*, 2015, vol. 9351, pp. 374–382.
- [163] A. Giusti, D. Ciresan, J. Masci, L. Gambardella, and J. Schmidhuber, "Fast image scanning with deep max-pooling convolutional neural networks," in *Proc. IEEE Int. Conf. Image Process.*, Sep. 2013, pp. 4034–4038.
- [164] Y. Xie, F. Xing, X. Kong, and L. Yang, "Beyond classification: Structured regression for robust cell detection using convolutional neural network," in *Proc. Int. Conf. Med. Image Comput. Comput.-Assisted Intervention*, 2015, vol. 9351, pp. 358–365.
- [165] J. A. Ozolek, A. B. Tosun, W. Wang, C. Chen, S. Kolouri, S. Basu, H. Huang, and G. K. Rohde, "Accurate diagnosis of thyroid follicular lesions from nuclear morphology using supervised learning," *Med. Image Anal.*, vol. 18, no. 5, pp. 772–780, 2014.
- [166] H. Su, F. Xing, X. Kong, Y. Xie, S. Zhang, and L. Yang, "Robust cell detection and segmentation in histopathological images using sparse reconstruction and stacked denoising autoencoders," in *Proc. Int. Conf. Med. Image Comput. Comput.-Assisted Intervention*, 2015, vol. 9351, pp. 383–390.
- [167] B. Liu, J. Huang, L. Yang, and C. Kulikowski, "Robust tracking using local sparse appearance model and k-selection," in *Proc. IEEE Conf. Comput. Vis. Pattern Recog.*, Jun. 2011, pp. 1313–1320.
- [168] J. Wright, A. Y. Yang, A. Ganesh, S. S. Sastry, and Y. Ma, "Robust face recognition via sparse representation," *IEEE Trans. Pattern Anal. Mach. Intell.*, vol. 31, no. 2, pp. 210–227, Feb. 2009.
- [169] D. Mayerich, J. Kwon, A. Panchal, J. Keyser, and Y. Choe, "Fast cell detection in high-throughput imagery using GPU-accelerated machine learning," in *Proc. IEEE Int. Symp. Biomed. Imag.*, Mar. 2011, pp. 719–723.
- [170] M. Sezgin and B. Sankur, "Survey over image thresholding techniques and quantitative performance evaluation," *J. Electron. Imag.*, vol. 13, no. 1, pp. 146–168, Jan. 2004.
- [171] X. Chen, X. Zhou, and S. T. C. Wong, "Automated segmentation, classification, and tracking of cancer cell nuclei in time-lapse microscopy," *IEEE Trans. Biomed. Eng.*, vol. 53, no. 4, pp. 762–766, Apr. 2006.
- [172] F. Long, H. Peng, and E. Myers, "Automatic segmentation of nuclei in 3D microscopy images of *C. elegans*," in *Proc. IEEE Int. Symp. Biomed. Imag.*, Apr. 2007, pp. 536–539.
- [173] J. Peng, Y. Chen, M. D. Green, S. L. Forsburg, and C. Hsu, "Robust cell segmentation for *Schizosaccharomyces pombe* images with focus gradient," in *Proc. IEEE Int. Symp. Biomed. Imag.*, Apr. 2013, pp. 414–417.
- [174] C. Callau, M. Lejeune, A. Korczynska, M. García-Rojo, G. Bueno, R. Bosch, J. Jaén, G. Orero, T. Salvadó, and C. López, "Evaluation of cytokeratin-19 in breast cancer tissue samples: A comparison of automatic and manual evaluations of scanned tissue microarray cylinders," *Biomed. Eng. OnLine*, vol. 14, no. 2, pp. 1–11, 2014.
- [175] S. J. Keenan, J. Diamond, W. G. McCluggage, H. Bharucha, D. Thompson, P. H. Bartels, and P. W. Hamilton, "An automated machine vision system for the histological grading of cervical intraepithelial neoplasia (CIN)," *J. Pathol.*, vol. 192, no. 3, pp. 351–362, Nov. 2000.
- [176] J. Kong, F. Wang, G. Teodoro, Y. Liang, Y. Zhu, C. Tucker-Burden, and D. J. Brat, "Automated cell segmentation with 3D fluorescence microscopy images," in *Proc. IEEE Int. Symp. Biomed. Imag.*, Apr. 2015, pp. 1212–1215.
- [177] X. Zhou, F. Li, J. Yan, and S. T. C. Wong, "A novel cell segmentation method and cell phase identification using Markov model," *IEEE Trans. Inf. Technol. Biomed.*, vol. 13, no. 2, pp. 152–157, Mar. 2009.
- [178] C. Ortiz de Solorzano, R. E. Garcia, A. Jones, D. Pinkel, J. W. Gray, D. Sudar, and S. J. Lockett, "Segmentation of confocal microscope images of cell nuclei in thick tissue sections," *J. Microsc.*, vol. 193, no. 3, pp. 212–226, Mar. 1999.
- [179] D. Forsberg and N. Monsef, "Evaluating cell nuclei segmentation for use on whole-slide images in lung cytology," in *Proc. IEEE Int. Conf. Pattern Recog.*, Aug. 2014, pp. 3380–3385.
- [180] G. Li, T. Liu, J. Nie, L. Guo, J. Chen, J. Zhu, W. Xia, A. Mara, S. Holley, and S. T. C. Wong, "Segmentation of touching cell nuclei using gradient flow tracking," *J. Microsc.*, vol. 231, no. 1, pp. 47–58, Jul. 2008.
- [181] C. Davatzikos, J. L. Prince, and R. N. Bryan, "Image registration based on boundary mapping," *IEEE Trans. Med. Imag.*, vol. 15, no. 1, pp. 112–115, Feb. 1996.
- [182] S. Wienert, D. Heim, K. Saeger, A. Stenzinger, M. Beil, P. Hufnagl, M. Dietel, C. Denkert, and F. Klauschen, "Detection and segmentation of cell nuclei in virtual microscopy images—a minimum-model approach," *Sci. Rep.*, vol. 2, no. 503, pp. 1–7, Jul. 2012.
- [183] R. A. C. and J. D. A., "Quantification of histochemical staining by color deconvolution," *Anal. Quant. Cytol. Histol.*, vol. 23, no. 4, pp. 291–299, Aug. 2001.
- [184] D. Padfield, J. Rittscher, and B. Roysam, "Coupled minimum-cost flow cell tracking for high-throughput quantitative analysis," *Med. Image Anal.*, vol. 15, no. 4, pp. 650–668, Aug. 2011.
- [185] G. Lin, M. K. Chawla, K. Olson, J. F. Guzowski, C. A. Barnes, and B. Roysam, "Hierarchical, model-based merging of multiple fragments for improved three-dimensional segmentation of nuclei," *Cytometry, A*, vol. 63A, no. 1, pp. 20–33, Jan. 2005.
- [186] G. Lin, M. K. Chawla, K. Olson, C. A. Barnes, J. F. Guzowski, C. Bjornsson, W. Shain, and B. Roysam, "A multi-model approach to simultaneous segmentation and classification of heterogeneous populations of cell nuclei in 3D confocal microscope images," *Cytometry, A*, vol. 71A, no. 9, pp. 724–736, Sep. 2007.
- [187] F. Long, H. Peng, X. Liu, S. K. Kim, and E. Myers, "A 3D digital atlas of *C. elegans* and its application to single-cell analyses," *Nature Methods*, vol. 6, no. 9, pp. 667–672, Sep. 2009.
- [188] M. Maska, O. Danek, S. Garasa, A. Rouzaut, A. Munoz-Barrutia, and C. Ortiz-de Solorzano, "Segmentation and shape tracking of whole fluorescent cells based on the Chan-Vese model," *IEEE Trans. Med. Imag.*, vol. 32, no. 6, pp. 995–1006, Jun. 2013.
- [189] O. Dzyubachyk, W. A. van Cappellen, J. Essers, W. J. Niessen, and E. Meijering, "Advanced level-set-based cell tracking in time-lapse fluorescence microscopy," *IEEE Trans. Med. Imag.*, vol. 29, no. 3, pp. 852–867, Mar. 2010.
- [190] G. Xiong, X. Zhou, and L. Ji, "Automated segmentation of drosophila RNAi fluorescence cellular images using deformable models," *IEEE Trans. Circuits Syst. I*, vol. 53, no. 11, pp. 2415–2424, Nov. 2006.
- [191] P. Wu, J. Yi, G. Zhao, Z. Huang, B. Qiu, and D. Gao, "Active contour-based cell segmentation during freezing and its application in cryop-



- reservation," *IEEE Trans. Biomed. Eng.*, vol. 62, no. 1, pp. 284–295, Jan. 2015.
- [192] J. P. Bergeest and K. Rohr, "Efficient globally optimal segmentation of cells in fluorescence microscopy images using level sets and convex energy functionals," *Med. Image Anal.*, vol. 16, no. 7, pp. 1436–1444, 2012.
- [193] H. Fatakdawala, J. Xu, A. Basavanthally, G. Bhanot, S. Ganesan, M. Feldman, J. E. Tomaszewski, and A. Madabhushi, "Expectation-maximization-driven geodesic active contour with overlap resolution (EMaGACOR): Application to lymphocyte segmentation on breast cancer histopathology," *IEEE Trans. Biomed. Eng.*, vol. 57, no. 7, pp. 1676–1689, Jul. 2010.
- [194] H. Chang, J. Han, P. T. Spellman, and B. Parvin, "Multireference level set for the characterization of nuclear morphology in glioblastoma multiforme," *IEEE Trans. Biomed. Eng.*, vol. 59, no. 12, pp. 3460–3467, Dec. 2012.
- [195] S. Ali and A. Madabhushi, "An integrated region-, boundary-, shape-based active contour for multiple object overlap resolution in histological imagery," *IEEE Trans. Med. Imag.*, vol. 31, no. 7, pp. 1448–1460, Jul. 2012.
- [196] L. Yang, P. Meer, and D. J. Foran, "Unsupervised segmentation based on robust estimation and color active contour models," *IEEE Trans. Inf. Technol. Biomed.*, vol. 9, no. 3, pp. 475–486, Sep. 2005.
- [197] O. Schmitt and M. Hasse, "Morphological multiscale decomposition of connected regions with emphasis on cell clusters," *Comput. Vis. Image Understanding*, vol. 113, no. 2, pp. 188–201, Feb. 2009.
- [198] Q. Wang, J. Niemi, C. M. Tan, L. You, and M. West, "Image segmentation and dynamic lineage analysis in single-cell fluorescence microscopy," *Cytometry, A*, vol. 77A, no. 1, pp. 101–110, Jan. 2010.
- [199] L. B. Dorini, R. Minetto, and N. J. Leite, "Semiautomatic white blood cell segmentation based on multiscale analysis," *IEEE J. Biomed. Health Inform.*, vol. 17, no. 1, pp. 250–256, Jan. 2013.
- [200] P. T. Jackway and M. Deriche, "Scale-space properties of the multiscale morphological dilation-erosion," *IEEE Trans. Pattern Anal. Mach. Intell.*, vol. 18, no. 1, pp. 38–51, Jan. 1996.
- [201] E. Meijering, "Cell segmentation: 50 years down the road," *IEEE Signal Process. Mag.*, vol. 29, no. 5, pp. 140–145, Sep. 2012.
- [202] J. B. Roerdink and A. Meijster, "The watershed transform: Definitions, algorithms and parallelization strategies," *Fundamenta Informaticae*, vol. 41, no. 1, pp. 187–228, Apr. 2000.
- [203] S. W. Zucker, "Region growing: Childhood and adolescence," *Comput. Graph. Image Process.*, vol. 5, no. 3, pp. 382–399, 1976.
- [204] N. Béliz-Osorio, J. Crespo, M. García-Rojo, A. Muñoz, and J. Azpiazu, "Cytology imaging segmentation using the locally constrained watershed transform," in *Proc. Math. Morphol. Appl. Image Signal Process.*, 2011, vol. 6671, pp. 429–438.
- [205] F. Cloppet and A. Boucher, "Segmentation of overlapping/aggregating nuclei cells in biological images," in *Proc. IEEE Int. Conf. Pattern Recog.*, Dec. 2008, pp. 1–4.
- [206] L. Yang, Z. Qiu, A. H. Greenaway, and W. Lu, "A new framework for particle detection in low-SNR fluorescence live-cell images and its application for improved particle tracking," *IEEE Trans. Biomed. Eng.*, vol. 59, no. 7, pp. 2040–2050, Jul. 2012.
- [207] L. Qu, F. Long, X. Liu, S. Kim, E. Myers, and H. Peng, "Simultaneous recognition and segmentation of cells-application in *C. elegans*," *Bioinformatics*, vol. 27, no. 20, pp. 2895–2902, Oct. 2011.
- [208] F. Liu, F. Xing, Z. Zhang, M. McGough, and L. Yang, "Robust muscle cell quantification using structured edge detection and hierarchical segmentation," in *Proc. Int. Conf. Med. Image Comput. Comput.-Assisted Intervention*, 2015, vol. 9351, pp. 324–331.
- [209] F. Liu, F. Xing, and L. Yang, "Robust muscle cell segmentation using region selection with dynamic programming," in *Proc. IEEE Int. Symp. Biomed. Imag.*, Apr. 2014, pp. 521–524.
- [210] P. Arbelaez, M. Maire, C. Fowlkes, and J. Malik, "Contour detection and hierarchical image segmentation," *IEEE Trans. Pattern Anal. Mach. Intell.*, vol. 33, no. 5, pp. 898–916, May 2011.
- [211] M. Aharon, M. Elad, and A. Bruckstein, "K-SVD: An algorithm for designing overcomplete dictionaries for sparse representation," *IEEE Trans. Signal Process.*, vol. 54, no. 11, pp. 4311–4322, Nov. 2006.
- [212] A. Santamaria-Pang, Y. Huang, and J. Rittscher, "Cell segmentation and classification via unsupervised shape ranking," in *Proc. IEEE Int. Symp. Biomed. Imag.*, Apr. 2013, pp. 406–409.
- [213] A. Kale and S. Aksoy, "Segmentation of cervical cell images," in *Proc. IEEE Int. Conf. Pattern Recog.*, Aug. 2010, pp. 2399–2402.
- [214] H. G. Akcay and S. Aksoy, "Automatic detection of geospatial objects using multiple hierarchical segmentations," *IEEE Trans. Geosci. Remote Sens.*, vol. 46, no. 7, pp. 2097–2111, Jul. 2008.
- [215] R. Delgado-Gonzalo, V. Uhlmann, D. Schmitter, and M. Unser, "Snakes on a plane: A perfect snap for bioimage analysis," *IEEE Signal Process. Mag.*, vol. 32, no. 1, pp. 41–48, Jan. 2015.
- [216] M. Kass, A. Witkin, and D. Terzopoulos, "Snakes: Active contour models," *Int. J. Comput. Vis.*, vol. 1, pp. 321–331, Jan. 1988.
- [217] N. Xu, N. Ahuja, and R. Bansal, "Object segmentation using graph cuts based active contours," *Comput. Vis. Image Understanding*, vol. 107, no. 3, pp. 210–224, 2007.
- [218] S. Osher and J. A. Sethian, "Fronts propagating with curvature-dependent speed: Algorithms based on Hamilton-Jacobi formulations," *J. Comput. Phys.*, vol. 79, no. 1, pp. 12–49, Nov. 1988.
- [219] V. Caselles, F. Catte, T. Coll, and F. Dibos, "A geometric model for active contours in image processing," *Numerische Mathematik*, vol. 66, no. 1, pp. 1–31, 1993.
- [220] R. Malladi, J. A. Sethian, and B. C. Vemuri, "Shape modeling with front propagation: A level set approach," *IEEE Trans. Pattern Anal. Mach. Intell.*, vol. 17, no. 2, pp. 158–175, Feb. 1995.
- [221] A. Yezzi, S. Kichenassamy, A. Kumar, P. Olver, and A. Tannenbaum, "A geometric snake model for segmentation of medical imagery," *IEEE Trans. Med. Imag.*, vol. 16, no. 2, pp. 199–209, Apr. 1997.
- [222] V. Caselles, R. Kimmel, and G. Sapiro, "Geodesic active contours," *Int. J. Comput. Vis.*, vol. 22, no. 1, pp. 61–79, Feb. 1997.
- [223] T. F. Chan and L. A. Vese, "Active contours without edges," *IEEE Trans. Image Process.*, vol. 10, no. 2, pp. 266–277, Feb. 2001.
- [224] L. A. Vese and T. F. Chan, "A multiphase level set framework for image segmentation using the Mumford and Shah model," *Int. J. Comput. Vis.*, vol. 50, no. 3, pp. 271–293, Dec. 2002.
- [225] D. Mumford and J. Shah, "Optimal approximations by piecewise smooth functions and associated variational problems," *Commun. Pure Appl. Math.*, vol. 42, no. 5, pp. 577–685, Jul. 1989.
- [226] A. Dufour, V. Shinin, S. Tajbakhsh, N. Guillen-Aghion, J. C. Olivo-Marin, and C. Zimmer, "Segmenting and tracking fluorescent cells in dynamic 3D microscopy with coupled active surfaces," *IEEE Trans. Image Process.*, vol. 14, no. 9, pp. 1396–1410, Sep. 2005.
- [227] A. Dufour, R. Thibaux, E. Labryere, N. Guillen, and J. C. Olivo-Marin, "3-D active meshes: Fast discrete deformable models for cell tracking in 3-D time-lapse microscopy," *IEEE Trans. Image Process.*, vol. 20, no. 7, pp. 1925–1937, Jul. 2011.
- [228] K. Li, E. D. Miller, M. Chen, T. Kanade, L. E. Weiss, and P. G. Campbell, "Cell population tracking and lineage construction with spatiotemporal context," *Med. Image Anal.*, vol. 12, no. 5, pp. 546–566, 2008.
- [229] D. Cremers, M. Rousson, and R. Deriche, "A review of statistical approaches to level set segmentation: Integrating color, texture, motion and shape," *Int. J. Comput. Vis.*, vol. 72, no. 2, pp. 195–215, 2007.
- [230] B. Zhang, C. Zimmer, and J. C. Olivo-Marin, "Tracking fluorescent cells with coupled geometric active contours," in *Proc. IEEE Int. Symp. Biomed. Imag.*, Apr. 2004, vol. 1, pp. 476–479.
- [231] D. Padfield, J. Rittscher, N. Thomas, and B. Roysam, "Spatio-temporal cell cycle phase analysis using level sets and fast marching methods," *Med. Image Anal.*, vol. 13, no. 1, pp. 143–155, Feb. 2009.
- [232] J. C. Bezdek, *Pattern Recognition With Fuzzy Objective Function Algorithms*. Norwell, MA, USA: Kluwer, 1981.
- [233] S. K. Nath, K. Rpalaniappan, and F. Bunyak, "Cell segmentation using coupled level sets and graph-vertex coloring," in *Proc. Int. Conf. Med. Image Comput. Comput.-Assisted Intervention*, 2006, vol. 1, pp. 101–108.
- [234] X. Xie and M. Mirmehdi, "MAC: Magnetostatic active contour model," *IEEE Trans. Pattern Anal. Mach. Intell.*, vol. 30, no. 4, pp. 632–646, Apr. 2008.
- [235] M. Rousson and N. Paragios, "Shape priors for level set representations," in *Proc. Eur. Conf. Comput. Vis.*, 2002, vol. 2351, pp. 78–92.
- [236] T. Chan and W. Zhu, "Level set based shape prior segmentation," in *Proc. IEEE Conf. Comput. Vis. Pattern Recog.*, Jun. 2005, vol. 2, pp. 1164–1170.
- [237] C. Li, C. Xu, C. Gui, and M. D. Fox, "Distance regularized level set evolution and its application to image segmentation," *IEEE Trans. Image Process.*, vol. 19, no. 12, pp. 3243–3254, Dec. 2010.
- [238] X. Wu and S. K. Shah, "Cell segmentation in multispectral images using level sets with priors for accurate shape recovery," in *Proc. IEEE Int. Symp. Biomed. Imag.*, Mar. 2011, pp. 2117–2120.

- [239] S. Farhand, R. B. Montero, X. Vial, D. T. Nguyen, M. Reardon, S. M. Pham, F. M. Andreopoulos, and G. Tsechenakis, "Probabilistic multi-compartmently geometric model: Application to cell segmentation," in *Proc. IEEE Int. Symp. Biomed. Imag.*, May 2012, pp. 174–177.
- [240] S. Li, J. Wakefield, and J. A. Noble, "Automated segmentation and alignment of mitotic nuclei for kymograph visualisation," in *Proc. IEEE Int. Symp. Biomed. Imag.*, Mar. 2011, pp. 622–625.
- [241] K. Mosaliganti, A. Gelas, A. Gouaillard, R. Noche, N. Obholzer, and S. Megason, "Detection of spatially correlated objects in 3D images using appearance models and coupled active contours," in *Proc. Int. Conf. Med. Image Comput. Comput.-Assisted Intervention*, 2009, vol. 5762, pp. 641–648.
- [242] L. D. Cohen, "On active contour models and balloons," *CVGIP: Image Understanding*, vol. 53, no. 2, pp. 211–218, Mar. 1991.
- [243] C. Xu and J. L. Prince, "Snakes, shapes, and gradient vector flow," *IEEE Trans. Image Process.*, vol. 7, no. 3, pp. 359–369, Mar. 1998.
- [244] C. Zimmer and J.-C. Olivo-Marin, "Coupled parametric active contours," *IEEE Trans. Pattern Anal. Mach. Intell.*, vol. 27, no. 11, pp. 1838–1842, Nov. 2005.
- [245] X. Han, C. Xu, and J. L. Prince, "A topology preserving level set method for geometric deformable models," *IEEE Trans. Pattern Anal. Mach. Intell.*, vol. 25, no. 6, pp. 755–768, Jun. 2003.
- [246] C. Zimmer, E. Labruiere, V. Meas-Yedid, N. Guillen, and J. C. Olivo-Marin, "Segmentation and tracking of migrating cells in videomicroscopy with parametric active contours: A tool for cell-based drug testing," *IEEE Trans. Med. Imag.*, vol. 21, pp. 1212–1221, Oct. 2002.
- [247] W. Wang, W. He, D. Metaxas, R. Mathew, and E. White, "Cell segmentation and tracking using texture-adaptive snakes," in *Proc. IEEE Int. Symp. Biomed. Imag.*, 2007, pp. 101–104.
- [248] F. Xing and L. Yang, "Unsupervised shape prior modeling for cell segmentation in neuroendocrine tumor," in *Proc. IEEE Int. Symp. Biomed. Imag.*, Apr. 2015, pp. 1443–1446.
- [249] F. Xing and L. Yang, "Fast cell segmentation using scalable sparse manifold learning and affine transform-approximated active contour," in *Proc. Int. Conf. Med. Image Comput. Comput.-Assisted Intervention*, 2015, vol. 9351, pp. 332–339.
- [250] O. Tuzel, L. Yang, P. Meer, and D. J. Foran, "Classification of hematologic malignancies using textron signatures," *Pattern Anal. Appl.*, vol. 10, no. 4, pp. 277–290, Oct. 2007.
- [251] L. Yang, O. Tuzel, W. Chen, P. Meer, G. Salaru, L. A. Goodell, and D. J. Foran, "Pathminer: A web-based tool for computer-assisted diagnostics in pathology," *IEEE Trans. Inf. Technol. Biomed.*, vol. 13, no. 3, pp. 291–299, May 2009.
- [252] H. Cai, X. Xu, J. Lu, J. W. Lichtman, S. P. Yung, and S. T. C. Wong, "Repulsive force based snake model to segment and track neuronal axons in 3D microscopy image stacks," *NeuroImage*, vol. 32, no. 4, pp. 1608–1620, 2006.
- [253] H. Cai, X. Xu, J. Lu, J. Lichtman, S. P. Yung, and S. T. C. Wong, "Shape-constrained repulsive snake method to segment and track neurons in 3D microscopy images," in *Proc. IEEE Int. Symp. Biomed. Imag.*, 2006, pp. 538–541.
- [254] F. Xing and L. Yang, "Robust selection-based sparse shape model for lung cancer image segmentation," in *Proc. Int. Conf. Med. Image Comput. Comput.-Assisted Intervention*, 2013, vol. 8151, pp. 404–412.
- [255] C. Nastar and N. Ayache, "Frequency-based nonrigid motion analysis: Application to four dimensional medical images," *IEEE Trans. Pattern Anal. Mach. Intell.*, vol. 18, no. 11, pp. 1067–1079, Nov. 1996.
- [256] T. F. Cootes, C. J. Taylor, D. H. Cooper, and J. Graham, "Active shape models-their training and application," *Comput. Vis. Image Understanding*, vol. 61, no. 1, pp. 38–59, 1995.
- [257] T. Hastie, R. Tibshirani, and J. Friedman, *The Elements of Statistical Learning: Data Mining, Inference, and Prediction*, 2nd ed. New York, NY, USA: Springer, 2011.
- [258] T. Liu, G. Li, J. Nie, A. Tarokh, X. Zhou, L. Guo, J. Malicki, W. Xia, and S. T. C. Wong, "An automated method for cell detection in zebrafish," *Neuroinformatics*, vol. 6, no. 1, pp. 5–21, Mar. 2008.
- [259] J. MacQueen, "Some methods for classification and analysis of multivariate observations," in *Proc. 5th Berkeley Symp. Math. Statist. Probability*, 1967, vol. 1, pp. 281–297.
- [260] S. Kothari, Q. Chaudry, and M. D. Wang, "Automated cell counting and cluster segmentation using concavity detection and ellipse fitting techniques," in *Proc. IEEE Int. Symp. Biomed. Imag.*, 2009, pp. 795–798.
- [261] X. Bai, C. Sun, and F. Zhou, "Splitting touching cells based on concave points and ellipse fitting," *Pattern Recog.*, vol. 42, no. 11, pp. 2434–2446, 2009.
- [262] S. Kothari, J. H. Phan, R. A. Moffitt, T. H. Stokes, S. E. Hassberger, Q. Chaudry, A. N. Young, and M. D. Wang, "Automatic batch-invariant color segmentation of histological cancer images," in *Proc. IEEE Int. Symp. Biomed. Imag.*, Mar. 2011, pp. 657–660.
- [263] M. Arif and N. Rajpoot, "Classification of potential nuclei in prostate histology images using shape manifold learning," in *Proc. Int. Conf. Mach. Vis.*, Dec. 2007, pp. 113–118.
- [264] R. Nock and F. Nielsen, "On weighting clustering," *IEEE Trans. Pattern Anal. Mach. Intell.*, vol. 28, no. 8, pp. 1223–1235, Aug. 2006.
- [265] G. Bueno, R. González, O. Déniz, M. García-Rojo, J. González-García, M. M. Fernández-Carrobles, N. Vázquez, and J. Salido, "A parallel solution for high resolution histological image analysis," *Comput. Methods Programs Biomed.*, vol. 108, no. 1, pp. 388–401, 2012.
- [266] C. Jung, C. Kim, S. W. Chae, and S. Oh, "Unsupervised segmentation of overlapped nuclei using Bayesian classification," *IEEE Trans. Biomed. Eng.*, vol. 57, no. 12, pp. 2825–2832, Dec. 2010.
- [267] E. Bernardis and S. X. Yu, "Pop out many small structures from a very large microscopic image," *Med. Image Anal.*, vol. 15, no. 5, pp. 690–707, Oct. 2011.
- [268] J. Ge, Z. Gong, J. Chen, J. Liu, J. Nguyen, Z. Yang, C. Wang, and Y. Sun, "A system for counting fetal and maternal red blood cells," *IEEE Trans. Biomed. Eng.*, vol. 61, no. 12, pp. 2823–2829, Dec. 2014.
- [269] X. Wu, M. Amrikachi, and S. K. Shah, "Embedding topic discovery in conditional random fields model for segmenting nuclei using multispectral data," *IEEE Trans. Biomed. Eng.*, vol. 59, no. 6, pp. 1539–1549, Jun. 2012.
- [270] S. Arslan, T. Ersahin, R. Cetin-Atalay, and C. Gunduz-Demir, "Attributed relational graphs for cell nucleus segmentation in fluorescence microscopy images," *IEEE Trans. Med. Imag.*, vol. 32, no. 6, pp. 1121–1131, Jun. 2013.
- [271] H. Kong, M. Gurcan, and K. Belkacem-Boussaid, "Partitioning histopathological images: An integrated framework for supervised color-texture segmentation and cell splitting," *IEEE Trans. Med. Imag.*, vol. 30, no. 9, pp. 1661–1677, Sep. 2011.
- [272] T. Janssens, L. Antanas, S. Derde, I. Vanhorebeek, G. V. den Berghe, and F. G. Grandas, "Charisma: An integrated approach to automatic H&E-stained skeletal muscle cell segmentation using supervised learning and novel robust clump splitting," *Med. Image Anal.*, vol. 17, no. 8, pp. 1206–1219, Dec. 2013.
- [273] A. P. Dempster, N. M. Laird, and D. B. Rubin, "Maximum likelihood from incomplete data via the EM algorithm," *J. Roy. Stat. Soc., B*, vol. 39, no. 1, pp. 1–38, 1977.
- [274] M. Bouguessa, S. Wang, and H. Sun, "An objective approach to cluster validation," *Pattern Recog. Lett.*, vol. 27, no. 13, pp. 1419–1430, Oct. 2006.
- [275] Z. Wu and R. Leahy, "An optimal graph theoretic approach to data clustering: Theory and its application to image segmentation," *IEEE Trans. Pattern Anal. Mach. Intell.*, vol. 15, no. 11, pp. 1101–1113, Nov. 1993.
- [276] P. F. Felzenszwalb and D. P. Huttenlocher, "Efficient graph-based image segmentation," *Int. J. Comput. Vis.*, vol. 59, no. 2, pp. 167–181, Sep. 2004.
- [277] Y. Boykov, O. Veksler, and R. Zabih, "Fast approximate energy minimization via graph cuts," *IEEE Trans. Pattern Anal. Mach. Intell.*, vol. 23, no. 11, pp. 1222–1239, Nov. 2001.
- [278] V. N. Kovacheva, A. M. Khan, M. Khan, D. B. A. Epstein, and N. M. Rajpoot, "DiSWOP: A novel measure for cell-level protein network analysis in localized proteomics image data," *Bioinformatics*, vol. 30, no. 3, pp. 420–427, 2014.
- [279] X. Lou, U. Koethe, J. Wittbrodt, and F. Hamprecht, "Learning to segment dense cell nuclei with shape prior," in *Proc. IEEE Conf. Comput. Vis. Pattern Recog.*, 2012, pp. 1012–1018.
- [280] V. Kolmogorov and Y. Boykov, "What metrics can be approximated by geo-cuts, or global optimization of length/area and flux," in *Proc. IEEE Int. Conf. Comput. Vis.*, Oct. 2005, vol. 1, pp. 564–571.
- [281] Y. Boykov and V. Kolmogorov, "Computing geodesics and minimal surfaces via graph cuts," in *Proc. IEEE Int. Conf. Comput. Vis.*, Oct. 2003, vol. 1, pp. 26–33.
- [282] J. Shi and J. Malik, "Normalized cuts and image segmentation," *IEEE Trans. Pattern Anal. Mach. Intell.*, vol. 22, no. 8, pp. 888–905, Aug. 2000.

- [283] E. Bernardis and S. X. Yu, "Finding dots: Segmentation as popping out regions from boundaries," in *Proc. IEEE Conf. Comput. Vis. Pattern Recog.*, 2010, pp. 199–206.
- [284] S. X. Yu and J. Shi, "Understanding popout through repulsion," in *Proc. IEEE Conf. Comput. Vis. Pattern Recog.*, 2001, vol. 2, pp. II-752–II-757.
- [285] J. D. Lafferty, A. McCallum, and F. C. N. Pereira, "Conditional random fields: Probabilistic models for segmenting and labeling sequence data," in *Proc. Int. Conf. Mach. Learn.*, 2001, pp. 282–289.
- [286] S. Kumar and M. Hebert, "Discriminative random fields," *Int. J. Comput. Vis.*, vol. 68, no. 2, pp. 179–201, Jun. 2006.
- [287] J. Pan, T. Kanade, and M. Chen, "Heterogeneous conditional random field: Realizing joint detection and segmentation of cell regions in microscopic images," in *Proc. IEEE Conf. Comput. Vis. Pattern Recog.*, Jun. 2010, pp. 2940–2947.
- [288] M. Uzunbas, C. Chen, and D. Metaxas, "Optree: A learning-based adaptive watershed algorithm for neuron segmentation," in *Proc. Int. Conf. Med. Image Comput. Comput.-Assisted Intervention*, 2014, vol. 8673, pp. 97–105.
- [289] L. Grady, "Random walks for image segmentation," *IEEE Trans. Pattern Anal. Mach. Intell.*, vol. 28, no. 11, pp. 1768–1783, Nov. 2006.
- [290] Y. Chen, P. Huang, K. Lin, H. Lin, L. Wang, C. Cheng, T. Chen, Y. Chan, and J. Y. Chiang, "Semi-automatic segmentation and classification of pap smear cells," *IEEE J. Biomed. Health Inform.*, vol. 18, no. 1, pp. 94–108, Jan. 2014.
- [291] S. Andrews, G. Hamarneh, and A. Saad, "Fast random walker with priors using precomputation for interactive medical image segmentation," in *Proc. Int. Conf. Med. Image Comput. Comput.-Assisted Intervention*, 2010, vol. 6363, pp. 9–16.
- [292] P. Wattuya, K. Rothaus, J. S. Prassni, and X. Jiang, "A random walker based approach to combining multiple segmentations," in *Proc. IEEE Int. Conf. Pattern Recog.*, Dec. 2008, pp. 1–4.
- [293] L. Yang, O. Tuzel, P. Meer, and D. J. Foran, "Automatic image analysis of histopathology specimens using concave vertex graph," in *Proc. Int. Conf. Med. Image Comput. Comput.-Assisted Intervention*, 2008, vol. 5241, pp. 833–841.
- [294] Z. Wu, D. Gurari, J. Y. Wong, and M. Betke, "Hierarchical partial matching and segmentation of interacting cells," in *Proc. Int. Conf. Med. Image Comput. Comput.-Assisted Intervention*, 2012, vol. 7510, pp. 389–396.
- [295] T. R. Jones, A. E. Carpenter, and P. Golland, "Voronoi-based segmentation of cells on image manifolds," in *Proc. Comput. Vis. Biomed. Image Appl.*, 2005, vol. 3765, pp. 535–543.
- [296] T. R. Jones, A. E. Carpenter, P. Golland, and D. M. Sabatini, *Methods for High-Content, High Throughput Image-Based Cell Screening*. J. Rittscher, R. Machiraju, and S. T. C. Wong, Eds. Norwood, MA, USA: Artech House, 2008.
- [297] E. W. Dijkstra, "A note on two problems in connection with graphs," *Numerische Math.*, vol. 1, no. 1, pp. 269–271, 1959.
- [298] H. Shen, G. Nelson, D. E. Nelson, S. Kennedy, D. G. Spiller, T. Griffiths, N. Paton, S. G. Oliver, M. R. H. White, and D. B. Kell, "Automated tracking of gene expression in individual cells and cell compartments," *J. Roy. Soc. Interface.*, vol. 3, no. 11, pp. 787–794, Dec. 2006.
- [299] C. Zhang, J. Yarkony, and F. A. Hamprecht, "Cell detection and segmentation using correlation clustering," in *Proc. Int. Conf. Med. Image Comput. Comput.-Assisted Intervention*, 2014, vol. 8673, pp. 9–16.
- [300] J. Yarkony, A. Ihler, and C. C. Fowlkes, "Fast planar correlation clustering for image segmentation," in *Proc. Eur. Conf. Comput. Vis.*, 2012, vol. 7577, pp. 568–581.
- [301] F. Zhou, J. Feng, and Q. Shi, "Texture feature based on local Fourier transform," in *Proc. IEEE Int. Conf. Image Process.*, Oct. 2001, vol. 2, pp. 610–613.
- [302] R. Duda, P. Hart, and D. Stork, *Pattern Classification*, 2nd ed. New York, NY, USA: Wiley, 2001.
- [303] Z. Yin, R. Bise, M. Chen, and T. Kanade, "Cell segmentation in microscopy imagery using a bag of local Bayesian classifiers," in *Proc. IEEE Int. Symp. Biomed. Imag.*, Apr. 2010, pp. 125–128.
- [304] Y. Zhou, H. Chang, K. E. Barner, and B. Parvin, "Nuclei segmentation via sparsity constrained convolutional regression," in *Proc. IEEE Int. Symp. Biomed. Imag.*, Apr. 2015, pp. 1284–1287.
- [305] D. Ciresan, A. Giusti, L. M. Gambardella, and J. Schmidhuber, "Deep neural networks segment neuronal membranes in electron microscopy images," in *Proc. Adv. Neural Inf. Process. Syst.*, 2012, pp. 2843–2851.
- [306] S. Kumar, S. Ong, S. Ranganath, T. C. Ong, and F. T. Chew, "A rule-based approach for robust clump splitting," *Pattern Recog.*, vol. 39, no. 6, pp. 1088–1098, Jun. 2006.
- [307] W. Beaver, D. Kosman, G. Tedeschi, E. Bier, W. McGinnis, and Y. Freund, "Segmentation of nuclei on confocal image stacks using performance based thresholding," in *Proc. IEEE Int. Symp. Biomed. Imag.*, Apr. 2007, pp. 53–56.
- [308] Y. Freund and L. Mason, "The alternating decision tree learning algorithm," in *Proc. Int. Conf. Mach. Learn.*, 1999, pp. 124–133.
- [309] L. Cheng, N. Ye, W. Yu, and A. Cheah, "Discriminative segmentation of microscopic cellular images," in *Proc. Int. Conf. Med. Image Comput. Comput.-Assisted Intervention*, 2011, vol. 6891, pp. 637–644.
- [310] A. Levinshtein, A. Stere, K. N. Kutulakos, D. J. Fleet, S. J. Dickinson, and K. Siddiqi, "Turbopixels: Fast superpixels using geometric flows," *IEEE Trans. Pattern Anal. Mach. Intell.*, vol. 31, no. 12, pp. 2290–2297, Dec. 2009.
- [311] W. Yu, H. K. Lee, S. Hariharan, W. Bu, and S. Ahmed, "Evolving generalized Voronoi diagrams for accurate cellular image segmentation," *Cytometry, A*, vol. 77A, no. 4, pp. 379–386, Apr. 2010.
- [312] L. Roux, D. Racoceanu, N. Lomenie, M. Kulikova, H. Irshad, J. Klossa, F. Capron, C. Genestie, G. L. Naour, and M. N. Gurcan, "Mitosis detection in breast cancer histological images an ICPR 2012 contest," *J. Pathol. Inform.*, vol. 4, no. 1, pp. 1–8, May 2013.
- [313] MITOS. (2012). *MITOS dataset*. [Online]. Available: [http://ludo17.free.fr/mitos\\_2012/](http://ludo17.free.fr/mitos_2012/)
- [314] M. Veta *et al.*, "Assessment of algorithms for mitosis detection in breast cancer histopathology images," *Med. Image Anal.*, vol. 20, no. 1, pp. 237–248, 2015.
- [315] AMIDA. (2013). *MICCAI 2013 Grand Challenge*. [Online]. Available: <http://amida13.isi.uu.nl/>
- [316] E. D. Gelasca, B. Obara, D. Fedorov, K. Kvilekval, and B. Manjunath, "A biosegmentation benchmark for evaluation of bioimage analysis methods," *BMC Bioinform.*, vol. 10, no. 368, pp. 1–12, Nov. 2009.
- [317] L. P. Coelho, A. Shariff, and R. F. Murphy, "Nuclear segmentation in microscope cell images: A hand-segmented dataset and comparison of algorithms," in *Proc. IEEE Int. Symp. Biomed. Imag.*, Jun. 2009, pp. 518–521.
- [318] M. Maska *et al.*, "A benchmark for comparison of cell tracking algorithms," *Bioinformatics*, vol. 30, no. 11, pp. 1609–1617, Feb. 2014.
- [319] NIH. (2016). *Image J*. [Online]. Available: <http://imagej.nih.gov/ij/>
- [320] C. A. Schneider, W. S. Rasband, and K. W. Eliceiri, "NIH image to imagej: 25 years of image analysis," *Nature Methods*, vol. 9, no. 7, pp. 671–675, Jul. 2012.
- [321] A. E. Carpenter, T. R. Jones, M. R. Lamprecht, C. Clarke, I. H. Kang, O. Friman, D. A. Guertin, J. H. Chang, R. A. Lindquist, J. Moffat, P. Golland, and D. M. Sabatini, "CellProfiler: Image analysis software for identifying and quantifying cell phenotypes," *Genome Biol.*, vol. 7, no. 10, p. R100, Oct. 2006.
- [322] T. R. Jones, A. E. Carpenter, M. R. Lamprecht, J. Moffat, S. J. Silver, J. K. Grenier, A. B. Castoreno, U. S. Eggert, D. E. Root, P. Golland, and D. M. Sabatini, "Scoring diverse cellular morphologies in image-based screens with iterative feedback and machine learning," in *Proc. Natl. Acad. Sci. USA*, vol. 106, no. 6, pp. 1826–1831, Feb. 2009.
- [323] J. Moffat *et al.*, "A lentiviral RNAi library for human and mouse genes applied to an arrayed viral high-content screen," *Cell*, vol. 124, no. 6, pp. 1283–1298, 2006.
- [324] K. W. Eliceiri, M. R. Berthold, I. G. Goldberg, L. Ibanez, B. S. Manjunath, M. E. Martone, R. F. Murphy, H. Peng, A. L. Plant, B. Roysam, N. Stuurman, J. R. Swedlow, P. Tomancak, and A. E. Carpenter, "Biological imaging software tools," *Nature Methods*, vol. 9, no. 7, pp. 697–710, Jul. 2012.
- [325] E. Meijering, O. Dzyubachyk, and I. Smal, "Methods for cell and particle tracking," in *Imaging and Spectroscopic Analysis of Living Cells—Optical and Spectroscopic Techniques*, vol. 504. Cambridge, MA, USA: Academic Press, 2012, pp. 183–200.
- [326] A. E. Carpenter, L. Kametsky, and K. W. Eliceiri, "A call for bioimaging software usability," *Nature Methods*, vol. 9, no. 7, pp. 666–670, Jul. 2012.

Authors' photographs and biographies not available at the time of publication.